# Chiral Structured Illumination Microscopy

A Microscopy Modality for Imaging
Fluorescent Chiral Domains at Sub-wavelength Resolution

## Dissertation

von M.Sc. Shiang-Yu Huang
geboren am 06.10.1990 in Taoyuan City, Taiwan

Supervisors: Prof. Dr. Rainer Heintzmann and Dr. habil. Jer-Shing Huang

Gutachter:


Prof. Dr. Rainer Heintzmann

*Institute of Physical Chemistry, Friedrich-Schiller-University Jena, Jena, Germany*

*Leibniz Institute of Photonic Technology, Jena, Germany*


Prof. Dr. Christian Eggeling

*Institute for Applied Optics and Biophysics, Friedrich Schiller University Jena, Jena, Germany*

*Leibniz-Institute of Photonic Technology, Jena, Germany*


Prof. Dr. Wei-Shun Chang

*Department of Chemistry and Biochemistry, University of Massachusetts Dartmouth, North Dartmouth, United States*

Tag der Disputation: 22.06.2022

*"Cleverness is a gift, kindness is a choice."*

– Jeff Bezos

# Abstract

Many microscopy methods have been developed to visualize the molecular chirality distribution. However, their performance is usually limited due to the low imaging speed, diffraction-limited resolution, or weak chiroptical responses. In this sense, a wide-field super-resolution chiral imaging modality that has the flexibility of applying various illumination schemes to enhance chiral light-matter interaction is highly desired.

This thesis covers the development of chiral structured illumination microscopy (chiral SIM), a novel wide-field super-resolution microscopy that is able to address the shortcomings restricting the capability of conventional chiral imaging techniques. Accordingly, the research background and fundamentals in regards to this new microscopy method are introduced at the beginning. The subsequent chapters illustrate the development of chiral SIM in both theoretical and experimental aspects. In particular, we establish the theoretical framework of chiral SIM and investigate possible far-field illumination schemes for its experimental realization. The proof-of-principle numerical simulations demonstrate its ability to image and discriminate chiral domains at super-resolution. The signal-to-noise ratio of the chiral SIM images simulated under different experimental conditions is analyzed to inspect the performance of chiral SIM. Meanwhile, we study the near-field illumination schemes that exploit the superchiral near fields generated by plasmonic or dielectric nanostructures to reinforce the chiroptical responses and elaborate on the main difficulty of applying them in the proposed chiral SIM method. After a series of theoretical work, we present our experimental attempts at the chiral SIM method. The fabrication and inspection of the selected chiral sample and the optical setups are specifically discussed. Although the experimental results are unsatisfactory, based on the following investigation, we further propose a new optical setup to solve the potential issues of the original chiral SIM setup. Finally, we summarize this thesis and provide suggestions that should be beneficial to the subsequent research in chiral SIM and may also open up new research fields.

At present, the chiral SIM method is still in its infancy. We hope the work presented in this thesis could not only inspire new ideas but also provide valuable insights that help to advance this new chiral imaging modality towards real applications in diverse fields in the future.

# Zusammenfassung

Viele Mikroskopieverfahren wurden entwickelt, um die molekulare Chiralitätsverteilung sichtbar zu machen. Ihre Leistungsfähigkeit ist jedoch in der Regel aufgrund der geringen Bildgebungsgeschwindigkeit, der beugungsbegrenzten Auflösung oder der schwachen chiroptischen Reaktionen begrenzt. In diesem Sinne wäre eine chirale Weitfeld-Superauflösungs-Bildgebungsmodalität, die die Flexibilität hat, verschiedene Beleuchtungsschemata anzuwenden, um die chirale Licht-Materie-Wechselwirkung zu verbessern, sehr wünschenswert.

Diese Arbeit befasst sich mit der Entwicklung der chiralen strukturierten Beleuchtungsmikroskopie (chiral SIM), einer neuartigen superauflösenden Weitfeldmikroskopie, die in der Lage ist, die Unzulänglichkeiten herkömmlicher chiraler Bildgebungsverfahren zu beheben. Dementsprechend werden zu Beginn der Arbeit der Forschungshintergrund und die Grundlagen dieser neuen Mikroskopiemethode vorgestellt. In den folgenden Kapiteln wird die Entwicklung der chiralen SIM sowohl in theoretischer als auch in experimenteller Hinsicht dargestellt. Insbesondere werden die theoretischen Rahmenbedingungen der chiralen SIM herausgearbeitet und mögliche Fernfeldbeleuchtungsschemata für ihre experimentelle Umsetzung untersucht. Die numerischen Simulationen zum Nachweis des Prinzips zeigen die prinzipielle Möglichkeit, chirale Domänen mit hoher Auflösung abzubilden und zu unterscheiden. Das Signal-Rausch-Verhältnis der chiralen SIM-Bilder, die unter verschiedenen experimentellen Bedingungen simuliert wurden, wird analysiert, um die Leistungsfähigkeit der chiralen SIM zu überprüfen. Weiterhin untersuchen wir die Nahfeldbeleuchtungsschemata, die die durch plasmonische oder dielektrische Nanostrukturen erzeugten superchiralen Nahfelder ausnutzen, um die chiroptischen Antworten zu verstärken, und arbeiten die Hauptschwierigkeit ihrer Anwendung in der vorgeschlagenen chiralen SIM-Methode heraus. Nach diesen theoretischen Betrachtungen stellen wir unsere experimentellen Versuche mit der chiralen SIM-Methode vor. Die Herstellung und Inspektion der ausgewählten chiralen Probe und die optischen Aufbauten werden speziell besprochen. Obwohl die experimentellen Ergebnisse nicht zufriedenstellend sind, schlagen wir auf der Grundlage der erfolgten Untersuchungen einen neuen optischen Aufbau vor, um die potenziellen Probleme des ursprünglichen chiralen SIM-Aufbaus zu lösen. Abschließend fassen wir diese Arbeit zusammen und geben Anregungen, die für

die weitere Forschung auf dem Gebiet der chiralen SIM von Nutzen sein sollten und auch neue Forschungsfelder eröffnen können.

Zurzeit steckt die chirale SIM-Methode noch in den Kinderschuhen. Wir hoffen, dass die in dieser Arbeit vorgestellten Ergebnisse nicht nur neue Ideen inspirieren, sondern auch wertvolle Erkenntnisse liefern, die dazu beitragen, dass diese neue chirale Bildgebungsmethode in Zukunft in verschiedenen Bereichen tatsächlich angewendet werden kann.

# Acknowledgements

I still remember the first day I came to Jena. It was freezing cold and I was astonished by the views of snow that flooded the sidewalks or capped the surrounding mountains as I arrived in January. Jer-Shing was already waiting for me at the parking lot in Paradise Station. Pursuing a Ph.D. in a foreign country is adventurous. But overcoming the difficulties encountered while heading towards the research goals is never an easy task. Every single tiny thing could turn out to be very complicated to deal with due to different ideologies and cultural differences. A better way is to meet the balance between work and relationships and, at the same time, remember to cheer yourself on and keep concentrating on the things you love and believe in. Studying for Ph.D. has been a really long journey and I would not have accomplished this without the help and support from my supervisors, colleagues, friends and family.

I am indebted to many friends I have met in IPHT. I would like to thank Christian and Ronny for dealing with many technical problems with me in the lab when I was a novice at the microscopy experiments. I also would like to thank Monalisa for the valuable discussions and the time she has spent with me in troubleshooting my tricky optical setups. Thank you to Benedict for asking me if I might have difficulties in continuing my Ph.D. program. Your consideration is very heartwarming. Many thanks to Joon for being considerate of me when I was struggling with writing a proposal based on my Ph.D. project. Further, I greatly thank Tino and Amir from the Ph.D. council for listening to me when I felt very depressed about my research results and giving me a piece of advice. Special thanks to Adriana, our secretary, who is always willing to help me deal with many things, regardless of administrative paperwork or problems I encountered during my life in Jena.

I would like to express my gratitude to all of the friends in our research group FA Nanooptics. Thank you to Lei for doing research and sharing working experience with me. I would also like to greatly thank Jiwei for everything he has taught me. He always selflessly shares his knowledge and experience with me. I really had a great time working on the project with him. Also, I want to thank the triple-A team, Ankit, Abhik, Ahbro, and Luan-Ying for the wonderful time we had in the office, restaurants and mountains, which gave me a lot of joy and energy. And I definitely have to thank Yi-Ju for her kind

# Table of Contents

# Acronyms

**CD** Circular Dichroism

**CPL** Circularly Polarized Light

**EPL** Elliptically Polarized Light

**FDCD** Fluorescence-Detected Circular Dichroism

**FDLD** Fluorescence-Detected Linear Dichroism

**FDTD** Finite-Difference Time-Domain

**HWP** Half-Wave Plate

**LCPL** Left-Circularly Polarized Light

**LCVR** Liquid Crystal Variable Retarder

**LD** Linear Dichroism

**LEPL** Left-Elliptically Polarized Light

**LPSIM** Localized Plasmonic Structured Illumination Microscopy

**LPL** Linearly Polarized Light

**NA** Numerical Aperture

**OC** Optical Chirality

**1DPC** One-Dimensional Photonic Crystal

**OR** Optical Rotation

**ORD** Optical Rotatory Dispersion

**OTF** Optical Transfer Function

**PALM** Photoactivated Localization Microscopy

**PEM** Photoelastic Modulator

**PSF** Point Spread Function

**RCPL** Right-Circularly Polarized Light

**REPL** Right-Elliptically Polarized Light

**SHG** Second-Harmonic Generation

**SIM** Structured Illumination Microscopy

**SLM** Spatial Light Modulator

**sCMOS** Scientific CMOS

**SNOM** Scanning Near-field Optical Microscopy

**SNR** Signal-To-Noise Ratio

**STED** Stimulated Emission Depletion Microscopy

**STORM** Stochastic Optical Reconstruction Microscopy

**TM** Transverse Magnetic

**TPF** Two-Photon Fluorescence

**TE** Transverse Electric

# Chapter 1

# Background

## 1.1 Motivation

As a widespread adage, *seeing is believing* conveys the importance of visual witnesses. Especially in the scientific community, visualization of objects is always a strong proof of existence. Optical microscopy is a technique devised to view minute objects and has been successful in many research subjects. For instance, remarkable advances in fluorescence microscopy facilitate a variety of applications, such as subcellular imaging and single-molecule localization, and thus renders fluorescence microscopy a powerful tool in material and biomedical science. Optical microscopy also plays an important role in chiral analysis. Various imaging techniques are developed to reveal the spatial distribution of local chiral domains at various spatial scales. Rich structural information on, for example, supramolecules, nanomaterials, and chiral polymers greatly expands our understanding of the related conformational changes of molecular systems. The signal detected in those chiral imaging techniques is unique. In most cases, the differential absorption upon circular polarization excitation, namely circular dichroism (CD), is detected, which discloses the molecular chirality that cannot be seen by traditional microscopy methods. Still, state-of-the-art chiral imaging modalities have left much to be desired. We summarize three main limitations that restrict the capability of current chiral imaging methods:

- Relatively low imaging speed

Confocal or other scanning-based imaging modalities are widely used in the investigation of local chiral domains. However, due to their scanning nature, the imaging rate is inherently low and thus reduces temporal resolution or relevant throughput.

- Diffraction-limited resolution

The resolution of traditional far-field optical microscopes is circumscribed by the celebrated Abbe limit due to the diffraction of light, which highly restricts the studies of chiral domains in the sub-wavelength regime.

- Low chiral contrast due to weak chiral light-matter interaction

The issue of the intrinsically weak chiral light-matter interaction is the most challenging aspect of chiral imaging. weak chiral response of samples, which originates from the size mismatch between molecules and the pitch of chiral light (e.g. circularly-polarized wave), leads to low signal-to-noise ratio and thus severely degrades the quality of the images.

We aim to develop a new wide-field microscopy method that has the potential to address the aforementioned limitations. Inspired by structured illumination microscopy (SIM), we conceive a novel imaging method, called chiral SIM, by incorporating SIM with optical chirality engineering (i.e. tailoring chiral optical fields) and fluorescence-detected circular dichroism for fast chiral imaging at super-resolution. The chiral SIM method theoretically has higher image speed compared to conventional scanning-based methods because the sample will be excited in a wide-field fashion (i.e. whole sample volume is illuminated in single image acquisition). Via a specialized image reconstruction program, the high spatial frequency information that is down-modulated due to the moiré effect on chiral domains can be restored, which generates super-resolved chiral images. In addition, exploiting the enhanced chiral optical fields formed near the plasmonic or dielectric nanostructures may be a promising solution to the weak chiral light-matter interaction in chiral analysis or imaging. Since the chiral SIM method is generally flexible to adapt to various illumination schemes, nanostructures that can sculpt the enhanced chiral optical fields into the desired excitation patterns are highly expected for further improving the performance of chiral SIM.

In the following, the background knowledge and the development of microscopy methods that relate to the chiral SIM research are summarized. Specifically, we present a brief introduction to chirality analysis and chiroptical effects and showcase the complementary chiral imaging and super-resolution optical microscopy methods.

## 1.2 Chirality and Chiral Analysis

Chirality is a fundamental characteristic that describes the lack of symmetry in three-dimensional conformation. This term can be traced back to the Greek $\chi\epsilon\iota\rho$, which means hand, and was first introduced by the British scientist Lord Kelvin in 1893 to dictate the situation where an object, shape or set of points cannot be superimposed on its mirror image [1]. Our hands are a classic example to illustrate what a chiral object looks like (Fig. 1.1). They also provide a way to name the chirality of an arbitrary object: left-handed or right-handed depending on the sense in which the object twists or curves.

Chirality is a pervasive phenomenon in nature and especially of great importance at the molecular level. Various chemical compounds and biological macromolecules, like sugar, enzymes, and proteins, are chiral. A pair of chiral molecules with mutually opposite handedness is known as enantiomers. Although enantiomers share the same physical properties, such as molecular mass, density, they exhibit diverse functionalities when interacting with living organisms. The chemical reactions or biological processes where chiral molecules are involved may vary greatly according to the molecular chirality and could, in the worst case, cause adverse effects on the organic system. A notorious example is the misuse of Thalidomide. In 1957, this drug was marketed with the trade name Contergan and prescribed as a sedative and antiemetic to alleviate nausea in pregnant women. Thalidomide was provided as racemic mixtures that comprise the same amount of left- and right-handed forms. Unfortunately, the left-handed enantiomers ((S)-thalidomide) leads to serious birth defects and about 10,000 infants worldwide were affected and born with limb malformation or deficiencies [2]. Therefore, enantioselective separation and characterization of molecular chirality play a crucial role in the pharmaceutical industry to prevent undesired side effects.

Commonly, the handedness of chiral molecules is characterized by how they interact with light. When light propagates through a randomly-oriented chiral molecule, optical properties such as intensity and polarization state are influenced depending on molecular chirality. Typical chiroptical (chiral-optical) responses include optical rotatory dispersion (ORD) and CD, referring to the rotation of the polarization plane of linearly polarized light (LPL) and the difference in the absorption upon two circularly polarized light (CPL), respectively. We illustrate those chiroptical effects in detail in Sec. 1.3. Since the size of most molecules (1 Å to 10 nm) and the pitch of the electromagnetic helix in CPL (several hundreds of nanometers in visible regime) are not comparable, molecules hardly

sense the helical pitch of the excitation fields, leading to the formidable weak chiral light-matter interaction. Nevertheless, by measuring the difference in the absorption of left- (LCPL) and right-circularly polarized light (RCPL), CD spectroscopy is a very successful tool for the routine study of the absolute molecular conformation or probing the structure of macromolecules [3, 4].
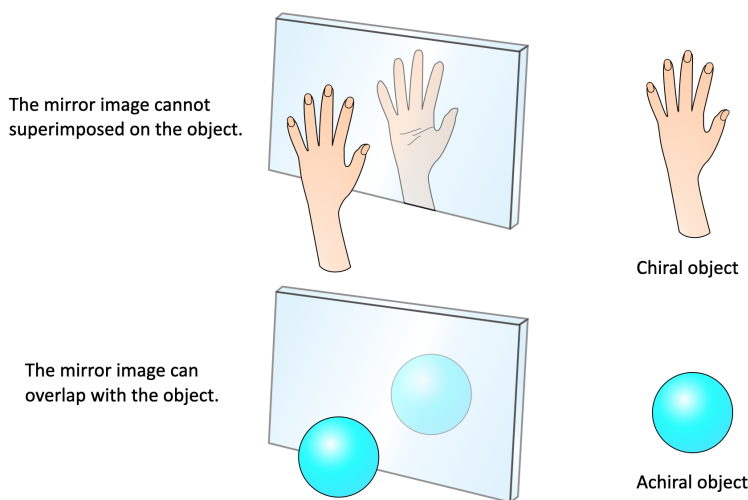


**Figure 1.1:** Definition of a chiral object.

## 1.3 Chiroptical Effects

The interaction between light and matter manifests itself in various phenomena, such as reflection, scattering, dispersion, and absorption. Distinctive responses occur especially when light interacts with chiral materials, which are known as the chiroptical effects [5, 6]. The discovery of chiroptical effects was first reported in 1811 when the French physicist Dominique Arago observed the dispersion of colors after the sunlight passed through a quartz crystal [7]. Soon with subsequent investigations on various compounds in solutions, the French physicist Jean Baptiste Biot ascribed the color dispersion to the rotation of the polarization plane of LPL [8]. This is known as circular birefringence or optical rotation (OR) and the corresponding wavelength dependence is termed ORD. The material that has the ability to rotate the polarization plane of LPL is called optically active. At the same time, scientists also focused on the absorptive properties of optically active materials. The early discoveries associated with the differential absorption upon two types of CPL, known as CD, were reported by an Austrian mineralogist Wilhelm

Haidinger in 1847 in amethyst quartz [9], and by a French physicist Aimé Cotton in 1895 in the solution of metal complexes [10].

Owing to the sensitivity of the chiroptical effects to molecular geometry, spectroscopic methods that detects ORD and CD have been widely used to characterize the absolute configuration of molecules or the related conformational changes. This characterization is crucial in many fields, such as pharmaceutics, material science, stereochemistry, and biophysics, because molecular chirality governs the functionalities of molecules. With the assistance of electronic devices, especially the photoelastic modulator (PEM), the development of chiroptical spectroscopy was greatly boosted in the late twenty century. Between these two spectroscopic techniques, there is a clear preference for CD spectroscopy because it has a smaller spectral bandwidth compared to ORD spectroscopy. Besides, the absorption bands of CD do not overlap extensively, which, on the contrary, usually happens in the case of ORD, and provides better discrimination for various elements [5, 11, 12]. In the following, we discuss the phenomenological equations that describe OR and CD.

### 1.3.1 Optical Rotation
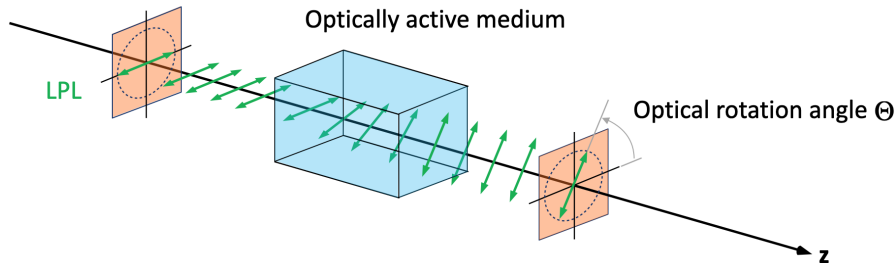


**Figure 1.2:** Illustration of OR. The polarization plane of the LPL rotates after the light passes through the optically active medium.

Linear chiroptical effects, such as OR and CD, are the manifestation of the difference in the refractive and absorption indices for LCPL and RCPL. These two phenomena can be elaborated if we consider LPL a superposition of LCPL and RCPL of equal amplitudes [13]. When LPL travels through an optically active medium, these two circularly polarized components experience different levels of refraction and their velocities are reduced correspondingly, which introduces the optical rotation angle [5]

$$\Theta = \frac{\pi s}{\lambda}(n_L - n_R), \tag{1.1}$$

to the orientation of the polarization plane at a specific wavelength. Here, $\lambda$ is the wavelength of light and $s$ is the propagation length within the optically active medium. $n_L$ and $n_R$ are the refractive indices of LCPL and RCPL, respectively. The polarization plane of the LPL thus rotates by an angle of $\Theta$, as shown in Fig. 1.2, which illustrates the phenomenon of OR.

### 1.3.2 Circular Dichroism
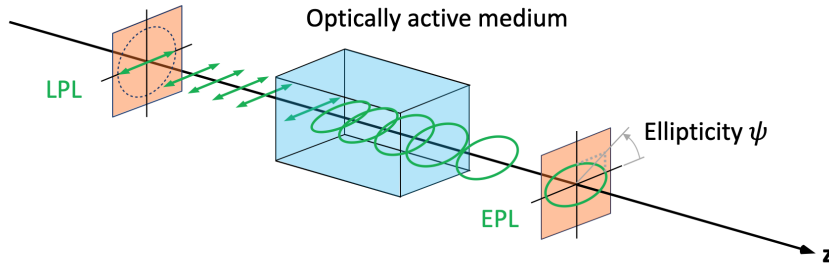


**Figure 1.3:** Illustration of CD. LPL is converted into EPL after passing through the absorbing optically active medium.

In addition to rotating the polarization plane of the LPL, optically active materials also exhibit peculiar absorption behavior. When LPL traverses an absorbing chiral medium, two circularly polarized components of LPL undergo different degrees of attenuation due to the difference in the absorption indices of LCPL and RCPL. Since the superposition of two circularly polarized components of unequal amplitudes leads to elliptical polarization, the LPL is then converted into EPL (Fig. 1.3). The corresponding ellipticity $\psi$, i.e. the ratio of the minor and major axes of the polarization ellipse, is given by [5]

$$\tan \psi = \tanh[\frac{\pi s}{\lambda}(\kappa_L - \kappa_R)], \tag{1.2}$$

where $s$ is the penetration length. $\kappa_L$ and $\kappa_R$ are the absorption indices of LCPL and RCPL, respectively. In general, $\psi$ is small such that

$$\psi \approx \frac{\pi s}{\lambda}(\kappa_L - \kappa_R). \tag{1.3}$$

In this way, the CD phenomenon directly relates to the ellipticity of the emerging EPL.

CD can also be expressed as the difference in absorbance of individual LCPL and RCPL, as shown in the following equation

$$\Delta A = A_L - A_R = (\epsilon_L - \epsilon_R)cl, \tag{1.4}$$

where $A_L$ $(A_R)$ and $\epsilon_L$ $(\epsilon_R)$ are the absorbance and the molar extinction coefficient upon the illumination of LCPL (RCPL), respectively. c is the molar concentration of the material and $l$ denotes the path length. In practice, a dimensionless quantity called Kuhn dissymmetry factor [5, 14]

$$g_{\text{CPL}} = \frac{A_L - A_R}{\frac{1}{2}(A_L + A_R)} = \frac{\epsilon_L - \epsilon_R}{\frac{1}{2}(\epsilon_L + \epsilon_R)}, \tag{1.5}$$

is usually introduced as an experimental criterion to estimate the chiral asymmetry of a given system. Here, the subscript CPL emphasizes that the dissymmetry factor is measured upon circularly polarized excitation. As shown in Eq. 1.5, $g_{\text{CPL}}$ is the ratio of the differential absorption $A_L - A_R$ to the conventional absorption $\frac{1}{2}(A_L + A_R)$ and links to molecular conformation or chirality. The value of $g_{\text{CPL}}$ ranges from $+2$ to $-2$ and the extreme values $+2$ and $-2$ indicate that LCPL and RCPL are completely absorbed, respectively. Nevertheless, because the interaction between light and chiral molecules is usually weak, the magnitude of $g_{\text{CPL}}$ for natural chiral molecules is generally in the order of $10^{-3} \sim 10^{-4}$ [15, 16]. .

Alternatively, CD can be associated with the difference in the intensity of the emitted fluorescence upon the illumination of LCPL and RCPL called fluorescence-detected circular dichroism (FDCD). FDCD is based on the assumption that the excitation spectrum of a fluorophore parallels its absorption spectrum. In other words, the intensity of the fluorescence emission is primarily dependent on the amount of absorbed light [17, 18]. The fluorophores should also be either chiral or attached to a chiral assembly to generate the FDCD signal [19]. The Brownian motion should randomize the orientation of the fluorophores such that the artifacts caused by photoselection are reduced [19, 20]. While FDCD is an indirect way to detect CD, it enables the CD measurement for specific fluorophores in a group of non-fluorescent chiral molecules. Thus, FDCD spectroscopy offers superior selectivity compared to the conventional CD counterpart.

## 1.4 Contemporary Chiral Imaging Techniques

Whereas chiroptical spectroscopic techniques provide rich structural information on numerous molecules, the lack of spatial information hinders the studies that seek to investigate the local chirality distribution. The demand for such investigation undoubtedly leads to the advent of versatile chiral imaging techniques. With these techniques, researchers nowadays can study not only the structural properties of chemicals and biological macromolecules but also the chiroptical properties of plasmonic nanostructures. In the following, we introduce state-of-the-art chiral imaging techniques to offer a better understanding of the current status of the research field.

### 1.4.1 Chiral Imaging via Modification of Existing CD Spectrometers

Intuitively, the sample holder in a typical CD spectrometer can be combined with a scanning stage to map the CD distribution and multiple CD spectra are collected to compose an image of CD distribution with respect to different wavelengths. This type of modification has been realized recently in a commercial CD spectrometer [21] and a synchrotron radiation CD spectrometer [22, 23]. In these works, the CD distribution of supramolecules is imaged to understand the mechanism of the molecular formation and characterize the local aggregation. Still, the spatial resolution of this type of CD mapping is limited to millimeter scale.
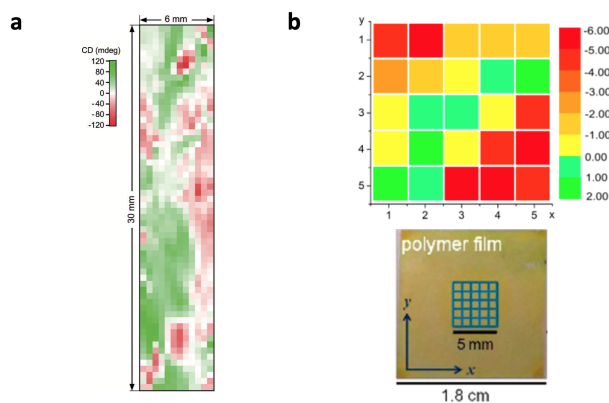


**Figure 1.4:** (a) CD image of a TAP-CyCo6 gel. The image was obtained by scanning the sample cuvette. Reprinted with permission for reference [21]. Copyright 2019, Wiley. (b) Top: CD map of chiral polymers. Bottom: Photo of the irradiated $5 \times 5$ sampling grid. Reprinted with permission for reference [22]. Copyright 2017, American Chemical Society.

### 1.4.2 Polarimetric Microscopy

Polarimetric microscopy is commonly used in chiral analysis since chiral substances are sensitive to the polarization of light. In theory, the polarization of light can be characterized by the Stokes vector or, if the light is completely polarized, the Jones vector.

When light enters an object, its properties change accordingly and the whole process can be mathematically described by the transformation of the Stokes vector or Jones vector. The object is then characterized by a transformation matrix, i.e. the Mueller matrix or Jones Matrix, in which the elements correspond to polarimetric properties of the object. Through Stokes-Mueller calculus or Jones calculus, the transformation matrix of an unknown medium put in a polarimetric microscope can be inferred with the prior knowledge of other optical components in the setup. Thus, one can study various optical properties, such as linear birefringence, linear dichroism, OR, and CD, of the medium.

Measuring the Jones matrix and Mueller matrix of materials undoubtedly has found many applications in diverse research fields. Microscopy techniques that perform CD imaging by measuring the Jones matrix have been developed and are often applied to study the optical properties of crystals (Fig. 1.5(a)) [24, 28]. On the other hand, Mueller matrix microscopy is widely used for characterizing the polarimetric properties of various samples at millimeter scale [25, 29], micrometer scale [26, 30, 31], and nanometer scale [27, 32] (Figs. 1.5(b-d)). The use of multiple PEMs or the dual rotating compensators in the optical setup determines the detection scheme of Mueller matrix microscopy. In the case of using multiple PEMs, a photomultiplier is usually employed to keep pace with the high modulation frequency of the PEMs (operated at around 50 kHz) [29] and thus a scanning-based detection scheme is required. Alternatively, if the dual rotating compensators are employed, the frame rate of a camera is comparable with the frequency of the polarization modulation such that the sample can directly be imaged on the camera without any scanning process [30].
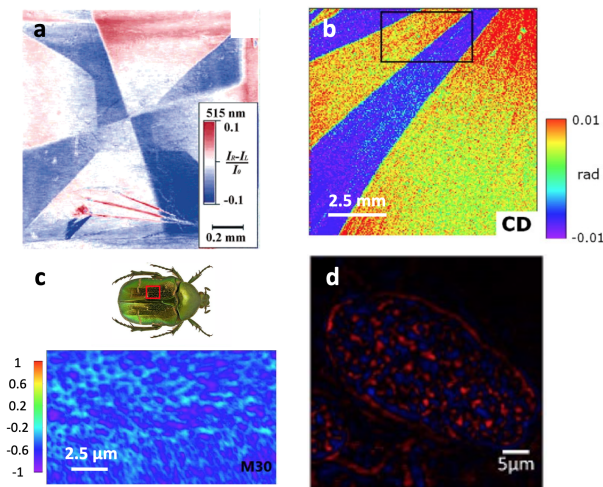


**Figure 1.5:** (a) CD image of Crystal of 1, 8-dihydroxyanthraquinone obtained using Jones formalism. Reprinted with permission from reference [24]. Copyright 2003, American Chemical Society. (b) CD image of Polycrystalline film of benzil from Mueller matrix microscopy. Reprinted with permission from reference [25]. Copyright 2010, Elsevier. (c) CD image of the exoskeleton of a *Cetonia Aurata* beetle from Mueller matrix microscopy. Adapted with permission from reference [26]. Copyright 2014, SPIE. (d) CD image of a Hek cell from Mueller matrix microscopy. Reprinted with permission from reference [27]. Copyright 2020, The Optical Society.

### 1.4.3 Confocal CD Microscopy

Confocal microscopy is an imaging technique extensively used in biology and material science. Its ability to perform optical sectioning enables the reconstruction of three-dimensional structures within a thick specimen. Confocal microscopy also attains higher image contrast and spatial resolution over traditional wide-field microscopy methods. This is achieved by positioning a spatial pinhole at the conjugate plane prior to the detector such that the out-of-focus light is rejected and cannot be recorded in the image. However, this improvement in contrast and resolution is at the expense of the reduced intensity on the detector, which may need to be compensated by other means like prolonging the exposure time or increasing the laser power.

To adapt the confocal microscopy technique to CD detection, a PEM is commonly employed to temporally modulate the polarization state of the excitation light. During the modulation, the polarization state continuously alters from left circular polarization to right circular polarization. The specimen is thus illuminated by the LCPL and RCPL successively while being raster-scanned. Finally, the difference in transmission of LCPL and RCPL is calculated for the image of the CD distribution. Confocal CD microscopy has been applied for the investigation of various types of samples, such as polymers [33], metal-organic frameworks [34], and even planar chiral nanostructures [35, 36]. The CD images are summarized in Fig. 1.6. Although the resolution of the confocal CD microscopy is still diffraction-limited, it is still better compared to the conventional CD wide-field microscopy methods.
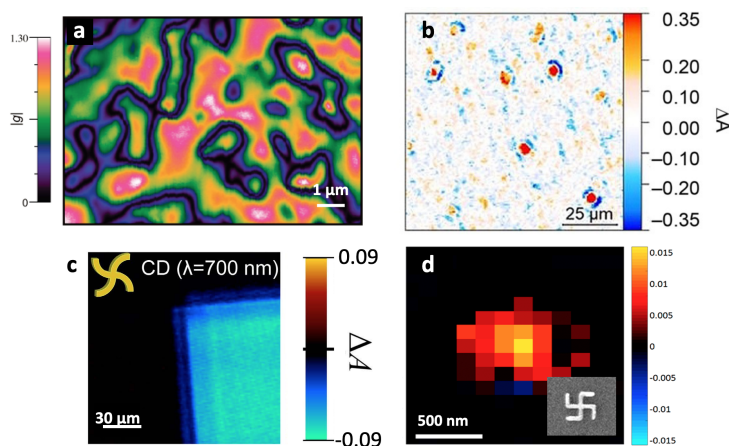


**Figure 1.6:** CD images obtained by confocal CD microscopy. (a) CD image of the chiral polyfluorene polymer film. Reprinted with permission from reference [33]. Copyright 2011, American Chemical Society. (b) CD image of chiral metal-organic frameworks. Reprinted with permission for reference [34]. Copyright 2011, Wiley. (c) CD image of swirl-shaped gold nanostructures. Reprinted with permission from reference [35]. (d) CD image of gold gammadion nanostructures. Reprinted with permission from reference [36]. Copyright 2018, American Chemical Society.

### 1.4.4 Nonlinear CD Microscopy

As an alternative to typical confocal microscopy techniques, nonlinear microscopy has found rich applications in a variety of biological research fields due to its unique advantages for biological imaging [37, 38]. In nonlinear microscopy, the laser beam with a wavelength longer than that required for one-photon excitation is focused at the sample plane by microscope optics. Using long wavelengths (e.g. in near-infrared regime) for illumination allows for deep penetration into the biological sample. In addition, owing to the low linear absorption rate in the out-of-focus area, the excitation volume within the sample significantly decreases compared to typical wide-field and confocal microscopy methods. This highly-confined excitation volume not only suppresses photodamage but also reduces the signals from out-of-focus areas. Thus, the spatial resolution of nonlinear microscopy is enhanced in a similar way to that in typical confocal microscopy but without a spatial pinhole positioned in front of the detector. Apart from absorption, multiple photons can be scattered at the same time and converted into one single photon. This phenomenon is known as the optical harmonic generation. In most cases, the signals detected in the nonlinear microscopy are the two-photon fluorescence (TPF) and the second-harmonic generation (SHG), which are based on the simultaneous absorption and scattering of two photons that have half of the energy required for one-photon excitation, respectively.

When incorporating with circular polarization excitation, TPF and SHG microscopy are able to probe the chirality by detecting the CD-dependent nonlinear signals, namely the TPF-CD and SHG-CD. TPF-CD microscopy has been experimentally demonstrated and applied to study the local organization of the chiral polyfluorene [39]. Regarding SHG-CD microscopy, the applications mainly focus on characterizing the chirality of macromolecular systems with ordered assemblies [40–47]. The CD images of these two nonlinear CD microscopy are summarized in Fig. 1.7. Both TPF-CD and SHG-CD microscopy techniques offer fair spatial resolution and selectivity for imaging local chiral domains. It is worth noting that, in contrast to the weak linear CD response, SHG-CD is electric-dipole allowed such that its magnitude becomes comparable with that of the linear dipole absorption [48]. However, because the generation of SHG requires the structures to be non-centrosymmetric (i.e. the lack of inversion symmetry), the applications of SHG-CD imaging is limited to the chiral samples with non-centrosymmetry.
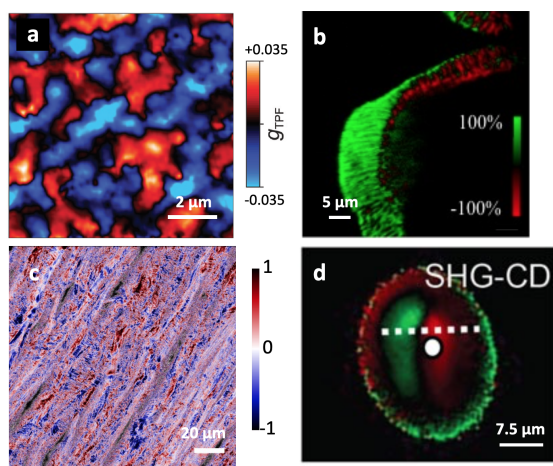
**Figure 1.7:** (a) TPF-CD image of chiral polyfluorene film. Reprinted with permission from reference [39]. Copyright 2012, American Chemical Society. (b) SHG-CD image of collagen. Adapted with permission from reference [42]. Copyright 2013, The Optical Society. (c) SHG-CD image of collagen. Reprinted with permission from reference [47]. Copyright 2019, The Optical Society. (d) SHG-CD image of starch granules. Reprinted with permission from reference [43]. Copyright 2014, Wiley.

### 1.4.5 Photothermal CD Microscopy

Photothermal techniques rely on the detection of temperature-dependent variation in physical parameters as light illuminates the sample and generates heat in the local environment [49, 50]. For example, the thermally-induced refraction index gradient can behave like a concave lens and thus diverges the laser beam, leading to a variation in the transmitted intensity recorded by a pinhole detector. By monitoring this "thermal lens effect" within an absorbing sample, thermal lens microscopy has found many applications in microfluidics [51] and bioimaging [52, 53]. The detection of the thermal lens effect is commonly achieved by using the coaxial two-beam configuration, namely the combination of a pump beam and a probe beam [51–54]. Since the pump beam is used to launch the heating process, its wavelength is selected to match the absorption band of the sample. On the contrary, the wavelength of the probe beam is chosen to achieve the minimal absorption of the sample. Due to the thermal lens effect, the probe beam diverges and the decrease of transmitted intensity is recorded by a photodiode as the signal. Apart from light divergence, a heated sample also scatters the probe beam differently compared to the normal sample and the additional scattering signals can be detected based on the heterodyne optical method [55] for further investigation. Applications of photothermal heterodyne imaging can be found in the detection of gold nanocluster detection [56] and single-molecule [57].

Thermal lens microscopy has been implemented to detect CD signals by introducing circular polarization excitation for chiral analysis on a microchip [58, 59]. However, it should be noted that the term "CD thermal lens microscopy" in reference [58] and [59] is supposed to be recognized as "thermal lens microspectroscopy," as it is a thermal lens spectroscopic method incorporating with a microscope objective. The ability of thermal

lens microscopy to image the spatial CD distribution has not yet been experimentally demonstrated. In contrast, the CD distribution of metal nanoparticles mapped by the photothermal heterodyne imaging method has been recently reported [60]. The corresponding photothermal-CD image is shown in Fig. 1.8(b).
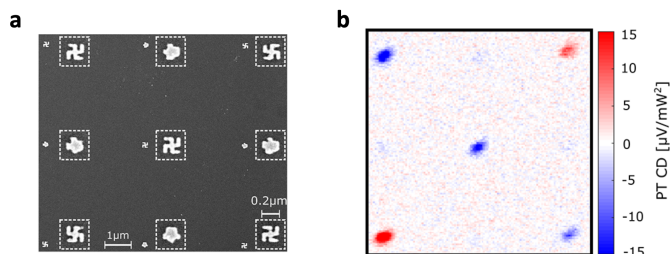


**Figure 1.8:** (a) Scanning electron microscope image of achiral, left and right-handed gammadion nanostructures. (b) Photothermal-CD image of the gammadion nanostructures shown in (a). Reprinted with permission from reference [60]. Copyright 2019, American Chemical Society.

## 1.4.6 Chiral Scanning Near-Field Optical Microscopy

The near field that carries the high spatial frequency information on an object fades out when the electromagnetic wave propagates more than one wavelength away. In scanning near-field optical microscopy (SNOM), this near field is detected by a metallic tip positioned very close to the sample to investigate the sample surface at sub-diffracted limit resolution. A detailed discussion on SNOM is given in Sec. 1.5.1.

SNOM has also been applied to collect CD signals when incorporating with circularly polarized excitation, which we term chiral SNOM [61–66]. Since chiral SNOM is a variant of SNOM, it enables the investigation of local CD distribution at a spatial resolution beyond the diffraction limit. Near-field CD distribution of plasmonic nanostructures [61–64] and polymers [65, 66] obtained by chiral SNOM have been reported, as summarized in Fig. 1.9. However, the whole optical setup of chiral SNOM is relatively complex. The scanning nature of SNOM also renders the measurement time-consuming and the investigation is restricted on the surface of the sample.
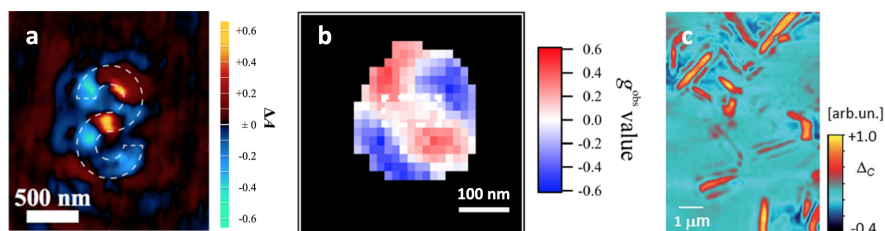


**Figure 1.9:** CD images obtained by chiral SNOM. (a) Near-field CD distribution of a chiral metal nanostructure. Reprinted with permission from reference [62]. Copyright 2013, American Chemical Society. (b) Near-field two-photon CD image of a gold rectangle. Reprinted with permission from reference [64]. Copyright 2016, American Chemical Society. (c) Near-field CD image of J-aggregates. Adapted from reference [66] with permission from The Royal Society of Chemistry.

## 1.5 Super-Resolution Optical Microscopy

To overcome the physical limitation imposed by the diffraction of light on the optical resolution, scientists have developed various microscopy modalities, which are based on the detection of the optical evanescent field, the control of the molecular emission process, and the manipulation of the illumination field. We introduce these super-resolution microscopy methods in the following sections.

### 1.5.1 Scanning Near-Field Optical Microscopy

The detection of an electromagnetic wave in the near field reveals the high spatial frequency information that fades out as the wave travels to the far field. The microscopy technique that detects this evanescent wave is known as SNOM or NSOM (near-field scanning optical microscopy) [67–69]. Because this evanescent wave decays exponentially within a distance less than the wavelength of light, a nanoscopic probe positioned very close to the investigated sample is requisite in SNOM. This requirement is usually fulfilled with two types of tip configuration: a probe tip with and without an aperture, corresponding to aperture SNOM and apertureless SNOM, respectively.

In aperture SNOM, a miniature hole situated at the end of the probe tip is able to confine the electromagnetic field in the near-field regime. Such configuration is commonly realized by a metal-coated tapered fiber, which can illuminate the sample surface or capture the optical signal in the near field and thus offers wide flexibility of different operation modes such as excitation, collection, and excitation-collection mode (Fig. 1.10(a)). For apertureless SNOM, a tapered metallic apex is used to perturb (scattering-SNOM) or enhance (tip-enhanced SNOM) the local electromagnetic field upon far-field illumination. The scattered light is then collected and transmitted to a detector via far-field optics (Fig. 1.10(b)). In both aperture SNOM and apertureless SNOM, the designed tips raster scan over the sample surface to map the whole region of interest at sub-wavelength resolution. SNOM has found many applications in various research subjects such as fluorescence imaging of biological samples [70–72] and near-field Raman spectroscopy [73]. Besides, SNOM can also incorporate with circular polarization excitation to map CD distribution, which is detailed in Sec. 1.4.6.
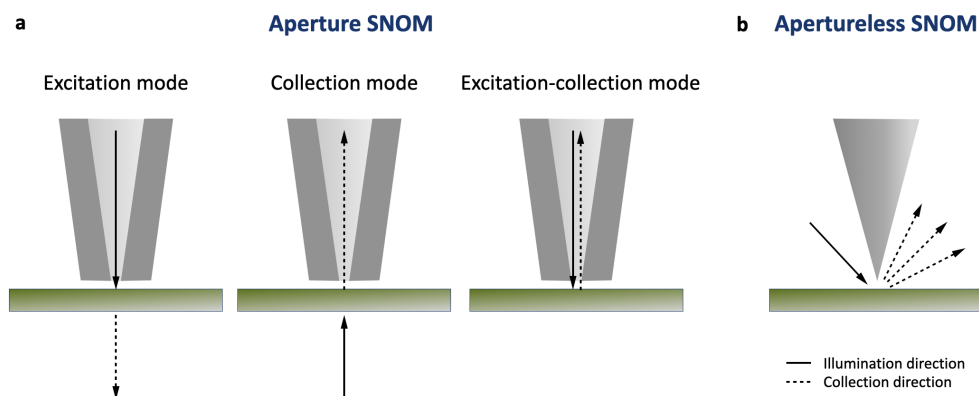
**Figure 1.10:** Schematics of (a) aperture SNOM with different operation modes and (b) apertureless SNOM.

### 1.5.2 Single-Molecule Localization Microscopy

The ability to control the photoswitching kinetics of fluorophores has brought traditional fluorescence microscopy into a new era. Due to the diffraction of light, two similar fluorophores that are spaced below the Abbe limit cannot be recognized as two separated spots, leading to the diffraction-limited resolution. Intuitively, if one can address the emission of each fluorophore individually (in analogy to switching only one of many bulbs in the dark and repeating this process several times), two neighboring fluorophores can be, in principle, distinguished and the position of those fluorophores can precisely be estimated. Owing to the studies of various fluorescent labels, this condition is achieved by using photoswitchable fluorophores, enabling related imaging techniques like stochastic optical reconstruction microscopy (STORM) and photoactivated localization microscopy (PALM) [74–77]. The photoswitchable fluorophores attached to the investigated sample are excited stochastically and sparsely to ensure the emission of fluorophores can be detected separately in each imaging frame. The locations of individual fluorophores are then calculated by fitting the emission profile with a two-dimensional Gaussian function, which provides the precision below the diffraction limit. By repeating this imaging process numerous times, the positions of the fluorophores are reconstructed from the acquired images, giving rise to the super-resolved image (Fig. 1.11). Both STORM and PALM follow the aforementioned principle to localize individual fluorophores. The major difference between these two imaging methods is that STORM uses photoswitchable fluorescent dyes (such as Cy3 and Cy5) and PALM mainly uses photoactivatable fluorescent proteins (such as Dronpa and PA-GFP) to label the investigated sample. The lateral resolution of STORM and PALM is reported in the range of 20 to 50 nm [74–77].
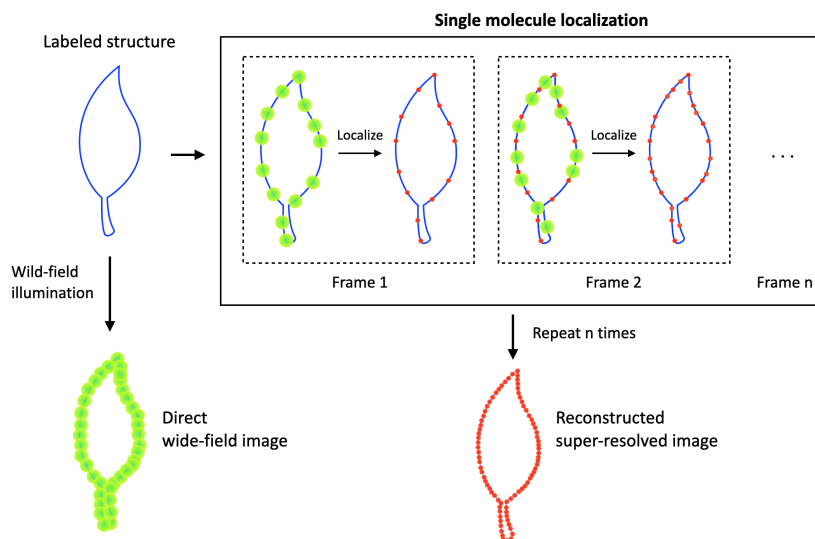
**Figure 1.11:** Principle of STORM and PALM to localize and reconstruct the positions of individual fluorophores.

### 1.5.3 Stimulated Emission Depletion Microscopy

In conventional fluorescence microscopy, the focal spot of a laser beam used for excitation spreads out due to the diffraction of light. Fluorophores situated in this excitation spot are excited simultaneously, rendering those fluorophores indiscernible. Better resolution can be obtained if a subset of fluorophores or even a single fluorophore is excited individually as the laser beam scans over the fluorescently labeled sample. This can be achieved by introducing a doughnut-shaped beam with zero intensity at the center to de-excite the fluorophores that are situated in the outer region of the original excitation beam (Fig. 1.12). Thus, only the fluorophores that locate in the center of the doughnut-shaped beam remain excited and emit the fluorescence after this depletion process. The stimulated emission occurs at a longer wavelength with respect to the desired fluorescence emission and therefore can be spectrally separated by optical components. The excitation and depletion beams are aligned to scan across the fluorescently labeled sample to generate the super-resolved image. The microscopy developed based on the aforementioned principle is known as stimulated emission depletion microscopy (STED) [78–80]. The resolution of STED microscopy mainly relies on the laser intensity of the depletion beam because it relates to the size of the zero point in the doughnut-shaped beam: the higher the laser intensity is applied, the smaller size of the zero point and better resolution are obtained. In STED microscopy, spatial resolution between 20 and 50 nm has been experimentally demonstrated [78–80]. An extremely high resolution of 2.4 nm is reported when a diamond with nitrogen-vacancy centers is observed [81].
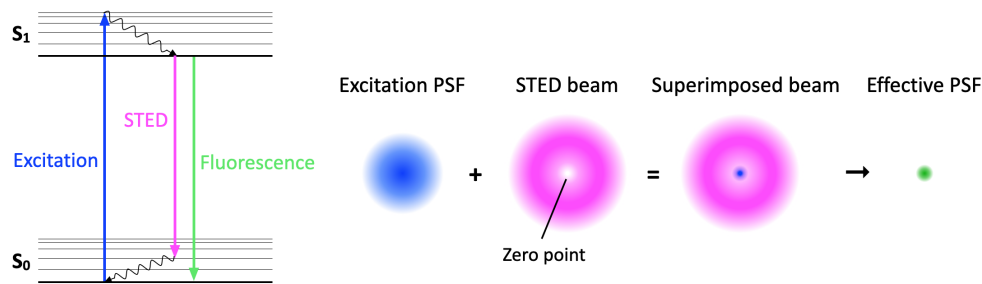
**Figure 1.12:** Principle of STED. The doughnut-shaped beam (STED beam) depletes the fluorophores situated in the region that overlaps the first excitation beam, leading to a smaller effective PSF compared to the original one.

### 1.5.4 Structured Illumination Microscopy

Compared to the aforementioned super-resolution microscopy techniques, structured illumination microscopy (SIM) is distinct as it applies stripe-like illumination to achieve sub-wavelength resolution (Fig. 1.13). In super-resolution SIM (hereinafter referred to as SIM), periodic intensity patterns are employed to illuminate the fluorophores. This forms frequency-mixing patterns, i.e. moiré patterns (Fig. 1.13(b)), that down-modulate the high spatial frequency information on the fluorophore distribution. These frequency-mixing patterns can be then captured by a diffraction-limited optical system and form a series of subimages. The high spatial frequency information on the fluorophore distribution is later decrypted from those subimages in Fourier space with the prior knowledge, such as the spatial frequency, initial phase, and orientation, of the illumination patterns. In principle, the spatial frequency of the periodic illumination patterns determines the resolution of SIM. Since the generation of the illumination patterns is mainly dependent on the superposition of far-field waves, the minimal spatial frequency that can be attained is inevitably restricted by the diffraction of light. The theoretical resolution offered by SIM is thus approximately two-fold superior to that of conventional wide-field microscopy methods. Practically, the resolution of SIM is able to reach 100 nm in visible range [82] and can further be improved to 50 nm if the nonlinear effect of the fluorescence [83] or plasmonic nanostructures is applied [84–86]. One advantage of SIM stems from its wide-field illumination scheme. Without the need for scanning over the sample, SIM in theory possesses higher imaging speed compared to other super-resolution microscopy methods and is therefore preferable to dynamic analysis such as live-cell imaging [87, 88]. Although STORM and PALM are also based on wide-field illumination, numerous frames are necessary to reconstruct the emission from individual fluorophores, which
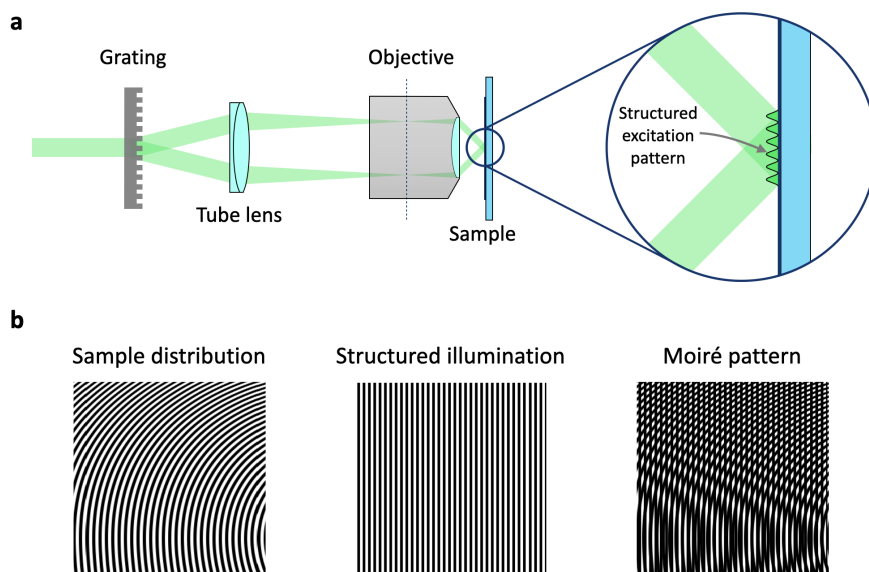
**Figure 1.13:** Principle of SIM. (a) Schematics of the configuration to generate the structured excitation pattern. (b) The superposition of the sample distribution and periodic structured illumination generates the moiré pattern that down-modulates high spatial frequency information.

inevitably decreases the imaging speed and leads to low throughput. Besides, SIM does not have special requirements for sample preparation compared to other super-resolution microscopy techniques. Samples that are suitable for conventional fluorescence microscopy can be, in principle, applied in SIM straightforwardly since the difference between SIM and conventional fluorescence microscopy is merely the structured illumination scheme. Special variants of SIM have been developed to effectively achieve structured illumination by manipulating the polarization distribution on the sample plane [89] or to observe the inner dipole orientation of a given sample [90]. Nevertheless, it should be noted that applying structured illumination to achieve resolution improvement is not feasible for coherent imaging methods [91]. The detected signals should be incoherent, which is exactly the case for fluorescence, in order to obtain the desired resolution improvement over the typical wide-field microscopy.

Overall, the essential idea of modulating the fluorescence emission by applying the periodic illumination patterns offers the possibility to visualize various fluorescence-dependent signals at sub-wavelength resolution. The principle of conventional SIM is thus of great importance to the basis of the proposed chiral SIM method and will be explicitly discussed in Sec. 2.4.

# Chapter 2

# Fundamentals

## 2.1 Light and Polarization

Light, which is an electromagnetic wave traveling in space, consists of oscillating electric and magnetic fields. Considering the solutions to electromagnetic wave equations, the electric field vector of a time-harmonic monochromatic plane wave propagating in an isotropic homogeneous medium along the $z$-direction can be expressed by

$$\tilde{\mathbf{E}} = \tilde{E}_x\hat{\mathbf{x}} + \tilde{E}_y\hat{\mathbf{y}} = (E_{0x}e^{i\varphi_x}\ \hat{\mathbf{x}} + E_{0y}e^{i\varphi_y}\ \hat{\mathbf{y}})e^{i(kz-\omega t)}, \tag{2.1}$$

which is a superposition of two orthogonal components along $x$- and $y$-direction (Fig. 2.1). Here, the symbol ~ denotes the corresponding complex field. $\hat{\mathbf{x}}$ and $\hat{\mathbf{y}}$ are the unit vectors along the $x$- and $y$-axis, respectively. $k$ is the wavevector along $z$-direction and $\omega$ is the angular frequency of light. $E_{0x}$ ($E_{0y}$) indicates the amplitude and $\varphi_x$ ($\varphi_y$) initial phase of the $x$-component ($y$-component) of the electric field, respectively. The trace of the electric field vector, which is determined by the ratio of $E_{0y}$ to $E_{0x}$ and the initial phases $\varphi_x$ and $\varphi_y$, defines the polarization state of the light. In principle, this trace
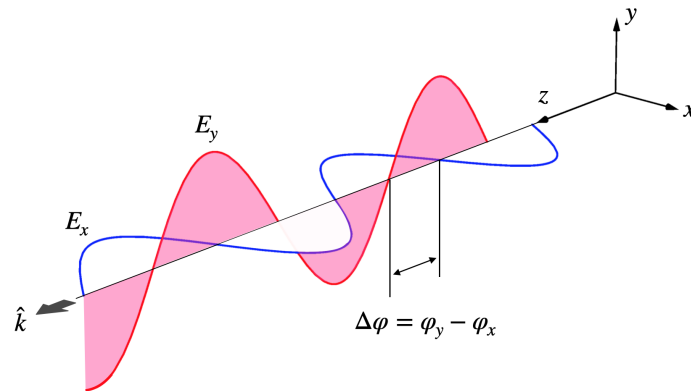


**Figure 2.1:** Illustration of a propagating electromagnetic plane wave. The electric field components $E_x$ and $E_y$ are indicated by blue and red lines, respectively. The phase difference of $E_x$ and $E_y$ is defined by $\Delta\varphi = \varphi_y - \varphi_x$.

can be portrayed by the so-called polarization ellipse (detailed derivation is referred to Appendix A):

$$(\frac{E_x}{E_{0x}})^2 + (\frac{E_y}{E_{0y}})^2 - 2\frac{E_x E_y}{E_{0x} E_{0y}}\cos\Delta\varphi = \sin^2\Delta\varphi, \tag{2.2}$$

where $E_j = \mathrm{Re}(\tilde{E}_j) = E_{0j}\cos(kz - \omega t + \varphi_j)$ is the physical electric field with $j = x, y$. $\Delta\varphi = \varphi_y - \varphi_x$ the phase difference between the electric field components. The range of $\Delta\varphi$ is defined as $-\pi < \Delta\varphi \leq \pi$. According to Eq. 2.2, the polarization states of a plane wave can be classified into three categories:

**Elliptically Polarized Light**

As its name suggests, the polarization ellipse of Eq. 2.2 describes an elliptical route of the electric field vector, as plotted in Fig. 2.2(a), and typically is known as elliptically polarized light (EPL). For a given ratio of $E_{0y}$ to $E_{0x}$ and $\Delta\varphi$, the orientation of the EPL $\nu$ and ellipticity $\eta$ are depicted by the relations [92]

$$\tan 2\nu = \tan 2\xi \cos\Delta\varphi, \qquad 0 \leq \nu \leq \pi, \tag{2.3}$$

$$\sin 2\eta = \sin 2\xi \sin\Delta\varphi, \qquad -\frac{\pi}{4} < \eta \leq \frac{\pi}{4}, \tag{2.4}$$

where $\xi = \tan^{-1}|\frac{E_{0y}}{E_{0x}}|$ $(0 \leq \xi \leq \frac{\pi}{2})$ is an auxiliary angle that defines the ratio between $E_{0x}$ and $E_{0y}$. During the propagation, the shape or the aspect ratio of the oval is determined by $\eta$. Meanwhile, EPL can rotate in two opposite ways when it propagates towards an observer. Based on the convention of the observer's view (i.e. the observer looks towards the source and against the propagation direction of the light), counter-clockwise rotation corresponds to left-elliptically polarized light (LEPL) and clockwise one corresponds to right-elliptically polarized light (REPL). The handedness of EPL is also denoted by the sign of $\eta$, where the negative sign denotes LEPL and the positive sign is for REPL.

**Linearly Polarized Light**

When the $x$- and $y$-component of the electric field is in phase ($\Delta\varphi = 0, \pi$), Eq. 2.2 is simplified as

$$(\frac{E_x}{E_{0x}} \mp \frac{E_y}{E_{0y}})^2 = 0, \tag{2.5}$$

which implies that the electric field vector points to a direction determined by $\Delta\varphi$ and $\xi$, and moves back and forth (Fig. 2.2(b) and (c)). This polarized light is termed LPL because the trace of the electric field is always along a line.

**Circularly Polarized Light**

If both $x$- and $y$-components are 90° out of phase ($\Delta\varphi = \pm\frac{\pi}{2}$) when having the same amplitudes ($E_{0x} = E_{0y} = E_0$), the trace of the electric field is reduced to

$$E_x^2 + E_y^2 = E_0^2, \tag{2.6}$$

which describes a rotating circle. This polarized light is therefore termed CPL. Similar to EPL, the handedness of the CPL is characterized when the light is traveling towards an observer. It corresponds to LCPL if the light rotates anticlockwise (Fig. 2.2(d)). If the light rotates clockwise, it is referred to as RCPL (Fig. 2.2(f)). CPL, as well as EPL, shows a helical trajectory depending on its handedness in the space and is thus regarded as chiral light.
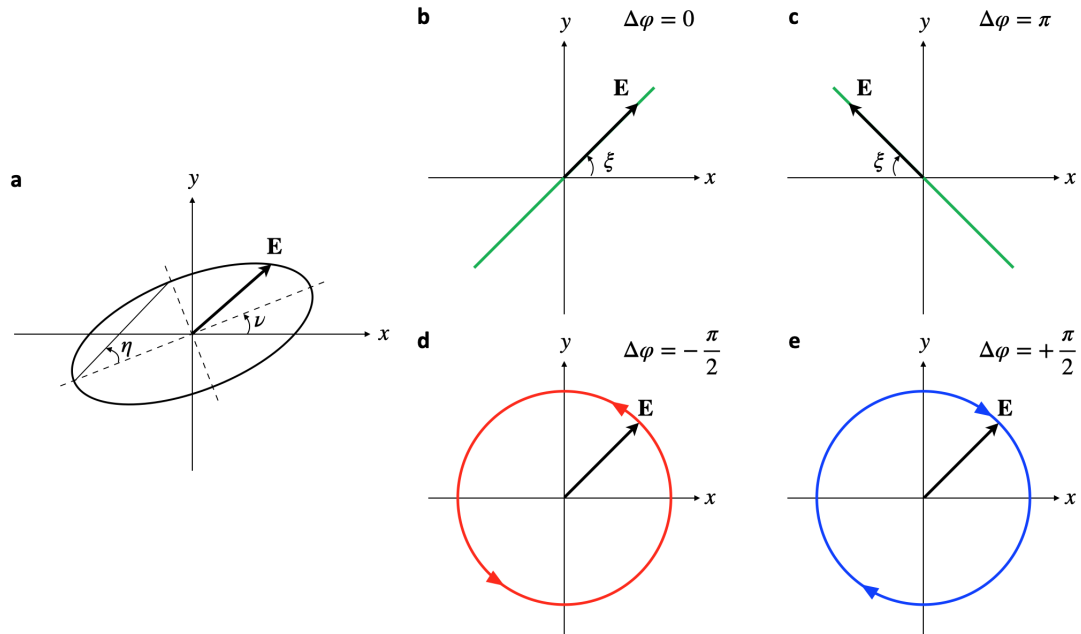


**Figure 2.2:** Illustration of the polarization states. (a) EPL is depicted by the polarization ellipse. $\nu$ is the orientation angle and $\eta$ is the ellipticity, which describes the rotation and shape of the polarization ellipse. (b) +45 °LPL. (c) −45 °LPL. (d) LCPL (e) RCPL. The handedness of EPL and CPL is determined based on the convention of the observer's view.

## 2.2 Optical Chirality

In 2010, a physical quantity called optical chirality (OC), originally proposed by the mathematical physicist Lipkin in 1964 [93] but later dismissed due to the lack of physical interpretation, was reemphasized by Tang and Cohen [16] and is later used by researchers to specify the chirality of an optical field. The general form of OC in vacuum is given by

$$C \equiv \frac{\varepsilon_0}{2} \mathbf{E} \cdot (\nabla \times \mathbf{E}) + \frac{1}{2\mu_0} \mathbf{B} \cdot (\nabla \times \mathbf{B}), \qquad (2.7)$$

where $\varepsilon_0$ and $\mu_0$ are the permittivity and permeability of free space, respectively. $\mathbf{E}$ and $\mathbf{B}$ are the real part of the complex electric field $\tilde{\mathbf{E}}$ and magnetic field $\tilde{\mathbf{B}}$, respectively. Considering a monochromatic time-harmonic electromagnetic wave, Eq. 2.7 can be simplified as [94]

$$C = \frac{2\omega}{\varepsilon_0} \mathrm{Im}(\tilde{\mathbf{E}}^* \cdot \tilde{\mathbf{B}}). \qquad (2.8)$$

OC is a time-even pseudo-scalar that helps us to identify the chiral property of electromagnetic fields: the sign of OC determines the handedness of the electromagnetic fields and the magnitude of OC relates to the polarization helicity of the electromagnetic fields [95]. As Eq. 2.8 suggests, there are two requisites to achieve nonzero OC: (i) some components of the electric field are parallel to the magnetic field and (ii) the relative phase of the parallel electric and magnetic components should not be zero or the multiple of $\pi$. In the far field, this condition occurs when the light is circularly polarized or elliptically polarized. Furthermore, the relation between OC and the CD can be illustrated when we consider the absorption of a chiral molecule. When the chiral molecule is subjected to an electromagnetic field, the electrons of the molecule are driven by these oscillating fields, inducing the electric dipole moment $\tilde{\mathbf{p}}$ and magnetic dipole moment $\tilde{\mathbf{m}}$ within the molecule. The induced dipole moments can be expressed as [16]

$$\tilde{\mathbf{p}} = \tilde{\alpha}\tilde{\mathbf{E}} - i\tilde{G}\tilde{\mathbf{B}}, \qquad (2.9)$$

$$\tilde{\mathbf{m}} = \tilde{\chi}\tilde{\mathbf{B}} + i\tilde{G}\tilde{\mathbf{E}}, \qquad (2.10)$$

where $\tilde{\alpha}$ is the electric polarizability, $\tilde{\chi}$ the magnetic susceptibility, and $\tilde{G}$ the isotropic mixed electric-magnetic dipole polarizability or chiral polarizability. It is worth noting that the local complex fields $\tilde{\mathbf{E}}$ and $\tilde{\mathbf{B}}$ also contribute to $\tilde{\mathbf{m}}$ and $\tilde{\mathbf{p}}$, respectively, and the

extent of the contributions is indicated by $\tilde{G}$. Considering the induced dipole moments, the absorption rate of the chiral molecule can be expressed by [16]

$$a = \langle \mathbf{E} \cdot \dot{\mathbf{p}} + \mathbf{B} \cdot \dot{\mathbf{m}} \rangle, \tag{2.11}$$

where $\dot{}$ denotes the derivative of a quantity with respect to time and $\langle\ \rangle$ means the time-average of a given function. $\mathbf{p} = \mathrm{Re}(\tilde{\mathbf{p}})$ and $\mathbf{m} = \mathrm{Re}(\tilde{\mathbf{m}})$ are the physical electric and magnetic dipole moments, respectively. Taking into account the harmonic time dependence $e^{i\omega t}$, we can rewrite Eq. 2.11 with the identities of the complex number [94]

$$a = \frac{\omega}{2}(\alpha''|\tilde{\mathbf{E}}|^2 + \chi''|\tilde{\mathbf{B}}|^2) + G''\omega \mathrm{Im}(\tilde{\mathbf{E}}^* \cdot \tilde{\mathbf{B}}), \tag{2.12}$$

where $\alpha''$, $\chi''$, and $G''$ are the imaginary part of $\tilde{\alpha}$, $\tilde{\chi}$, and $\tilde{G}$. Since the magnetic response is usually weak for most of the molecules, the second term on the right-hand side of Eq. 2.12 can be neglected. Then, by substituting Eq. 2.8 into Eq. 2.12, we can obtain

$$a = \frac{2}{\varepsilon_0}(\omega U_e \alpha'' - C G''), \tag{2.13}$$

where $U_e$ is the time-average electric energy density of the optical field given by

$$U_e = \frac{\varepsilon_0}{4}|\tilde{\mathbf{E}}|. \tag{2.14}$$

The difference in the absorption of LCPL and RCPL, which indicates CD, is given by

$$\Delta a = a_L - a_R$$
$$= \frac{2}{\varepsilon_0}\left[(U_{e,L} - U_{e,R})\alpha'' - (C_L - C_R)G''\right], \tag{2.15}$$

where the subscripts $L$ and $R$ represent LCPL and RCPL, respectively. Because the intensity of LCPL and RCPL is the same, $U_{e,L} - U_{e,R} = 0$ and the first term of Eq. 2.15 is eliminated. Next, $C_L$ and $C_R$ in vacuum can be calculated according to Eq. 2.8 [96]

$$C_{L,R} = \pm C_{\mathrm{CPL}} = \pm \frac{\epsilon_0 \omega}{2c} E_0^2, \tag{2.16}$$

where $E_0$ denotes the electric field amplitude of the CPL. By substituting Eq. 2.16 into Eq. 2.15, the CD is given by

$$\Delta a = -\frac{4}{\varepsilon_0} C_{\text{CPL}} G''.$$ (2.17)

The dissymmetry factor $g_{\text{CPL}}$ can also be expressed as

$$g_{\text{CPL}} = \frac{a_L - a_R}{\frac{1}{2}(a_L + a_R)} = -\frac{2 C_{\text{CPL}} G''}{\omega U_e \alpha''},$$ (2.18)

where $U_e = U_{e,L} = U_{e,R}$. In Eq. 2.18, $G''$ indicates the chirality of the molecule, where $G'' = 0$ links to achiral species and the sign of $G''$ corresponds to the handedness of the molecular chiral domains.

## 2.3 Fluorescence Microscopy

### 2.3.1 Physics of Fluorescence

Fluorescence is a manifestation of the interaction between light and molecules that are usually referred to as fluorophores or fluorescent dyes. The physics behind this phenomenon involves three basic events: excitation of a molecular system, vibrational relaxation of excited state electron, and the emission of a longer-wavelength photon (Fig. 2.3(a)). As the molecule absorbs an incoming photon, the electron within is promoted from the ground state ($S_0$) to a higher energy level, which is usually the first excited state ($S_1$). After a short duration, the electron will relax to the lowest vibrational level of $S_1$ and lose part of its energy. Finally, the excited electron returns to the ground state and releases the stored energy by emitting a photon. Because the electron energy is partially dissipated during vibrational relaxation, the emitted photon has lower energy compared to the absorbed one. This leads to the difference in the peak positions of the excitation and the emission spectra, known as the Stokes shift (Fig. 2.3(b)). The whole process of fluorescence and the characteristic time are illustrated by a simplified Jablonski diagram shown in Fig. 2.3(a).

Fluorescence plays a crucial role in many practical applications, especially in the field of biological imaging. A large variety of fluorescent probes such as inorganic nanoparticles, organic dyes, and fluorescent proteins are developed to meet the demands of various imaging applications [97]. Targets inside a complex biological assembly can

be specified after the labeling process. The stained components can stand out from the dark background during the imaging process, which tremendously increases the image contrast. Besides, the redshift of the fluorescence emission permits the selection of desired fluorescence signals using filters or dichroic mirrors. In summary, by offering high contrast, selectivity, and sensitivity, fluorescence microscopy becomes very popular and indispensable in biological science.
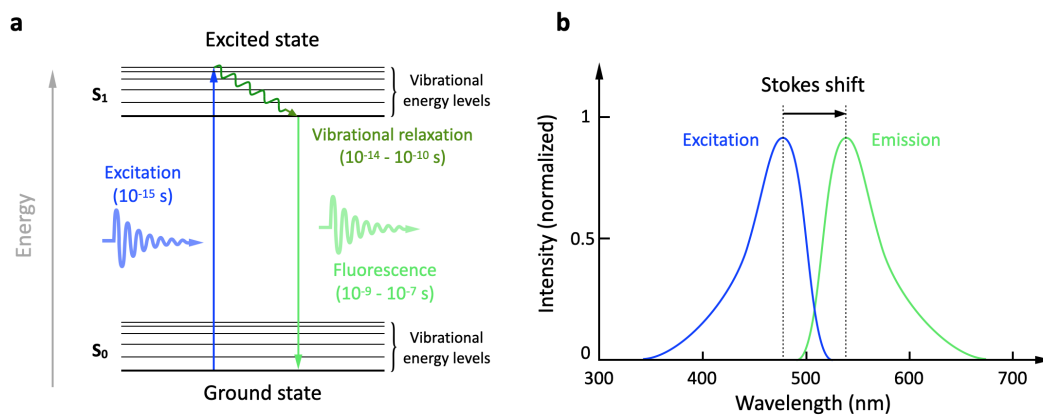


**Figure 2.3:** (a) A simplified form of the Jablonski diagram for the fluorescence process. $S_0$ and $S_1$ denote the ground state and the first excited state, respectively. (b) Corresponding excitation and emission spectra for illustrating the Stokes shift.

### 2.3.2 Resolution of Conventional Fluorescence Microscopy

Resolution is an important metric to justify the capability of an optical imaging system. One of the common criteria to indicate the resolution is the Abbe diffraction limit. In 1873, the German physicist Ernst Abbe postulated that the image formation process can be elaborated using a periodic grating structure and then concluded that the resolution of an optical microscope is fundamentally limited due to the diffraction of light [98]. As light illuminates on the grating structure, it is deviated and forms individual diffraction orders separated by an angle (Fig. 2.4). The position where the diffracted light rays can interference constructively is mathematically described by

$$d \sin \theta_m = m\lambda, \tag{2.19}$$

where $d$ is the grating period and $\theta_m$ denotes the diffraction angle. $m$ indicates the diffraction order and $\lambda$ is the wavelength of the incident light. As implied by Eq. 2.19, $\theta_m$ can be larger than the acceptance angle of the imaging lens as $d$ becomes smaller. Thus, not all of the diffracted light rays can be captured by the imaging lens and interfere
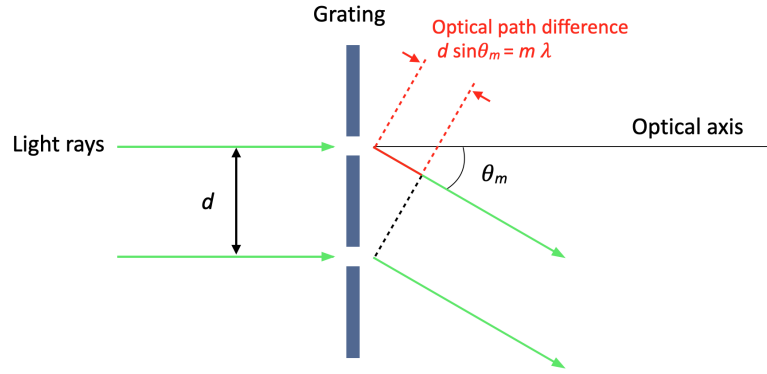
**Figure 2.4:** Illustration of light diffraction. $d$ denotes the grating period and $\theta_m$ is the diffraction angle of $m^{\text{th}}$ order. The constructive interference of the light rays will occur when the optical path difference equals the integral multiple of the wavelength of the incident light $\lambda$.

on the eventual image plane (Figs. 2.5(a) and (b)). This inevitably leads to a loss of the details of the grating image. Abbe suggested that the grating structure can be resolved if at least the $0^{\text{th}}$ and $1^{\text{st}}$ diffraction orders of the light are accepted by the imaging lens. In this regard, the diffraction angle of $1^{\text{st}}$-order $\theta_1$ should be half-acceptance angle $\alpha$ in order to obtain the minimal $d$

$$d = \frac{\lambda}{n \sin \alpha} = \frac{\lambda}{\text{NA}},\tag{2.20}$$

where NA denotes the numerical aperture of the imaging lens. Eq. 2.20 is interpreted as the minimal resolvable spacing of the grating structure and thus indicates the resolving power of the imaging system. Abbe also pointed out that one can resolve a finer grating, namely improving the resolution described by Eq. 2.20, if the light incidents at an angle with respect to the optical axis. By adjusting the incident angle, higher diffraction orders of the light that missed the imaging lens can thus be captured (Fig. 2.5(c)). Regarding this oblique illumination, the minimal $d$ can be expressed as

$$d = \frac{\lambda}{n(\sin \theta_1 + \sin \theta_i)},\tag{2.21}$$

by considering the incident angle of the light $\theta_i$. In the case of $\theta_i$ and $\theta_1$ being identical to $\alpha$ (for instance, the NA of the condenser and objective are the same), the resolution indicated by Eq. 2.20 is two-fold enhanced, leading to the celebrated Abbe diffraction limit

$$d_{\text{Abbe}} = \frac{\lambda}{2\text{NA}}.\tag{2.22}$$
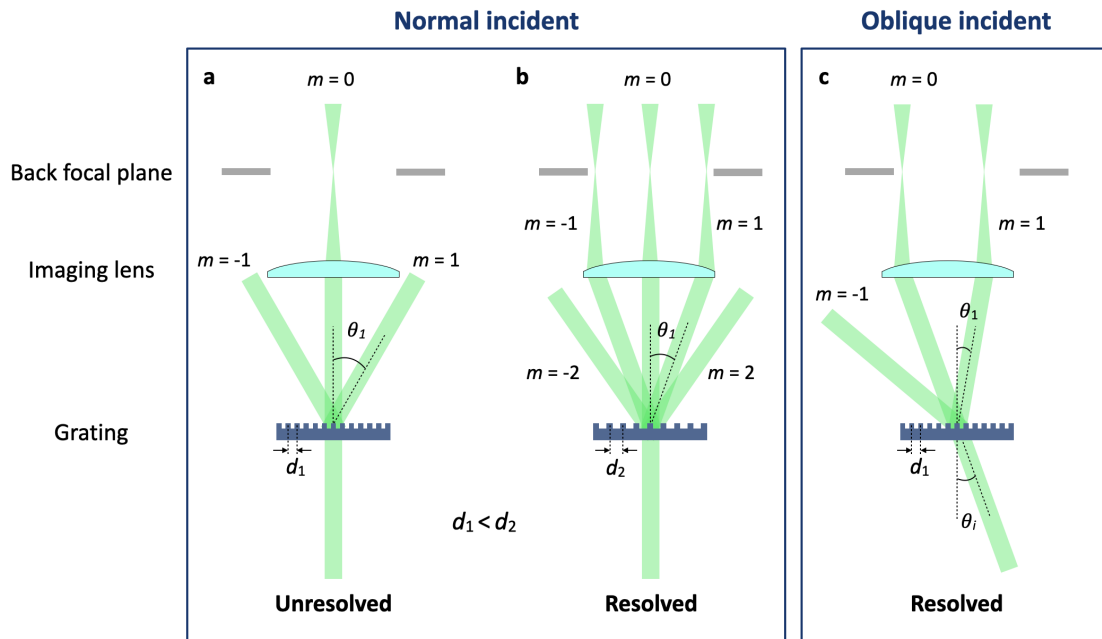
**Figure 2.5:** Illustration of Abbe's consideration for image formation. (a) $\pm 1^{\text{st}}$ order diffracted light cannot pass through the imaging lens because the grating period $d_1$ is small (or the spatial frequency is high). (b) As $d_1$ increases to $d_2$, $\pm 1^{\text{st}}$ order diffracted light can pass through the imaging lens. (c) Compared to (a), the $1^{\text{st}}$ order diffracted light can pass through the imaging lens if the light obliquely incidents on the grating with a period of $d_1$.

Since an arbitrary object can be considered as the superposition of the grating structures with different spatial frequencies, the Abbe diffraction limit is conventionally used to evaluate the resolving power of an imaging system. In the case of fluorescence microscopy, although the emission from fluorophores is incoherent, the image still has to be formed by the interference of the light rays collected by the imaging lens. Therefore, the diffraction limit can still be applied to indicate the resolution of fluorescence microscopy methods though the Abbe theory mainly considers the coherent imaging process [99].

Another useful way to assess the resolution of fluorescence microscopy is taking into account the point spread function (PSF). The PSF characterizes the response of an optical imaging system to a point light source, which, in the case of fluorescence microscopy, is the fluorophore since the size of a fluorophore is very small. In the imaging process, light emanating from a fluorophore is accepted by an imaging lens, usually an objective, and then relayed to the final image plane. However, the eventual image of the point source spreads out and forms a blurry spot with concentric ring patterns due to the diffraction of light. This is known as the PSF and has an approximated profile to an Airy pattern. Furthermore, considering multiple point sources on the sample plane, which usually represent the sophisticated structures of a fluorescently labeled sample, those blurry spots at the image plane may coincide when two adjacent point sources

are too close to each other. This undoubtedly imposes a limitation on the resolution of an optical microscope because two objects cannot be distinguished if the overlap is very large. The British physicist Lord Rayleigh proposed that two point objects are considered just resolved by the human eye if they are separated by the distance where the first maximum of one Airy pattern meets the first minimum of another Airy pattern (Fig. 2.6(a)). This is the famous Rayleigh criterion denoted by [100]

$$d_{\text{Rayleigh}} = \frac{0.61\lambda}{\text{NA}}. \tag{2.23}$$

Two point objects are considered unresolved when they are distanced below $d_{\text{Rayleigh}}$ because the Airy patterns are overlapped very much (Fig. 2.6(b)). If these two point objects are separated larger than $d_{\text{Rayleigh}}$, the corresponding Airy patterns can be recognized (Fig. 2.6(c)) and therefore it is considered well-resolved. Although the Rayleigh criterion is sort of arbitrary because "can be resolved by the human eye" is a very subjective standard, it is close to the Abbe diffraction limit and still widely used to illustrate the resolution of an optical imaging system.

In conclusion, for traditional optical microscopy techniques, it is unfeasible to discriminate two different objects when they are spaced less than $d_{\text{Abbe}}$ or $d_{\text{Rayleigh}}$. Typically, the optimized lateral resolution of a diffraction-limited optical imaging system is around 200 nm to 300 nm when visible light is applied to view the specimen.
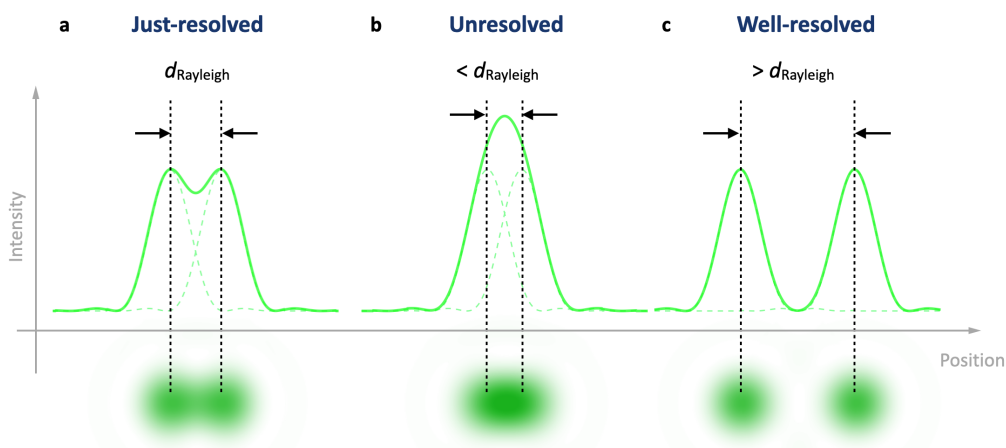


**Figure 2.6:** Illustration of Rayleigh criterion. The PSF of a point source is approximated by an Airy pattern and indicated by the dashed green line and the green disk-like pattern at the bottom. The solid green lines indicate the superposition of two Airy patterns. (a) Two point sources spaced by the distance where the first minimum of one Airy pattern is underneath the maximum of the other Airy pattern are considered just-resolved. Such distance is also known as the Rayleigh criterion. (b) Two point sources are considered unresolved when the distance between them is smaller than $d_{\text{Rayleigh}}$ (c) Two point sources are considered well-resolved when the distance between them is larger than $d_{\text{Rayleigh}}$.

### 2.3.3 Image Formation in Fluorescence Microscopy

In fluorescence microscopy, when a fluorescently labeled specimen is illuminated, the fluorescence emanating from each fluorophore will be collected by a microscope objective and then forms an image on a detector. To model the final image transferred by the optical system, the whole imaging process is assumed to be linear and shift-invariant. In other words, the fluorescence response from every point within the sample can be linearly integrated and the PSF of the imaging system is position-independent in the field of view [99]. Thus, the acquired image of fluorophore distribution is given by

$$M(\mathbf{r}) = \int I_{em}(\mathbf{r}')h(\mathbf{r} - \mathbf{r}')d\mathbf{r}', \tag{2.24}$$

where $I_{em}(\mathbf{r})$ emission distribution of the fluorophores and $h(\mathbf{r})$ denotes the PSF of the optical microscope. Eventually, this imaging process can be implemented by the two-dimensional convolution of $I_{em}(\mathbf{r})$ and $h(\mathbf{r})$

$$M(\mathbf{r}) = I_{em}(\mathbf{r}) \otimes h(\mathbf{r}), \tag{2.25}$$

where $\otimes$ denotes the convolution operation. Since the PSF does not perfectly reflect a point object, the convolution process with the PSF will smear the details of the sample emission and give rise to a blurry image of the fluorophores (Fig. 2.7(a)). This imaging process can also be formulated in Fourier space. Considering the convolution theorem, Eq. 2.25 can be converted to

$$\bar{M}(\mathbf{k}) = \bar{I}_{em}(\mathbf{k}) \cdot \bar{h}(\mathbf{k}), \tag{2.26}$$

where the bar $^-$ denotes the Fourier transform of the corresponding real-space quantity and $\mathbf{k}$ is the coordinate vector in Fourier space. $\bar{h}(\mathbf{k})$ denotes the Fourier transform of the PSF and is termed optical transfer function (OTF). As its name suggests, the OTF describes a range of spatial frequencies that can be transferred by the optical imaging system. In Fourier space, the OTF is a circular region whose bandwidth defines the cut-off frequency (the radius of the yellow dashed circle in Fig. 2.7(b))

$$k_{cutoff} = \frac{2\text{NA}}{\lambda_{em}}, \tag{2.27}$$

which translates the classic resolution limit into the maximal resolvable spatial frequency. Note that $k_{cutoff}$ is expressed as the reciprocal of Abbe diffraction limit when the emission wavelength of the sample $\lambda_{em}$ is considered [101]. As a result, the Fourier spectrum of the sample emission $\bar{I}_{em}$ will be truncated after multiplying by the OTF ($\bar{M}(\mathbf{k})$ in Fig. 2.7(b)). High spatial frequency information sitting outside of the supporting region of the OTF is lost, which renders the whole image formation a low-pass filtering process of the sample emission. Eventually, this yields a blurry image ($M(\mathbf{r})$ in Fig. 2.7(a)) and illustrates again the limited resolution that a diffraction-limited optical system obtains.
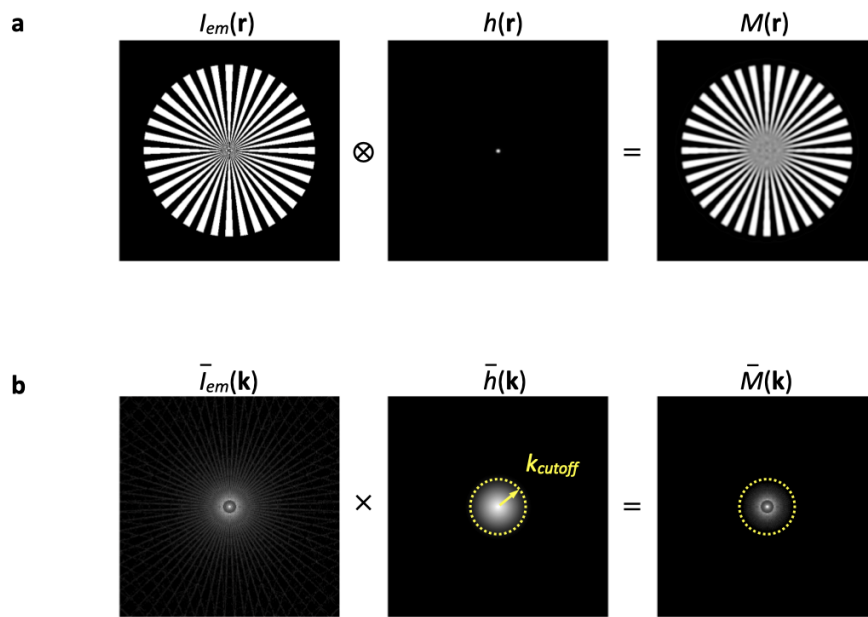


**Figure 2.7:** Visual interpretation of the image formation in fluorescence microscopy in the (a) real space and (b) Fourier space. The synthetic sample is a Siemens star. The yellow dashed circle and the relevant radius denote the region of OTF and $k_{cutoff}$, respectively.

## 2.4 Principle of SIM

The motif of SIM is to structure the intensity distribution into periodic excitation patterns such that the fluorescence emission of the sample is modulated, generating the desired moiré effect. The high spatial frequency information is retained and can therefore be restored computationally in specialized image reconstruction. In this section, we briefly introduce the principle of super-resolution SIM (hereinafter referred to as SIM).

We continue with Eq. 2.25. Suppose $I_{em}(\mathbf{r})$ is linearly in response to the excitation light, we can obtain the following relation by neglecting the proportionality constants that relate to detection efficiency and quantum yield

$$I_{em}(\mathbf{r}) = s(\mathbf{r}) \cdot I_{illu}(\mathbf{r}), \tag{2.28}$$

where $s(\mathbf{r})$ denotes the distribution of fluorophores and $I_{illu}(\mathbf{r})$ is the intensity distribution of the illumination on the sample plane. Thus, the acquired image, also referred to as "subimage" in SIM, described by Eq. 2.25 can be rewritten as

$$M(\mathbf{r}) = [s(\mathbf{r}) \cdot I_{illu}(\mathbf{r})] \otimes h(\mathbf{r}). \tag{2.29}$$

Via the interference of two beams (Fig. 1.13(a)), the intensity of the illumination at the sample plane is structured into a cosinusoidal form

$$I_{illu}(\mathbf{r}) = I_0 \left[ 1 + m \cos \left( \mathbf{k}_g \cdot \mathbf{r} + \varphi \right) \right], \tag{2.30}$$

where $I_0$ is the mean intensity and $m$ is the modulation depth. $\mathbf{k}_g$ and $\varphi$ denote the wavevector and the initial phase of the structured illumination pattern, respectively. As the image processing and reconstruction of SIM are mainly operated in Fourier space, we calculate the Fourier transform of the subimage upon this structured illumination. Considering the convolution theorem, the Fourier transform of Eq. 2.29 is given by

$$\bar{M}(\mathbf{k}) = \left[ \bar{I}_{illu}(\mathbf{k}) \otimes \bar{s}(\mathbf{k}) \right] \cdot \bar{h}(\mathbf{k}). \tag{2.31}$$

In Fourier space, the structured illumination described by Eq. 2.30 becomes

$$\bar{I}_{illu}(\mathbf{k}) = I_0 \left[ \delta(\mathbf{k}) + \frac{m}{2} e^{-i\varphi} \delta(\mathbf{k} + \mathbf{k}_g) + \frac{m}{2} e^{+i\varphi} \delta(\mathbf{k} - \mathbf{k}_g) \right], \tag{2.32}$$

where $\delta(\mathbf{k})$ is the Dirac delta function in Fourier space. Eq. 2.32 indicates that the cosinusoidal excitation pattern corresponds three sampling peaks in Fourier space ($\bar{I}_{illu}(\mathbf{k})$ in Fig. 2.8(b)). By substituting Eq. 2.32 into Eq. 2.31, we can obtain

$$\bar{M}(\mathbf{k}) = I_0 \left\{ \left[ \delta(\mathbf{k}) + \frac{m}{2} e^{-i\varphi} \delta(\mathbf{k} + \mathbf{k}_g) + \frac{m}{2} e^{+i\varphi} \delta(\mathbf{k} - \mathbf{k}_g) \right] \otimes \bar{s}(\mathbf{k}) \right\} \cdot \bar{h}(\mathbf{k})$$

$$= I_0 \left[ \bar{s}(\mathbf{k})\bar{h}(\mathbf{k}) + \frac{m}{2} e^{-i\varphi} \bar{s}(\mathbf{k} + \mathbf{k}_g)\bar{h}(\mathbf{k}) + \frac{m}{2} e^{+i\varphi} \bar{s}(\mathbf{k} - \mathbf{k}_g)\bar{h}(\mathbf{k}) \right]. \qquad (2.33)$$

In Eq. 2.33, the convolution of the Fourier spectrum $\bar{s}(\mathbf{k})$ and the three delta functions indicates that $\bar{s}(\mathbf{k})$ is duplicated three times and positioned at where those delta functions are located in Fourier space. In this fashion, the originally inaccessible high spatial frequency information is shifted into the supporting region of OTF and thus can be captured by a diffraction-limited optical imaging system. For simplicity, we can rewrite Eq. 2.33 as

$$\bar{M}(\mathbf{k}) = \sum_{l=-1}^{+1} \bar{\Omega}_l \left( \mathbf{k} - l\mathbf{k}_g \right) e^{il\varphi}, \qquad (2.34)$$

where the individual components $\bar{\Omega}_l \left( \mathbf{k} - l\mathbf{k}_g \right)$ are given by

$$\bar{\Omega}_0(\mathbf{k}) = I_0 \bar{s}(\mathbf{k})\bar{h}(\mathbf{k}), \qquad (2.35a)$$

$$\bar{\Omega}_{\pm 1}(\mathbf{k} \mp \mathbf{k}_C) = \frac{m}{2} I_0 \ \bar{s}(\mathbf{k} \mp \mathbf{k}_g)\bar{h}(\mathbf{k}). \qquad (2.35b)$$

In particular, $\bar{\Omega}_{\pm 1} \left( \mathbf{k} \mp \mathbf{k}_g \right)$ denotes the components that possess high spatial frequency information on the sample distribution. To separate the three components of $\bar{\Omega}_l \left( \mathbf{k} - l\mathbf{k}_g \right)$, at least three subimages $M(\mathbf{r})$, which can be obtained by shifting the excitation pattern $I_{em}(\mathbf{r})$ for three individual pattern phases $\varphi$, are required for the SIM image reconstruction. Specifically, $\bar{M}(\mathbf{k})$ dictates a linear equation composed of three unknown components $\bar{\Omega}_l \left( \mathbf{k} - l\mathbf{k}_g \right)$. Thus, those unknown components can be extracted by solving a system of three linear equations, which can be expressed in the matrix form as follow

$$\begin{bmatrix} \bar{M}_1(\mathbf{k}) \\ \bar{M}_2(\mathbf{k}) \\ \bar{M}_3(\mathbf{k}) \end{bmatrix} = \begin{bmatrix} e^{-i\varphi_1} & 1 & e^{+i\varphi_1} \\ e^{-i\varphi_2} & 1 & e^{+i\varphi_2} \\ e^{-i\varphi_3} & 1 & e^{+i\varphi_3} \end{bmatrix} \begin{bmatrix} \bar{\Omega}_{-1}(\mathbf{k} + \mathbf{k}_g) \\ \bar{\Omega}_0(\mathbf{k}) \\ \bar{\Omega}_{+1}(\mathbf{k} - \mathbf{k}_g) \end{bmatrix}. \qquad (2.36)$$

For simplicity, Eq. 2.36 can be simplified as

$$\bar{\mathbf{M}} = \mathbf{\Lambda}\bar{\mathbf{\Omega}}, \tag{2.37}$$

where $\mathbf{\Lambda}$ is termed the component mixing matrix. The component separation is performed by multiplying Eq. 2.37 the inverse matrix $\mathbf{\Lambda}^{-1}$:

$$\bar{\mathbf{\Omega}} = \mathbf{\Lambda}^{-1}\bar{\mathbf{M}}. \tag{2.38}$$

To achieve isotropic resolution improvement (i.e. extending the effective OTF evenly in Fourier space), the illumination patterns with different in-plane orientations $\mathbf{k}_{g,\phi}$, which is indicated by the additional index $\phi$, are applied during the image acquisition. In general, a total of nine subimages (three patterns orientations and three pattern phases for each orientation) are used to generate one SIM image with isotropic resolution improvement. Next, the separated components are shifted back to their correct position in the Fourier spectrum

$$\bar{\Omega}_{l,\phi}(\mathbf{k} - l\mathbf{k}_{g,\phi}) \to \bar{\Omega}_{l,\phi}(\mathbf{k}), \tag{2.39}$$

and recombine those separated components with the Wiener filter

$$\bar{M}_{rec}(\mathbf{k}) = \frac{\sum_{l,\phi} \bar{h}^* \left(\mathbf{k} + l\mathbf{k}_{g,\phi}\right) \bar{\Omega}_{l,\phi}(\mathbf{k})}{\sum_{l,\phi} \left|\bar{h} \left(\mathbf{k} + l\mathbf{k}_{g,\phi}\right)\right|^2 + w}. \tag{2.40}$$

Eventually, the SIM reconstructed image is obtained by performing the inverse Fourier transform of Eq. 2.40

$$M_{rec}(\mathbf{k}) = \mathcal{F}^{-1}\left\{\frac{\sum_{l,\phi} \bar{h}^* \left(\mathbf{k} + l\mathbf{k}_{g,\phi}\right) \bar{\Omega}_l(\mathbf{k})}{\sum_{l,\phi} \left|\bar{h} \left(\mathbf{k} + l\mathbf{k}_{g,\phi}\right)\right|^2 + w}\right\}, \tag{2.41}$$

where $\mathcal{F}^{-1}$ denotes the operation of the inverse Fourier transform. A detailed visual illustration of the image formation and reconstruction in conventional SIM is displayed in Fig. 2.8.
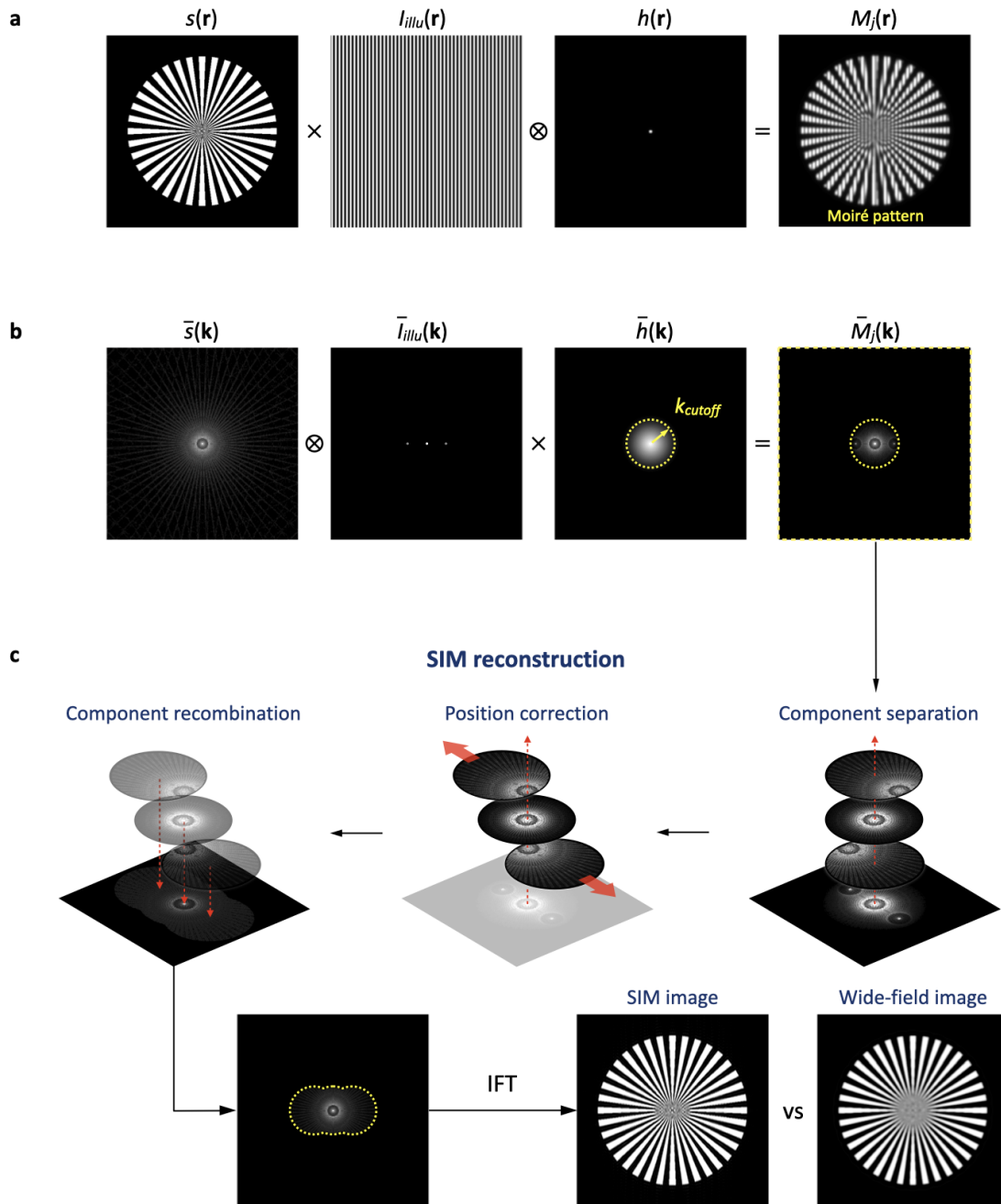
**Figure 2.8:** Illustration of SIM principle. SIM subimage formation in the (a) real space and (b) the corresponding representation in Fourier space. (c) SIM image reconstruction. Since the structured illumination patterns used here only have one orientation, the OTF extends along $k_x$ and the resolution improvement is observed only in the $x$-direction in the SIM image. For isotropic resolution improvement, illumination patterns with different orientations have to be applied. The intensity of all Fourier spectra is enhanced for clarity.

# Chapter 3

# Principle of Chiral SIM

The principle of chiral SIM is similar to that of classical SIM, namely structuring the illumination patterns in order to generate the desired moiré effect and down-modulate the high spatial frequency information. As an imaging method for chiral analysis, chiral SIM has to manage the signal that reflects the molecular chirality. Therefore, the motif of chiral SIM is to tailor the excitation fields such that the emitted CD-dependent fluorescence is modulated to generate the moiré effect on the chiral domains. In particular, it is the OC of the excitation fields to be tailored into structured patterns because, according to Eq. 2.13, the CD-related absorption can only be externally modified by the OC of the optical fields. Meantime, since the CD-related signal is generally combined with the one that originates from electric dipole absorption, extracting one type of signal from the other becomes an important issue in chiral SIM, as the illumination fields have to fulfill the requirements for this signal decoupling process.

This chapter aims to establish the theoretical framework of chiral SIM. We detail the image formation process and specifically discuss the requirements for the illumination schemes. Two scenarios for the essential signal decoupling are mathematically formulated. At last, we illustrate the corresponding image reconstruction process in chiral SIM.

## 3.1 Image Formation

### 3.1.1 CD-Dependent Fluorescence Emission from Chiral Domains

Because chiral SIM is a chiral imaging technique based on fluorescence detection, one major prerequisite is that the fluorescence emitted from chiral samples should be CD-dependent, i.e. the detected signal has to be FDCD. To achieve this, the criteria of FDCD mentioned in Sec. 1.3.2 should be fulfilled. The fluorophores should either be chiral or attached to the chiral domains, and the rotatory Brownian motion should randomize the orientation during the excited state lifetime of the fluorophores. As all

these criteria are satisfied, the CD-dependent fluorescence that is proportional to the molecular absorption rate is

$$F(\mathbf{r}) = \gamma\, a(\mathbf{r})$$

$$= \frac{2\gamma}{\varepsilon_0} \left[ \omega U_e(\mathbf{r})\alpha''(\mathbf{r}) - C(\mathbf{r})G''(\mathbf{r}) \right], \tag{3.1}$$

where $\gamma$ is a proportionality constant that describes the linear dependence of $a(\mathbf{r})$ on $F(\mathbf{r})$. Considering the point spread function of the imaging system $h(\mathbf{r})$, the acquired subimage is thus given by

$$M(\mathbf{r}) = \frac{2\gamma}{\varepsilon_0} \left[ \omega U_e(\mathbf{r})\alpha''(\mathbf{r}) - C(\mathbf{r})G''(\mathbf{r}) \right] \otimes h(\mathbf{r}). \tag{3.2}$$

Essentially, Eq. 3.2 illustrates that the recorded subimages are composed of two types of signals: one is attributed to the linear electric dipole absorption (the first term in Eq. 3.2) and the other is contributed by the CD response that depends on the chirality of light and the sample (the second term in Eq. 3.2). To obtain the CD response of the sample in the reconstructed image, it is crucial to decouple the CD-dependent signal from the signal of electric dipole absorption. Once the molecular properties are given, the feasibility of this signal decoupling only lies in the external excitation. Thus, the excitation optical fields, namely the spatial distribution of OC and electric energy density, should be neatly engineered to enable the decoupling of these two types of signals. Overall, this signal decoupling can be achieved by Fourier analysis or image subtraction, which will be discussed in the following section.

### 3.1.2 Illumination and Requirements

Considering far-field illumination schemes, the spatial distribution of OC and electric energy density generated via multiple wave interference can be, in principle, represented by the superposition of a finite number of simple harmonics that contain the fundamental spatial frequency $\mathbf{k}_C$ and $\mathbf{k}_U$, respectively. Therefore, we can express $C(\mathbf{r})$ and $U_e(\mathbf{r})$ as

$$C(\mathbf{r}) = \sum_l C_l e^{i(l\mathbf{k}_C \cdot \mathbf{r} + \phi_l)}, \tag{3.3}$$

$$U_{e,}(\mathbf{r}) = \sum_l U_{e,l} e^{i(l\mathbf{k}_U \cdot \mathbf{r} + \varphi_l)}, \tag{3.4}$$

where $C_l$ and $U_{e,l}$ are the strengths and $\phi_l$ and $\varphi_l$ the phase of the $l^{\text{th}}$ harmonic term of $C(\mathbf{r})$ and $U_e(\mathbf{r})$, respectively. In addition, the harmonics are numbered from $l = -L$ to $l = L$, in total $2L + 1$ terms. Next, we assume that the fundamental frequency of $C(\mathbf{r})$ and $U_e(\mathbf{r})$ are identical and the phases of individual frequencies are the same, i.e. $\mathbf{k}_C = \mathbf{k}_U = \mathbf{k}'$ and $\phi_l = \varphi_l$. Furthermore, the excitation patterns are supposed to remain rigid when sweeping the sample such that the phases of individual harmonics are multiples of the phase of the fundamental frequency [102]. This implies that $\varphi_l = l\varphi$, where $\varphi$ denotes the phase of the fundamental frequency. In general, the aforementioned assumptions should be valid when far-field illumination schemes are exploited. Thus, Eqs. 3.3 and 3.4 can be rewritten as

$$C(\mathbf{r}) = \sum_l C_l e^{i(l\mathbf{k}'\cdot\mathbf{r}+l\varphi)}, \tag{3.5}$$

$$U_e(\mathbf{r}) = \sum_l U_{e,l} e^{i(l\mathbf{k}'\cdot\mathbf{r}+l\varphi)}. \tag{3.6}$$

By substituting Eqs. 3.5 and 3.6 into Eq. 3.2, the acquired subimage is given by

$$M(\mathbf{r}) = \sum_l \frac{2\gamma}{\varepsilon_0} e^{i(l\mathbf{k}'\cdot\mathbf{r}+l\varphi)} \left[\omega U_{e,l}\alpha''(\mathbf{r}) - C_l G''(\mathbf{r})\right] \otimes h(\mathbf{r}). \tag{3.7}$$

To down-modulate the high spatial frequency information that corresponds to the fine details of the chiral domains, the illumination scheme should be able to structure the OC distribution into a periodic pattern. This implies, $L$ should be equal to or larger than one ($L \geq 1$) and the corresponding $C_l$ is nonzero ($C_l \neq 0$ when $l \geq 1$) such that high-order harmonic terms, which carry high spatial frequency information on chiral domains, will exist and can be restored during chiral SIM image reconstruction.

In addition to the structured OC distribution, the devised illumination scheme should also guarantee that the CD-related signal can be decoupled from the signal contributed by the dominant electric dipole absorption. This means two quantities of the excitation fields, namely $U_e(\mathbf{r})$ and $C(\mathbf{r})$ shown in Eq. 3.2, require special considerations. In the following, we illustrate two scenarios of the illumination schemes that allow decoupling the CD-related signal from that of electric dipole absorption.

**Scenario 1: The Number of the Harmonics of $C(\mathbf{r})$ Exceeds that of $U_e(\mathbf{r})$**

Continue with Eq. 3.7, we first calculate the corresponding Fourier transform by considering the convolution theorem:

$$\bar{M}(\mathbf{k}) = \sum_l \frac{2\gamma}{\varepsilon_0} \, e^{il\varphi} \left[ \omega U_{e,l} \bar{\alpha}''(\mathbf{k} - l\mathbf{k}') - C_l \bar{G}''(\mathbf{k} - l\mathbf{k}') \right] \bar{h}(\mathbf{k})$$

$$= \sum_l \bar{\Omega}_l(\mathbf{k} - l\mathbf{k}') e^{il\varphi}, \tag{3.8}$$

where the individual components $\bar{\Omega}_l(\mathbf{k} - l\mathbf{k}')$ that consist of different spatial frequency information are given by

$$\bar{\Omega}_l(\mathbf{k} - l\mathbf{k}') = \frac{2\gamma}{\varepsilon_0} \left[ \omega U_{e,l} \bar{\alpha}''(\mathbf{k} - l\mathbf{k}') - C_l \bar{G}''(\mathbf{k} - l\mathbf{k}') \right] \bar{h}(\mathbf{k}). \tag{3.9}$$

As Eq. 3.8 implies, multiple $\bar{\Omega}_l(\mathbf{k} - l\mathbf{k}')$ are superimposed within a single subimage. Those individual components can be separated after the regular separation process depicted in Sec. 3.2. However, the separated $\bar{\Omega}_l(\mathbf{k} - l\mathbf{k}')$ still contain the signal that originates from the electric dipole absorption, as shown in the first term of Eq. 3.9. Here, if the illumination scheme can form the excitation fields where, for specific harmonic terms, only the harmonic strengths of the OC distribution $C_l$ exist, the corresponding individual components will solely contain the CD-related signal. To be more explicitly, there should be a set of harmonic terms indexed by $l'$ whose harmonic strengths $U_{e,l'} = 0$ but $C_{l'} \neq 0$. In this way, the $l'^{\text{th}}$ individual components $\bar{\Omega}_{l'}(\mathbf{k} - l'\mathbf{k}')$ only consist of the CD-related signal, as shown in the following

$$\bar{\Omega}_{l'}(\mathbf{k} - l'\mathbf{k}') = -\frac{2\gamma}{\varepsilon_0} C_l' \bar{G}''(\mathbf{k} - l'\mathbf{k}') \bar{h}(\mathbf{k}). \tag{3.10}$$

In addition, the absolute value of $l'$ needs to be equal or larger than one ($1 \leq |l'| \leq L$) such that high-order terms of $\bar{\Omega}_{l'}(\mathbf{k} - l'\mathbf{k}')$, which consist of high spatial frequency information on chiral domains, will subsist and be recovered in the ensuing reconstruction process. Regarding the undecoupled components, i.e. $\bar{\Omega}_l(\mathbf{k} - l\mathbf{k}')$ where $U_{e,l} \neq 0$, they will be excluded from the subsequent position correction and recombination processes. In theory, several illumination schemes using the interference of LPL are able to generate this type of excitation pattern that follows the aforementioned requirements [103, 104] and thus enable the decoupling of the CD-dependent signal through Fourier analysis.

**Scenario 2: $U_e(\mathbf{r})$ Remains Identical While the Handedness of $C(\mathbf{r})$ Alters**

If the harmonic strengths $U_{e,l}$ exist in every harmonic term, the signal contributed by electric dipole absorption may be excluded using image subtraction. To enable such a type of signal decoupling, the selected illumination scheme should form the excitation patterns whose $U_e(\mathbf{r})$ remains the same while the handedness of $C(\mathbf{r})$ changes. Under this circumstance, we can acquire pairs of conjugate subimages $M_\pm(\mathbf{r})$ as shown in the following

$$M_\pm(\mathbf{r}) = \sum_l \frac{2\gamma}{\varepsilon_0} e^{i(l\mathbf{k}'\cdot\mathbf{r}+l\varphi)} \left[\omega U_{e,l}\alpha''(\mathbf{r}) - C_{\pm,l}G''(\mathbf{r})\right] \otimes h(\mathbf{r}), \qquad (3.11)$$

where the sign $\pm$ denotes the change of the handedness of $C(\mathbf{r})$. Next, we can produce the differential image $M(\mathbf{r})$, which is later for the same image reconstruction, by subtracting one conjugate image from the other

$$M(\mathbf{r}) = M_+(\mathbf{r}) - M_-(\mathbf{r})$$

$$= -\sum_l \frac{2\gamma}{\varepsilon_0} e^{i(l\mathbf{k}'\cdot\mathbf{r}+l\varphi)} \Delta C_l G''(\mathbf{r}) \otimes h(\mathbf{r}), \qquad (3.12)$$

where $\Delta C_l = C_{+,l} - C_{-,l}$ denotes the differential harmonic strengths. The corresponding Fourier transform of Eq. 3.12 is thus calculated as

$$\bar{M}(\mathbf{k}) = -\sum_l \frac{2\gamma}{\varepsilon_0} e^{il\varphi} \Delta C_l \bar{G}''(\mathbf{k} - l\mathbf{k}')\bar{h}(\mathbf{k})$$

$$= \sum_{l=-L}^{L} \bar{\Omega}_l(\mathbf{k} - l\mathbf{k}')e^{il\varphi}, \qquad (3.13)$$

where the individual components $\bar{\Omega}_l(\mathbf{k} - l\mathbf{k}')$ are given by

$$\bar{\Omega}_l(\mathbf{k} - l\mathbf{k}') = -\frac{2\gamma}{\varepsilon_0} \Delta C_l \bar{G}''(\mathbf{k} - l\mathbf{k}')\bar{h}(\mathbf{k}). \qquad (3.14)$$

Here, the individual components only carry the CD-related signal since the signal that originates from electric dipole absorption is eliminated after the image subtraction. As long as $\Delta C_l \neq 0$, $\bar{\Omega}(\mathbf{k} - l\mathbf{k}')$ will subsist and high spatial frequency information on chiral domains will be restored in the image reconstruction. In theory, one possible illumination scheme to generate the excitation patterns that fulfill the aforementioned requirements is to use two CPL [103, 105].

## 3.2 Image Reconstruction

We continue with Eqs. 3.8 or 3.13 and follow the similar component separation process illustrated in Sec. 2.4. Because there are in total $2L+1$ individual components, a series of at least $2L+1$ subimages $M_j(\mathbf{r})$ with different pattern phase $\varphi_j$ is necessary to separate the superimposed components. Those subimages $\bar{M}_j(\mathbf{k})$, indexed by $j = 1, 2, ..., 2L+1$, can establish a system of linear equations as shown in the following

$$
\begin{bmatrix} \bar{M}_1(\mathbf{k}) \\ \\ \vdots \\ \\ \bar{M}_{2L+1}(\mathbf{k}) \end{bmatrix} = \begin{bmatrix} e^{-iL\varphi_1} & \cdots & 1 & \cdots & e^{iL\varphi_1} \\ \\ \vdots & & \ddots & & \vdots \\ \\ e^{-iL\varphi_{2L+1}} & \cdots & 1 & \cdots & e^{iL\varphi_{2L+1}} \end{bmatrix} \begin{bmatrix} \bar{\Omega}_{-L}(\mathbf{k} + L\mathbf{k}') \\ \vdots \\ \bar{\Omega}_0(\mathbf{k}) \\ \vdots \\ \bar{\Omega}_L(\mathbf{k} - L\mathbf{k}') \end{bmatrix}. \quad (3.15)
$$

For simplicity, Eq. 4.20 can be rewritten by

$$
\bar{\mathbf{M}} = \mathbf{\Lambda}\bar{\mathbf{\Omega}}, \quad (3.16)
$$

where $\bar{\mathbf{M}}$ and $\bar{\mathbf{\Omega}}$ are the column vectors which consist of the subimages and separated components, respectively, and $\mathbf{\Lambda}$ denotes the component mixing matrix and its elements can be defined by

$$
\mathbf{\Lambda}_{jl} = e^{il\varphi_j}. \quad (3.17)
$$

Finally, the separation of the individual components is conducted by inverting Eq. 3.16

$$
\bar{\mathbf{\Omega}} = \mathbf{\Lambda}^{-1}\bar{\mathbf{M}}. \quad (3.18)
$$

### 3.2.1 Position Correction of the Separated Components

To gain the isotropic resolution improvement in chiral SIM, the structured illumination with different lateral orientations $\mathbf{k}'_\phi$, where $\phi$ denotes the angle of the pattern orientation, is applied during the image acquisition. In this way, the separated components $\bar{\Omega}_{l,\phi}(\mathbf{k}-l\mathbf{k}')$ located at $\mathbf{k} = l\mathbf{k}'_\phi$ in Fourier space are obtained after the separation process. Subsequently, $\bar{\Omega}_{l,\phi}(\mathbf{k} - l\mathbf{k}')$ should be shifted back to their true position in the Fourier spectrum. Note

that this position correction process, as well as the subsequent recombination process, are executed differently according to the scenario that the applied excitation fields follow.

When scenario 1 is followed, only the individual components whose harmonic strengths $U_{e,l} = 0$, namely $\bar{\Omega}_{l'}(\mathbf{k} - l'\mathbf{k})$, are computationally shifted back to their true position in Fourier space in the first scenario. In this sense, the position correction of the individual components are denoted by

$$\bar{\Omega}_{l',\phi}(\mathbf{k} - l'\mathbf{k}'_\phi) \rightarrow \bar{\Omega}_{l',\phi}(\mathbf{k}). \tag{3.19}$$

As for scenario 2, all individual components are shifted back to their original positions in Fourier space, which is denoted by

$$\bar{\Omega}_{l,\phi}(\mathbf{k} - l\mathbf{k}'_\phi) \rightarrow \bar{\Omega}_{l,\phi}(\mathbf{k}). \tag{3.20}$$

### 3.2.2 Recombination of the Separated Components

Finally, the separated components are recombined with the Wiener filter as shown in the following when the excitation fields obey the first scenario

$$\bar{M}_{rec}(\mathbf{k}) = -\frac{\sum_{l',\phi} \bar{h}^* \left(\mathbf{k} + l'\mathbf{k}'_\phi\right) \bar{\Omega}_{l',\phi}(\mathbf{k})}{\sum_{l',\phi} \left|\bar{h}\left(\mathbf{k} + l'\mathbf{k}'_\phi\right)\right|^2 + w}, \tag{3.21}$$

and the second scenario

$$\bar{M}_{rec}(\mathbf{k}) = -\frac{\sum_{l,\phi} \bar{h}^* \left(\mathbf{k} + l\mathbf{k}'_\phi\right) \bar{\Omega}_{l,\phi}(\mathbf{k})}{\sum_{l,\phi} \left|\bar{h}\left(\mathbf{k} + l\mathbf{k}'_\phi\right)\right|^2 + w}. \tag{3.22}$$

Here, $w$ denotes the empirical Wiener parameter. Note that components with $U_{e,l} \neq 0$ are discarded after the component separation in the first scenario. Therefore, only $\bar{\Omega}_{l'}(\mathbf{k})$ are recombined to form the reconstructed Fourier image shown in Eq. 3.21. After retransforming the chiral SIM Fourier image to real space by inverse Fourier transformation, as denoted by

$$M_{rec}(\mathbf{r}) = \mathcal{F}^{-1}\left[\bar{M}_{rec}(\mathbf{k})\right], \tag{3.23}$$

we can obtain the super-resolved images of chiral domains.

# Chapter 4

# Theoretical Demonstration of Chiral SIM

This chapter aims to provide proof-of-concept demonstration of chiral SIM. To begin with, we investigate the excitation fields, namely the spatial distribution of OC and electric energy density, formed by the interference of two far-field waves. Two possible illumination schemes that exploit the interference of (i) *s*- and *p*-polarized light and (ii) two CPL with the same handedness are studied and the analytical expressions of the OC and electric energy density patterns generated by these two illumination schemes are verified by numerical simulations. The image formation process is numerically simulated to mimic a real experiment and then the synthesized subimages are processed by the chiral SIM reconstruction program to generate the super-resolved chiral domain images. Finally, we present two theoretical demonstrations of chiral SIM in the absence of noise and discuss our discovery.

## 4.1 Analysis of Two-Wave-Interference Illumination Scheme

In theory, a single electromagnetic plane wave with an arbitrary polarization state can be decomposed into *s*- and *p*-polarized components. Considering multiple plane waves propagating towards the *xy*-plane, which is appointed as the sample plane, at different angles, the corresponding *s*- and *p*-polarized components of the electric and magnetic fields can be written by [103]

$$\tilde{\mathbf{E}}_{m,s} = E_{m,s}e^{i(\mathbf{k}_m\cdot\mathbf{r}-\omega t+\xi_m)}e^{i\zeta_m}\left(-\sin\phi_m\hat{\mathbf{x}} + \cos\phi_m\hat{\mathbf{y}}\right), \tag{4.1}$$

$$\tilde{\mathbf{B}}_{m,s} = \frac{n}{c}E_{m,s}e^{i(\mathbf{k}_m\cdot\mathbf{r}-\omega t+\xi_m)}e^{i\zeta_m}\left(-\cos\theta_m\cos\phi_m\hat{\mathbf{x}} - \cos\theta_m\sin\phi_l\hat{\mathbf{y}} + \sin\theta_m\hat{\mathbf{z}}\right), \tag{4.2}$$

$$\tilde{\mathbf{E}}_{m,p} = E_{m,p}e^{i(\mathbf{k}_m \cdot \mathbf{r} - \omega t + \xi_m)}\left(-\cos\theta_m \cos\phi_m \hat{\mathbf{x}} - \cos\theta_m \sin\phi_m \hat{\mathbf{y}} + \sin\theta_m \hat{\mathbf{z}}\right), \quad (4.3)$$

$$\tilde{\mathbf{B}}_{m,p} = \frac{n}{c}E_{m,p}e^{i(\mathbf{k}_m \cdot \mathbf{r} - \omega t + \xi_m)}\left(-\sin\phi_m \hat{\mathbf{x}} + \cos\phi_m \hat{\mathbf{y}}\right), \quad (4.4)$$

where $m$ is the index that numbers the incoming plane waves, $n$ denotes the refractive index, and $c$ is the speed of light. $E_{m,s}$ and $E_{m,p}$ indicate the electric field amplitude of the $s$- and $p$-polarized components, respectively. $\zeta_m$ denotes the phase difference between the $s$- and $p$-polarized components of the plane wave and influences the polarization state of the incident wave. $\xi_m$, $\phi_m$ and $\theta_m$ denote the initial phase, azimuth and incident angles of the plane wave, respectively. $\mathbf{k}_m$ is the wavevector that indicates the propagation direction of the plane wave and is specified by

$$\mathbf{k}_m = nk_0(\sin\theta_m \cos\phi_m \hat{\mathbf{x}} + \sin\theta_m \sin\phi_m \hat{\mathbf{y}} + \cos\theta_m \hat{\mathbf{z}}). \quad (4.5)$$

For multiple-wave interference, the final electric and magnetic fields are given by

$$\tilde{\mathbf{E}} = \sum_m \left(\tilde{\mathbf{E}}_{m,s} + \tilde{\mathbf{E}}_{m,p}\right), \quad (4.6)$$

$$\tilde{\mathbf{B}} = \sum_m \left(\tilde{\mathbf{B}}_{m,s} + \tilde{\mathbf{B}}_{m,p}\right). \quad (4.7)$$

In practice, the interference of two plane waves is relatively simple to be implemented in an experiment when, for instance, a diffractive optical component is applied. Thus, they are widely used in microscopy methods for generating structured illumination [106, 107]. We thereby consider two plane waves, namely $m = 1, 2$, that coincide on the sample plane (Fig. 4.1). The resulting OC and electric energy density distribution are expressed as

$$
\begin{aligned}
C(\mathbf{r}) = \frac{\varepsilon_0 n k_0}{2}\Bigg( & 2E_{1,s}E_{1,p}\sin\zeta_1 + 2E_{2,s}E_{2,p}\sin\zeta_2 \\
& -\sin\Phi\Big\{(E_{1,s}E_{2,p}\cos\zeta_1 + E_{1,p}E_{2,s}\cos\zeta_2)[\cos(\phi_1 - \phi_2)(1 + \cos\theta_1\cos\theta_2) + \sin\theta_1\sin\theta_2] \\
& + [E_{1,s}E_{2,s}\cos(\zeta_1 - \zeta_2) + E_{1,p}E_{2,p}]\sin(\phi_1 - \phi_2)(\cos\theta_1 + \cos\theta_2)\Big\} \\
& + \cos\Phi\Big\{(E_{1,s}E_{2,p}\sin\zeta_1 + E_{1,p}E_{2,s}\sin\zeta_2)[\cos(\phi_1 - \phi_2)(1 + \cos\theta_1\cos\theta_2) + \sin\theta_1\sin\theta_2] \\
& + E_{1,s}E_{2,s}\sin(\zeta_1 - \zeta_2)\sin(\phi_1 - \phi_2)(\cos\theta_1 + \cos\theta_2)\Big\}\Bigg), \quad (4.8)
\end{aligned}
$$

$$U_e(\mathbf{r}) = \frac{\varepsilon_0}{4}\left\{ E_{1,s}^2 + E_{1,p}^2 + E_{2,s}^2 + E_{2,p}^2 \right.$$

$$+ 2E_{1,s}E_{2,s}\cos(\phi_1 - \phi_2)\cos(\Phi + \zeta_1 - \zeta_2)$$

$$+ 2E_{1,s}E_{2,p}\cos\theta_2\sin(\phi_1 - \phi_2)\cos(\Phi + \zeta_1)$$

$$- 2E_{1,p}E_{2,s}\cos\theta_1\sin(\phi_1 - \phi_2)\cos(\Phi - \zeta_2)$$

$$\left. + 2E_{1,p}E_{2,p}[\cos\theta_1\cos\theta_2\cos(\phi_1 - \phi_2) + \sin\theta_1\sin\theta_2]\cos\Phi \right\}, \qquad (4.9)$$

when we substitute Eqs. 4.6 and 4.7 into Eqs. 2.8 and 2.14 [103]. Here, $\Phi$ is a factor that depends on the wavevector and the initial phase of the two incident waves, given by

$$\Phi = (\mathbf{k}_2 - \mathbf{k}_1)\cdot\mathbf{r} + \xi_2 - \xi_1$$

$$= nk_0\left[ x\left(\sin\theta_2\cos\phi_2 - \sin\theta_1\cos\phi_1\right) \right.$$

$$\left. + y\left(\sin\theta_2\sin\phi_2 - \sin\theta_1\sin\phi_1\right) + z\left(\cos\theta_2 - \cos\theta_1\right)\right] + \xi_2 - \xi_1. \qquad (4.10)$$

If we look into Eqs 4.8 and 4.9, we can notice that the resulting $C(\mathbf{r})$ and $U_e(\mathbf{r})$ have a strong dependency on the configuration ($\phi_{1,2}$, $\theta_{1,2}$ and $\zeta_{1,2}$) of the two excitation plane waves. The first and second terms on the right-hand side of Eq. 4.8 lead to an offset, which could be positive or negative, in the designed OC distribution. Particularly, this offset disappears if two incident waves are linearly polarized ($\zeta_1 = \zeta_2 = 0$). Similarly, the first to fourth terms on the right-hand side of Eq. 4.9 describe a positive offset, which exists to ensure that the electric energy density is, in principle, positive as well.
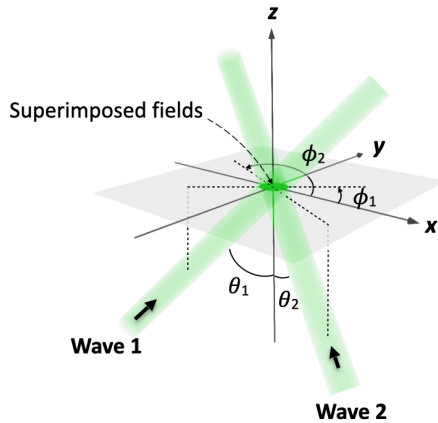


**Figure 4.1:** Schematics of the two-wave interference. $\phi_m$ and $\theta_m$ and of the azimuth and incident angle of the $m^{\text{th}}$ wave, where $m = 1, 2$.

## 4.2  Image Reconstruction Regarding
## Two-Wave-Interference Illumination Schemes

Here, we select two specific two-wave-interference illumination schemes, namely using *s*- and *p*-polarized light and two CPL with the same handedness, to generate the structured OC and electric density patterns for the ensuing theoretical analysis and numerical demonstration. The readers who would like to know more about using other far-field illumination schemes to generate structured OC distribution are referred to Ref. [103].

### 4.2.1  Illumination Scheme of Using *S*- and *P*-Polarized Waves

The schematic diagram that describes the illumination scheme of using *s*- and *p*-polarized plane waves is shown in Fig. 4.2. We assign the first plane wave to be *p*-polarized and the second one *s*-polarized. Accordingly, $\zeta_1 = \zeta_2 = 0$ and the electric field amplitudes become $E_{1,s} = E_{2,p} = 0$, $E_{1,p} = E_{2,s} = \frac{1}{\sqrt{2}}E_0$, where $\frac{1}{\sqrt{2}}$ is a constant that normalizes the amplitudes. These two waves propagate towards the sample plane ($xy$-plane) at the same incident angle $\theta$ ($\theta_1 = \theta_2 = \theta$) and their azimuth angles follow the relation of $|\phi_1 - \phi_2| = \pi$. Considering Eqs. 4.8 and 4.9, the OC and electric energy density distribution generated on the sample plane by this illumination scheme are

$$C_j(\mathbf{r}) = C_1 \cos(\mathbf{k}' \cdot \mathbf{r} + \varphi_j), \tag{4.11}$$

$$U_{e,j}(\mathbf{r}) = U_{e,0} = \frac{\varepsilon_0}{4}E_0^2, \tag{4.12}$$

where $j$ indexes the pattern shift when the excitation patterns sweep the sample. $C_1 = n\frac{\varepsilon_0 \omega}{2c}E_0^2 \cos^2\theta = n\,C_{\mathrm{CPL}}\cos^2\theta$ denotes the amplitude of the structured OC pattern and corresponds to the strength of $1^{\mathrm{st}}$ harmonic term. $U_{e,0}$ corresponds to the strength of the $0^{\mathrm{th}}$ harmonic term of the electric energy density distribution. As shown in Eq. 4.11, the OC distribution is structured into a cosinusoidal form and its orientation relates to the wavevector

$$\mathbf{k}' = nk_0 \sin\theta \big[\big(\cos\phi_1 - \cos\phi_2\big)\hat{\mathbf{x}} + \big(\sin\phi_1 - \sin\phi_2\big)\hat{\mathbf{y}}\big]$$

$$= 2nk_0 \sin\theta(\cos\phi\,\hat{\mathbf{x}} + \sin\phi\,\hat{\mathbf{y}}) \tag{4.13}$$
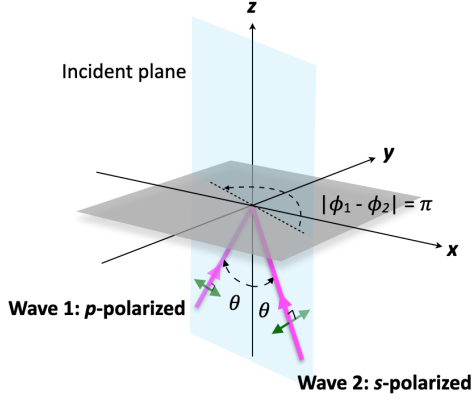
**Figure 4.2:** Schematics of using *s*- and *p*-polarized light to generate structured OC patterns. The superposition of *s*- and *p*-polarized light with an incident angle of $\theta$ forms periodically structured OC patterns and uniform electric energy density distribution on the sample plane.

with the relation of $|\phi_1 - \phi_2| = \pi$. Here, we let $\phi_1 = \phi$ and $\phi_2 = \phi \pm \pi$ in order to simplify the notation. According to Eq. 4.13, we can rotate the OC pattern, as required during the image acquisition of chiral SIM, by adjusting the azimuth angle of the two waves while keeping the relation of $|\phi_1 - \phi_2| = \pi$. The phase of the OC pattern is given by

$$\varphi_j = \frac{\pi}{2} - \xi_1 + \xi_2, \tag{4.14}$$

which suggests that we can shift the pattern by adjusting the initial phase of the *s*- and *p*-polarized waves. In contrast to the structured $C_j(\mathbf{r})$, the resulting $U_{e,j}(\mathbf{r})$ shown in Eq. 4.12 are independent of the incident angle and azimuth angle of the *s*- and *p*-polarized light and remains constant. This indicates that, in principle, the harmonic strengths $U_{e,l} = 0$ when $|l| \geq 1$ and the corresponding individual components $\bar{\Omega}_{\pm 1}(\mathbf{k} \mp \mathbf{k}')$ solely contain the CD-related signal. Therefore, this illumination scheme fulfills the requirements mentioned in the first scenario illustrated in Sec. 3.1.2 and enables the decoupling of the CD-related signal. In the following, we formulate this decoupling process.

Considering Eqs. 3.7, 4.11 and 4.12, the subimages $M_j(\mathbf{r})$ obtained with the illumination scheme of the *s*- and *p*-polarized waves are

$$M_j(\mathbf{r}) = \frac{2\gamma}{\varepsilon_0}\Big[\omega U_{e,0}\alpha''(\mathbf{r}) - C_1 \cos(\mathbf{k}' \cdot \mathbf{r} + \varphi_j)G''(\mathbf{r})\Big] \otimes h(\mathbf{r}). \tag{4.15}$$

The corresponding Fourier transform of the subimages $\bar{M}_j(\mathbf{r})$ is therefore calculated as

$$\bar{M}_j(\mathbf{k}) = \frac{2\gamma}{\varepsilon_0}\Big[\omega U_{e,0}\bar{\alpha}''(\mathbf{k}) - e^{-i\varphi_j}C_1\bar{G}''(\mathbf{k}+\mathbf{k}') - e^{i\varphi_j}C_1\bar{G}''(\mathbf{k}-\mathbf{k}')\Big]\bar{h}(\mathbf{k})$$

$$= \sum_{l=-1}^{1} \bar{\Omega}_l(\mathbf{k} - l\mathbf{k}')e^{il\varphi_j}, \tag{4.16}$$

where the three individual components $\bar{\Omega}_l(\mathbf{k} - l\mathbf{k}')$ are given by

$$\bar{\Omega}_0(\mathbf{k}) = \frac{2\gamma}{\varepsilon_0}\omega U_{e,0}\bar{\alpha}''(\mathbf{k})\bar{h}(\mathbf{k}), \tag{4.17}$$

$$\bar{\Omega}_{\pm 1}(\mathbf{k} \mp \mathbf{k}') = -\frac{2\gamma}{\varepsilon_0}C_1\bar{G}''(\mathbf{k} \mp \mathbf{k}')\bar{h}(\mathbf{k}). \tag{4.18}$$

As can be seen in Eqs. 4.17 and 4.18, $\bar{\Omega}_l(\mathbf{k} - l\mathbf{k}')$ solely contain the CD-related signal when $l = \pm 1$. Still, at least $2L + 1 = 3$ subimages are required to separate all $\bar{\Omega}_l(\mathbf{k} - l\mathbf{k}')$. To achieve this, the excitation pattern has to be shifted thrice during the image acquisition, which corresponds to three different pattern phases. In practice, a preferable choice for the pattern phases $\varphi_j$ is a set of equidistant values between 0 and $2\pi$, which means

$$\varphi_j = (j - 1)\varphi_0, \tag{4.19}$$

where $\varphi_0 = \frac{2\pi}{2L+1}$ denotes the fundamental step of the pattern phase. To separate the individual components, a system of linear equations is established as

$$\begin{bmatrix} \bar{M}_1(\mathbf{k}) \\ \bar{M}_2(\mathbf{k}) \\ \bar{M}_3(\mathbf{k}) \end{bmatrix} = \begin{bmatrix} 1 & 1 & 1 \\ e^{-i\varphi_0} & 1 & e^{i\varphi_0} \\ e^{-i2\varphi_0} & 1 & e^{i2\varphi_0} \end{bmatrix} \begin{bmatrix} \bar{\Omega}_{-1}(\mathbf{k} + \mathbf{k}') \\ \bar{\Omega}_0(\mathbf{k}) \\ \bar{\Omega}_{+1}(\mathbf{k} - \mathbf{k}') \end{bmatrix}, \tag{4.20}$$

when $j$ varies from 1 to $2L + 1 = 3$. Eq. 4.20 can also be written in a simpler expression:

$$\bar{\mathbf{M}} = \boldsymbol{\Lambda}\bar{\boldsymbol{\Omega}}, \tag{4.21}$$

where $\bar{\mathbf{M}}$ and $\bar{\boldsymbol{\Omega}}$ denote the column vector composed by the subimages and the separated components, respectively, and $\boldsymbol{\Lambda}$ is the corresponding component mixing matrix. Then the component separation is achieved by inverting Eq. 4.21

$$\bar{\boldsymbol{\Omega}} = \boldsymbol{\Lambda}^{-1}\bar{\mathbf{M}}. \tag{4.22}$$

After the separation process, $\bar{\Omega}_0(\mathbf{k})$ is discarded because it contains the unwanted signal of electric dipole absorption. Only $\bar{\Omega}_{\pm 1}(\mathbf{k} \mp \mathbf{k}')$ are involved in the subsequent position correction and recombination processes. To obtain isotropic resolution improvement in Fourier space, we change the in-plane orientation of the pattern three times during the

image acquisition. Here, the wavevector of the pattern becomes $\mathbf{k}'_\phi$ and $\phi$ marks the pattern orientation (Eq. 4.13). Practically, a preferred set of $\phi$ is

$$\phi = \{0, \frac{\pi}{3}, \frac{2\pi}{3}\} \tag{4.23}$$

such that the separated components $\bar{\Omega}_{\pm1,\phi}(\mathbf{k} \mp \mathbf{k}')$ can be distributed evenly after they are shifted back to their true position in Fourier space:

$$\bar{\Omega}_{\pm1,\phi}(\mathbf{k} \mp \mathbf{k}'_\phi) \to \bar{\Omega}_{\pm1,\phi}(\mathbf{k}). \tag{4.24}$$

In general, nine subimages (three pattern orientations and three pattern phases for each orientation) are acquired to reconstruct an image with isotropic resolution improvement. Via the recombination of the position-corrected components, the reconstructed chiral SIM image in Fourier space is given by

$$\bar{M}_{rec}(\mathbf{k}) = -\frac{\sum_{l'=\pm1,\phi} \bar{h}^* \left(\mathbf{k} + l'\mathbf{k}'_\phi\right) \bar{\Omega}_{l'}(\mathbf{k})}{\sum_{l'=\pm1,\phi} \left|\bar{h}\left(\mathbf{k} + l'\mathbf{k}'_\phi\right)\right|^2 + w}, \tag{4.25}$$

when the Wiener filter is considered. Finally, the reconstructed chiral SIM image in real space can be retransformed by performing the inverse Fourier transform of Eq. 4.25.

**Global Phase Issue in the Image Reconstruction**

In reality, the phase of the structured excitation patterns does not perfectly match the designated phase set described in Eq. 4.19, which is already an issue in conventional SIM and now also happens to chiral SIM. Consequently, each pattern phase $\varphi_j$ will contain an unknown residual phase or the so-called global phase $\varphi'$ and becomes

$$\varphi_j \to \varphi_j + \varphi'. \tag{4.26}$$

After the component separation is completed, this residual phase globally shifts the phase of individual components $\bar{\Omega}_l(\mathbf{k} - l\mathbf{k}')$, which also illustrates why this residual phase is usually termed the global phase. Because the global phase influences the reconstruction results, it should be estimated to correct the phase of the separated components, preventing unpleasant artifacts in the reconstruction image. In conventional SIM, this global phase is evaluated by analyzing the cross-correlation between the

separated components, i.e. computing the cross-correlation between $\bar{\Omega}_0(\mathbf{k})$ and $\bar{\Omega}_{\pm 1}(\mathbf{k})$, respectively, after the position correction process [108]. Similarly, the global phase in chiral SIM is estimated by computing the cross-correlations between the separated components. However, since $\bar{\Omega}_0(\mathbf{k})$ carries the undesired signal from electric dipole absorption when the illumination scheme that uses *s*- and *p*-polarized light is applied, the cross-correlation between $\bar{\Omega}_0(\mathbf{k})$ and $\bar{\Omega}_{\pm 1}(\mathbf{k})$ is unusable. The determination of the global phase should thus be operated based on the cross-correlation between $\bar{\Omega}_{+1}(\mathbf{k})$ and $\bar{\Omega}_{-1}(\mathbf{k})$. We formulate this global phase determination in the following paragraphs.

Considering Eq. 4.26, $C_j(\mathbf{r})$ shown in Eq. 4.11 is rewritten as

$$C_j(\mathbf{r}) = C_1 \cos\left(\mathbf{k}' \cdot \mathbf{r} + \varphi_j + \varphi'\right). \tag{4.27}$$

Accordingly, the Fourier transform of the subimages can be calculated as

$$\bar{M}_j(\mathbf{k}) = \frac{2\gamma}{\varepsilon_0}\left[\omega U_{e,0}\bar{\alpha}''(\mathbf{k}) - e^{-i\varphi_j}e^{-i\varphi'}C_1\bar{G}''(\mathbf{k}+\mathbf{k}') - e^{i\varphi_j}e^{i\varphi'}C_1\bar{G}''(\mathbf{k}-\mathbf{k}')\right]\bar{h}(\mathbf{k})$$

$$= \sum_{l=-1}^{1} \bar{\Omega}_l(\mathbf{k}-l\mathbf{k}')e^{il\varphi'}e^{il\varphi_j}. \tag{4.28}$$

When we use the phase set described in Eq. 4.19 to form the component mixing matrix, the system of linear equations composed of $\bar{M}_j(\mathbf{k})$ is established as

$$\begin{bmatrix} \bar{M}_1(\mathbf{k}) \\ \bar{M}_2(\mathbf{k}) \\ \bar{M}_3(\mathbf{k}) \end{bmatrix} = \begin{bmatrix} 1 & 1 & 1 \\ e^{-i\varphi_0} & 1 & e^{i\varphi_0} \\ e^{-i2\varphi_0} & 1 & e^{i2\varphi_0} \end{bmatrix} \begin{bmatrix} e^{-i\varphi'}\bar{\Omega}_{-1}(\mathbf{k}+\mathbf{k}') \\ \bar{\Omega}_0(\mathbf{k}) \\ e^{i\varphi'}\bar{\Omega}_{+1}(\mathbf{k}-\mathbf{k}') \end{bmatrix}. \tag{4.29}$$

As evident in Eq. 4.29, the separated components $\bar{\Omega}_{\pm 1}(\mathbf{k} \mp \mathbf{k})$ are accompanied by the phase factors $e^{\pm i\varphi'}$ that originate from the global phase $\varphi'$. Thus, we have to evaluate this global phase and compensate the additional phase factor of $\bar{\Omega}_{\pm 1}(\mathbf{k} \mp \mathbf{k})$ by multiplying $e^{\mp i\varphi'}$ individually:

$$e^{\pm i\varphi'}\bar{\Omega}_{\pm 1}(\mathbf{k}) \rightarrow \bar{\Omega}_{\pm 1}(\mathbf{k}). \tag{4.30}$$

Typically, the global phase is estimated by analyzing the cross-correlation between the position-corrected components $\bar{\Omega}_l(\mathbf{k})$ at $\mathbf{k} = 0$, which is defined by [109]

$$\mathcal{C}_{i,j}(\mathbf{k} = 0) = \left( \int \bar{\Omega}_i(\mathbf{k}'') \bar{\Omega}_j^*(\mathbf{k} + \mathbf{k}'') d\mathbf{k}'' \right) \bigg|_{\mathbf{k}=0} = \left[ \bar{\Omega}_i(\mathbf{k}) \circledast \bar{\Omega}_j(\mathbf{k}) \right] \bigg|_{\mathbf{k}=0} \qquad (4.31)$$

where $\circledast$ denotes the cross-correlation operation. In principle, the global phase should be evaluated by the cross-correlations between the position-corrected $\pm 1^{\text{st}}$-order and the $0^{\text{th}}$-order components, i.e. $\mathcal{C}_{0,\pm 1}$, akin to what is performed in conventional SIM [108, 109]. However, since $\bar{\Omega}_0(\mathbf{k})$ shown in Eq. 4.17 contains undesired signal from electric dipole absorption, we calculate the cross-correlation between $\bar{\Omega}_{\pm 1}(\mathbf{k})$ to find out the global phase (see Appendix B for details):

$$\mathcal{C}_{-1,1}(\mathbf{k} = 0) = \left[ e^{-i\varphi'} \bar{\Omega}_{-1}(\mathbf{k}) \circledast e^{i\varphi'} \bar{\Omega}_1(\mathbf{k}) \right] \bigg|_{\mathbf{k}=0} = e^{-i2\varphi'} \left[ |\bar{\Omega}_{-1}(\mathbf{k})| \circledast |\bar{\Omega}_1(\mathbf{k})| \right] \bigg|_{\mathbf{k}=0}.$$
$$(4.32)$$

By calculating the argument of $\mathcal{C}_{-1,1}(\mathbf{k} = 0)$, we can obtain

$$\arg\left[ \mathcal{C}_{-1,1}(\mathbf{k} = 0) \right] = -2\varphi' + 2n\pi, \qquad (4.33)$$

where $n$ denotes an integer. From Eq. 4.33, the estimated global phase $\varphi'_{\text{est}}$ is given by

$$\varphi'_{\text{est}} = -\frac{1}{2}\arg\left[ \mathcal{C}_{-1,1}(\mathbf{k} = 0) \right] = \varphi' - n\pi. \qquad (4.34)$$

To compensate the phase factor of the $\pm 1^{\text{st}}$-order components, the components are multiplied by $e^{\mp i\varphi'_{\text{est}}}$:

$$e^{\pm i\varphi'} \bar{\Omega}_{\pm 1}(\mathbf{k}) \rightarrow e^{\pm in\pi} \bar{\Omega}_{\pm 1}(\mathbf{k}). \qquad (4.35)$$

After the recombination of the individual components $e^{in\pi} \bar{\Omega}_{\pm 1}(\mathbf{k})$ (note that $n$ is an integer such that $e^{\pm in\pi} \bar{\Omega}_{\pm 1}(\mathbf{k}) = e^{in\pi} \bar{\Omega}_{\pm 1}(\mathbf{k})$) with different pattern orientations $\phi$, the reconstructed chiral SIM image in Fourier space should be given by

$$\bar{M}_{rec}(\mathbf{k}) = -e^{in\pi} \frac{\sum_{l'=\pm 1,\phi} \bar{h}^* \left( \mathbf{k} + l' \mathbf{k}'_\phi \right) \bar{\Omega}_{l'}(\mathbf{k})}{\sum_{l'=\pm 1,\phi} \left| \bar{h} \left( \mathbf{k} + l' \mathbf{k}'_\phi \right) \right|^2 + w}. \qquad (4.36)$$

Importantly, the parity of $n$ in Eq. 4.36 affects the handedness of the chiral domains shown in the reconstructed chiral SIM image: if $n$ is odd, $e^{in\pi} = -1$ and the handedness of the chiral domains will be displayed in an opposite way in the image, leading to misinterpretation of the investigated sample. However, the parity of $n$ cannot be verified straightforwardly with the prior knowledge of the structured patterns or post-analysis of the subimages. One possible means to judge if we need to remedy the opposite handedness is to inspect the phase of the Fourier transform of a wide-field FDCD image at $\mathbf{k} = 0$. In theory, the phase of the Fourier transform of the wide-field FDCD image and chiral SIM image at $\mathbf{k} = 0$ should be identical. Thus, if the phase difference in the Fourier transform of the wide-field FDCD and the reconstructed chiral SIM image is $\pm\pi$ at $\mathbf{k} = 0$, $\bar{M}_{rec}(\mathbf{k})$ should be multiplied by $-1$ additionally to correct the handedness of the chiral domains shown in the chiral SIM image.

### 4.2.2 Illumination Scheme of Using Two CPL with Same Handedness

The schematic diagram that describes the illumination scheme of using two CPL is shown in Fig. 4.3. We assume that two CPL propagate towards the sample plane ($xy$-plane) at the same incident angle of $\theta$ ($\theta_1 = \theta_2 = \theta$). Accordingly, $\zeta_1 = \zeta_2 = \frac{\pi}{2}$ (LCPL) or $-\frac{\pi}{2}$ (RCPL) because these two plane waves are left-circularly polarized. The electric field amplitudes also become $E_{1,s} = E_{2,p} = E_{1,p} = E_{2,s} = \frac{1}{2}E_0$, where $\frac{1}{2}$ is a constant that normalizes the amplitudes. Likewise, the azimuth angle of these two CPL follows the relation of $|\phi_1 - \phi_2| = \pi$. Considering 4.8 and 4.9, the OC and electric energy density distribution generated by the interference of the two CPL are [103, 105]

$$C_{\pm,j}(\mathbf{r}) = \pm C_0 \mp C_1 \cos(\mathbf{k}' \cdot \mathbf{r} + \varphi_j), \qquad (4.37)$$

$$U_{e\pm,j}(\mathbf{r}) = U_{e,0} - U_{e,1} \cos(\mathbf{k}' \cdot \mathbf{r} + \varphi_j), \qquad (4.38)$$

where the signs $+$ and $-$ in the subscript indicate the usage of two LCPL and RCPL, respectively. $C_0 = n\,C_{\text{CPL}}$ and $U_{e,0}$ correspond to the strength of the $0^{\text{th}}$ harmonic term of the structured OC and electric energy density patterns, respectively, and also indicate an offset in these two structured patterns. $C_1$ and $U_{e,1} = U_{e,0} \cos^2 \theta$ correspond to the strength of the $1^{\text{st}}$ harmonic term of the structured OC and electric energy density
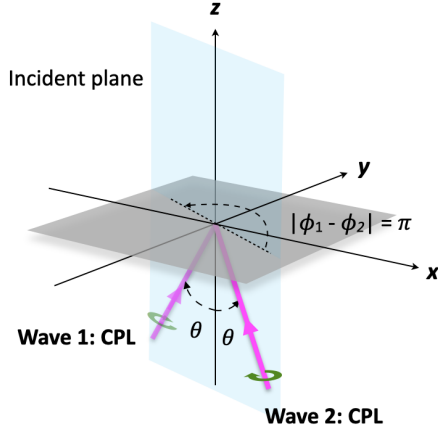
**Figure 4.3:** Schematics of using two CPL with the same handedness to generate structured OC patterns. The superposition of two LCPL or RCPL at an incident angle of $\theta$ forms both periodically structured OC and electric energy density distribution on the sample plane.

pattern and denote the amplitude of these two structured patterns. The phase of these two patterns is defined by

$$\varphi_j = \xi_1 - \xi_2, \tag{4.39}$$

which is slightly different from the pattern phase shown in Eq. 4.14. The wavevector of both OC and electric energy density patterns is given by

$$\mathbf{k}' = nk_0 \sin \theta \left[ \left( \cos \phi_1 - \cos \phi_2 \right) \hat{\mathbf{x}} + \left( \sin \phi_1 - \sin \phi_2 \right) \hat{\mathbf{y}} \right]$$

$$= 2nk_0 \sin \theta (\cos \phi \, \hat{\mathbf{x}} + \sin \phi \, \hat{\mathbf{y}}), \tag{4.40}$$

where we let $\phi_1 = \phi$ and $\phi_2 = \phi \pm \pi$ for simplicity. According to Eqs. 4.37 and 4.38, both structured OC and electric energy density patterns possess the same pattern period and orientation and we are able to rotate these two types of patterns by adjusting the azimuth angle of the two incident CPL while maintaining the relation of $|\phi_1 - \phi_2| = \pi$.

Crucially, Eqs. 4.37 and 4.38 also suggest that the structured distribution of electric energy density remains identical ($U_{e+,j}(\mathbf{r}) = U_{e-,j}(\mathbf{r})$) when the handedness of the OC pattern is altered ($C_{+,j}(\mathbf{r}) = -C_{-,j}(\mathbf{r})$). In this sense, the illumination scheme of using two CPL with the same handedness fulfills the requirements of the second scenario (Sec. 3.1.2). We can therefore decouple the CD-related signal from the one of electric dipole absorption by image subtraction. In the following, we formulate the process of the signal decoupling and the corresponding image reconstruction while applying the two-CPL illumination scheme in chiral SIM.

Considering Eqs. 3.7, 4.37 and 4.38, the subimages $M_{\pm,j}(\mathbf{r})$ acquired upon the illumination scheme of two LCPL and RCPL are given by

$$M_{\pm,j}(\mathbf{r}) = \frac{2\gamma}{\varepsilon_0}\Big\{\Big[\omega U_{e,0} + U_{e,1}\cos(\mathbf{k}'\cdot\mathbf{r}+\varphi_j)\Big]\alpha''(\mathbf{r})$$

$$\mp \Big[C_0 \pm C_1\cos(\mathbf{k}'\cdot\mathbf{r}+\varphi_j)\Big]G''(\mathbf{r})\Big\}\otimes h(\mathbf{r}), \qquad (4.41)$$

where the signs $+$ and $-$ in the subscript again denote the usage of two LCPL and RCPL, respectively. Following Eq. 3.12, we can obtain the differential images $M_j(\mathbf{r})$ after subtracting $M_{j,+}(\mathbf{r})$ from $M_{j,-}(\mathbf{r})$:

$$M_j(\mathbf{r}) = M_{j,+}(\mathbf{r}) - M_{j,-}(\mathbf{r})$$

$$= -\frac{4\gamma}{\varepsilon_0}\Big[C_0 - C_1\cos(\mathbf{k}'\cdot\mathbf{r}+\varphi_j)\Big]G''(\mathbf{r})\otimes h(\mathbf{r}). \qquad (4.42)$$

The corresponding Fourier transform of the differential images $\bar{M}_j(\mathbf{r})$ is therefore calculated as

$$\bar{M}_j(\mathbf{k}) = -\frac{4\gamma}{\varepsilon_0}\Big[C_0\bar{G}''(\mathbf{k}) - e^{-i\varphi_j}C_1\bar{G}''(\mathbf{k}+\mathbf{k}') - e^{i\varphi_j}C_1\bar{G}''(\mathbf{k}-\mathbf{k}')\Big]\bar{h}(\mathbf{k})$$

$$= \sum_{l=-1}^{1}\bar{\Omega}_l(\mathbf{k}-l\mathbf{k}')e^{il\varphi_j}, \qquad (4.43)$$

where $C_{-1} = C_1$ and the three individual components $\bar{\Omega}_l(\mathbf{k}-l\mathbf{k}')$ are given by

$$\bar{\Omega}_0(\mathbf{k}) = -\frac{4\gamma}{\varepsilon_0}\omega C_0\bar{G}''(\mathbf{k})\bar{h}(\mathbf{k}), \qquad (4.44)$$

$$\bar{\Omega}_{\pm 1}(\mathbf{k}\mp\mathbf{k}') = \frac{4\gamma}{\varepsilon_0}C_1\bar{G}''(\mathbf{k}\mp\mathbf{k}')\bar{h}(\mathbf{k}). \qquad (4.45)$$

According to Eqs. 4.44 and 4.45, all $\bar{\Omega}_l(\mathbf{k}-l\mathbf{k}')$ contain the CD-related signal. Therefore we do not discard any components during the image reconstruction. The favored sets for the pattern phases $\varphi_j$ and the orientation $\phi$ are the same as the ones described in Eqs. 4.19 and 4.23. In total, eighteen subimages (three pattern phases for each pattern orientation and two handedness of the incident CPL) are required for generating the differential images (Eq. 4.42) and then for the image reconstruction process. Because more raw images are acquired, the imaging rate of chiral SIM inevitably decreases at least by a factor of two compared to the case of using $s$- and $p$-polarized light. On the other

hand, since we do not discard the $0^{\text{th}}$-order component $\bar{\Omega}_0(\mathbf{k})$, the global phase can be determined by computing the cross-correlation between $\bar{\Omega}_0(\mathbf{k})$ and the position-corrected components $\bar{\Omega}_{\pm 1}(\mathbf{k})$ straightforwardly [108]. After we follow the similar component separation (Eq. 4.22), position correction (Eq. 4.24) and component recombination process illustrated in the previous section, the reconstructed chiral SIM image in Fourier space is represented by

$$\bar{M}_{rec}(\mathbf{k}) = -\frac{\sum_{l,\phi} \bar{h}^* \left( \mathbf{k} + l\mathbf{k}'_\phi \right) \bar{\Omega}_l(\mathbf{k})}{\sum_{l,\phi} \left| \bar{h} \left( \mathbf{k} + l\mathbf{k}'_\phi \right) \right|^2 + w}, \tag{4.46}$$

where $l = -1, 0, +1$ because we do not abandon the $0^{\text{th}}$-order component during the image reconstruction. Finally, the real-space chiral SIM image can be retrieved by performing the inverse Fourier transform of Eq. 4.46.

Intriguingly, this approach also allows to perform conventional SIM using the same set of the raw images $M_{j,\pm}(\mathbf{r})$ acquired upon the two CPL illumination. Here, if we sum up $M_{j,+}(\mathbf{r})$ and $M_{j,-}(\mathbf{r})$, which is given by

$$M_{sum,j}(\mathbf{r}) \equiv M_{j,+}(\mathbf{r}) + M_{j,-}(\mathbf{r})$$
$$= \frac{4\gamma}{\varepsilon_0} \omega \Big[ U_{e,0} + U_{e,1} \cos(\mathbf{k}' \cdot \mathbf{r} + \varphi_j) \Big] \alpha''(\mathbf{r}) \otimes h(\mathbf{r}), \tag{4.47}$$

it is clear that the CD-related signal is removed and only the signal from electric dipole absorption remains. By performing the typical SIM image reconstruction mentioned in Sec. 2.4, we can restore the high spatial frequency information and obtain the image of the normal fluorescent domains, i.e. $\alpha''(\mathbf{r})$, at super-resolution. This feature will also be demonstrated in Sec. 4.3.2.

## 4.3 Numerical Demonstration of Chiral SIM in the Absence of Noise

After formulating the image formation and reconstruction processes of chiral SIM, we aim to present the proof-of-concept demonstration based on numerical calculations. In this section, we introduce the synthetic samples, namely the chiral Siemens star and the nanobeads, used for the theoretical demonstrations. The excitation patterns generated using the interference of *s*- and *p*-polarized light and two CPL with the same handedness

are numerically simulated using the finite-difference time-domain (FDTD) method. These simulated patterns also verify the analytical expression we derived in the previous section. At the end, we present a series of theoretical demonstrations of chiral SIM that apply these two illumination schemes. To emphasize the resolution improvement offered by chiral SIM, comparisons between the conventional wide-field FDCD and chiral SIM images are provided. The effect of noise is neglected to demonstrate the superior resolving power of chiral SIM. The influence caused by the noise on the reconstructed chiral SIM image will be discussed in Sec. 5.1.

### 4.3.1 Synthetic Chiral Samples and Simulated Excitation Patterns

**Chiral Siemens Star**

A Siemens star made of one chiral domain embedded in the other one in the background, as shown in Fig. 4.4(a), is simulated as a chiral sample. The corresponding Fourier transform is displayed in Fig. 4.4(b). As a standard test target commonly used in optical imaging, the regular shape of the Siemens star provides a simple way to evaluate the resolution of a given microscopy method. The distance between the spokes decreases radially towards the center of the chiral Siemens star. The central area will be blurry if the resolution is not sufficient to distinguish two spokes, like the result presented in Fig. 2.7(a). Hence, we can compare the resolution of different microscopy techniques by observing the area of this haziness at the center: the smaller area we see, the better resolution it gains. On the other hand, the absolute value of the dissymmetry factor $g_{\mathrm{CPL}}$ of the chiral domains in the chiral Siemens star is set to be $10^{-3}$, which is at a similar scale to that of natural chiral species. Therefore, only two values of $g_{\mathrm{CPL}}$, namely $10^{-3}$ and $-10^{-3}$, are present in the chiral Siemens star and the background, respectively.
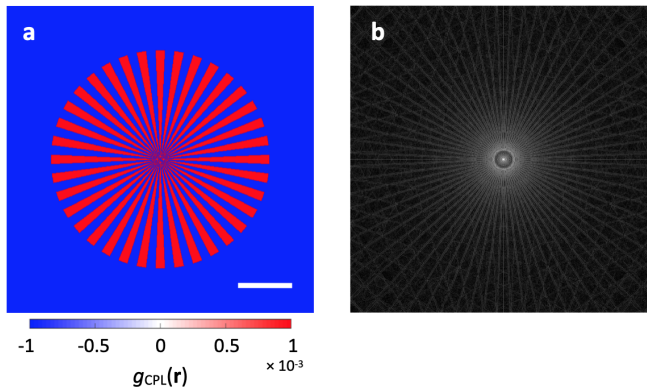


**Figure 4.4:** Synthetic chiral Siemens star. (a) Spatial distribution of the dissymmetry factor $g_{\mathrm{CPL}}(\mathbf{r})$ of the Siemens star. Scale bar: $2\,\mu\mathrm{m}$ (b) The corresponding Fourier transform.

## Randomly-Distributed Nanobeads

To mimic a realistic sample that may appear in experiments, we simulate a bead sample (Fig. 4.5(a) and (b)) for the chiral SIM demonstration. The diameter of those nanobeads is either 80 nm or 120 nm. Those beads are either achiral (marked by the yellow rectangle in Fig. 4.5(b)) or chiral (indicated by red or blue color in Fig. 4.5(a)) and randomly distributed in the region of interest. Note that since the dissymmetry factor $g_{CPL}(\mathbf{r})$ of the achiral beads is zero, they cannot be observed in Fig. 4.5(a) (see the area marked by the yellow rectangle). Some of the nanobeads are positioned very closely to inspect the performance of conventional wide-field microscopy and the chiral SIM method. Similar to the chiral Siemens star, the absolute value of $g_{CPL}$ of the chiral nanobeads is set to be $10^{-3}$, which is similar to that of natural chiral molecules.
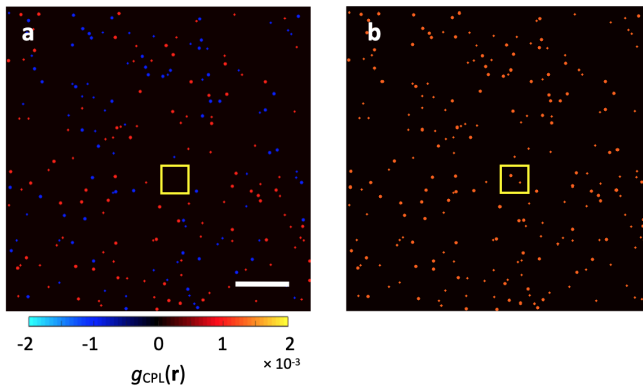


**Figure 4.5:** Synthetic nanobeads. (a) Spatial distribution of the dissymmetry factor $g_{CPL}(\mathbf{r})$ of the nanobeads. (b) Spatial distribution of the nanobeads. The yellow rectangles indicate the location of the achiral beads. Scale bar: 2 µm.

## Excitation Patterns

The excitation patterns $C_j(\mathbf{r})$ and $U_{e,j}(\mathbf{r})$ employed in the numerical demonstrations are simulated by the FDTD method (FDTD Solutions, Lumerical). In the simulations, the azimuth and incident angles of *s*- and *p*-polarized and two circularly polarized plane wave sources are determined according to the discussion in Secs. 4.2.1 and 4.2.2, respectively. The excitation wavelength is selected to be 532 nm and we assume an oil immersion objective whose numerical aperture (NA) is 1.2 is used for both illumination and collection. Therefore, the theoretical cut-off frequency of the OTF $k_{cutoff}$ is about $4.4 \times 10^{-3}$ nm$^{-1}$, as calculated from the reciprocal of Abbe diffraction limit (Eq. 2.22). The incident angle of the plane wave sources $\theta$ is set to be 41° to achieve a moderate resolution improvement of around 1.85, i.e. the ratio of $|\mathbf{k}'| = 2nk_0 \sin\theta$ to $k_{cutoff}$ is about 0.85. The structured patterns are generated in three in-plane orientations by adjusting the azimuth angle of the first and second waves $\phi_1$ and $\phi_2$ while the relation of $|\phi_1 - \phi_2| = \pi$ is maintained.
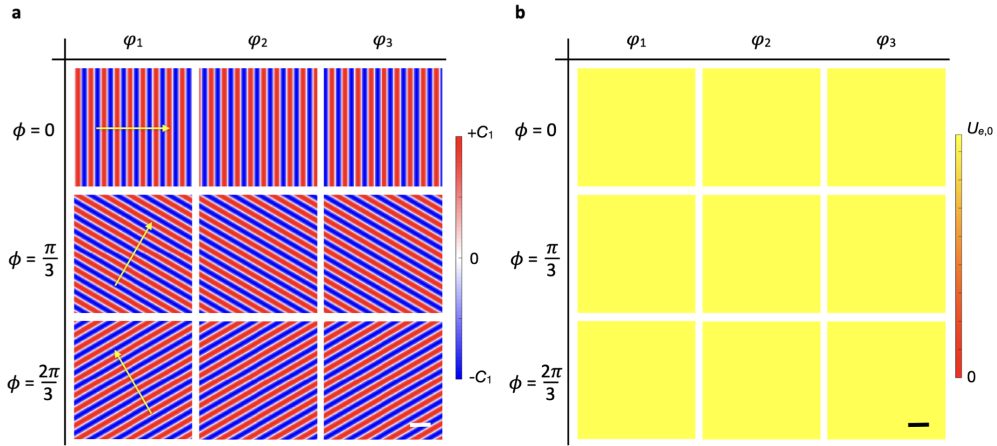
**Figure 4.6:** Simulated $C_j(\mathbf{r})$ and $U_{e,j}(\mathbf{r})$ when using *s*- and *p*-polarized light in the FDTD illumination. The two light sources are configured as illustrated in Fig. 4.2. (a) Zoom-in of $C_j(\mathbf{r})$ and (b) uniformly distributed $U_{e,j}(\mathbf{r})$ with respect to the pattern phase $\varphi_j$ and orientation $\phi$. Scale bar: 400 nm.
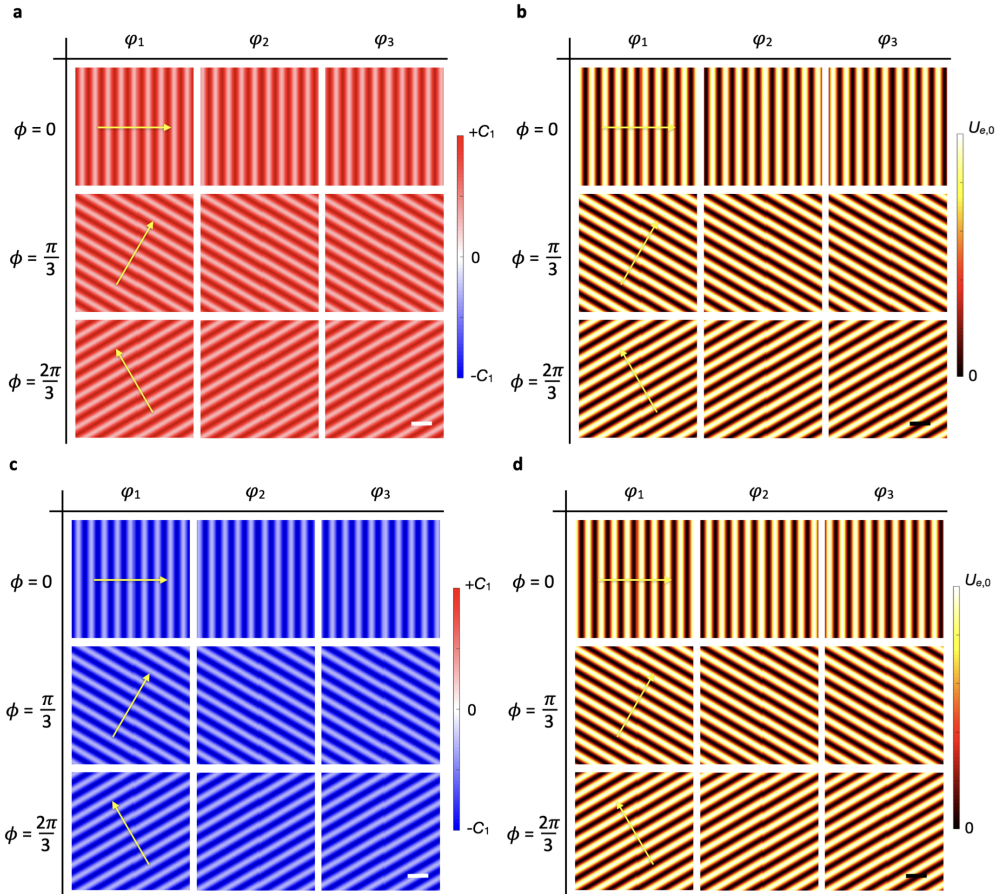


**Figure 4.7:** Simulated $C_j(\mathbf{r})$ and $U_{e,j}(\mathbf{r})$ when using two CPL in the FDTD illumination. The two light sources are configured as illustrated in Fig. 4.3. (a) Zoom-in of $C_{+,j}(\mathbf{r})$ and (b) $U_{e+,j}(\mathbf{r})$ with respect to the pattern phase $\varphi_j$ and orientation $\phi$ when two LCPL are applied. (c) Zoom-in of $C_{-,j}(\mathbf{r})$ and (d) $U_{e-,j}(\mathbf{r})$ with respect to the pattern phase $\varphi_j$ and orientation $\phi$ when two RCPL are applied. Scale bar: 400 nm.

According to Eq. 4.23, the pattern orientation $\phi$ varies from 0 to $\frac{2\pi}{3}$ successively. The structured patterns are shifted by tuning the initial phase of the plane waves $\xi_1$ and $\xi_2$

that relates to the pattern phase $\varphi_j$. Finally, a $z$-normal monitor where the mesh size is set to be $20 \times 20$ nm is placed on the $xy$-plane (appointed as the sample plane) to record the electromagnetic field distribution for calculating the excitation patterns.

When $s$- and $p$-polarized light are employed, $C_j(\mathbf{r})$ is structured into one-dimensional periodic patterns (Fig. 4.6(a)), of which orientation and phase vary according to $\phi$ and $\varphi_j$. In contrast, $U_{e,j}(\mathbf{r})$ remains constant even though $\phi$ and $\varphi_j$ change (Fig. 4.6(b)), which fulfills the requirements of the first scenario to decouple the CD-related signal. When two CPL are employed, both $C_j(\mathbf{r})$ (Figs. 4.7(a) and (c)) and $U_{e,j}(\mathbf{r})$ (Figs. 4.7(b) and (d)) are structured into periodic patterns. The value of the structured OC patterns is positive (negative) when two LCPL (RCPL) are applied. Meantime, the electric energy density distribution remains the same as the handedness of two CPL alters, which fulfill the requirements of the second scenario to decouple the CD-related signal. Overall, the FDTD-simulated excitation patterns are in good agreement with the analytical prediction indicated by Eqs. 4.11, 4.12, 4.37 and 4.38.

### 4.3.2 Theoretical Demonstration

For the theoretical demonstrations, the subimages employed in the chiral SIM image reconstruction are computed based on Eqs. 4.15 (using $s$- and $p$-polarized light) and 4.41 (using two CPL) with the FDTD-simulated illumination patterns (Figs. 4.6 and 4.7) in MATLAB R2017b (MathWorks, USA). The chiral SIM image reconstruction program is established by modifying the existing SIM image reconstruction program, which is written based on MATLAB built-in functions as well as the ones from an additional MATLAB toolbox named DIPimage [110]. We divide the demonstrations into two parts: applying the illumination schemes of (i) $s$- and $p$-polarized light and (ii) two CPL with the same handedness. In the demonstrations, nine (using $s$- and $p$-polarized light) or eighteen subimages (using two CPL) will undergo the chiral SIM image reconstruction process, as mathematically depicted in Secs. 4.2.1 and 4.2.2, respectively, to restore the high spatial frequency information on the chiral Siemens star and the nanobeads, generating the super-resolved chiral SIM image. The wide-field FDCD image, which is generated by subtracting the simulated images acquired upon the illumination of single LCPL from that of single RCPL, is also provided as a benchmark to highlight the resolution improvement shown in the reconstructed chiral SIM image. The wide-field FDCD images are also processed by the Wiener deconvolution method [110] for a fair comparison with the reconstructed chiral SIM images. All images of the chiral Siemens star and the

nanobeads are normalized to their largest pixel value and the maximum received photon number in the brightest pixel is set to be $10^5$. Here, we omit the noise that occurs during the image acquisition in both demonstrations to emphasize the significant resolution improvement shown in the reconstructed chiral SIM images.

## Part I – Using *S*- and *P*-Polarized Light

The deconvolved wide-field FDCD, reconstructed chiral SIM images and the corresponding Fourier transform of the chiral Siemens star are presented in Figs. 4.8(a-d), respectively. Compare to the wide-field FDCD image (Fig. 4.8(a)), the unresolved area in the chiral SIM image (Fig. 4.8(b)) reduces and the edges of the spokes become more rigid. The bandwidth shown in the Fourier transform of the chiral SIM image (Fig. 4.8(d)) is expanded and beyond the OTF determined by the optical system (marked by the yellow dashed circle). All features mentioned above indicate that the resolution of chiral SIM is higher compared to the wide-field FDCD imaging method. It is worth noting that the boundaries between opposite chiral domains manifest themselves as pseudo achiral domains due to the finite spatial resolution, which is a universal feature of all CD images regardless of the imaging methods [39, 42]. We also present the wide-field FDCD and chiral SIM images of the nanobeads in Figs. 4.8(e) and (f), respectively. Compared to the wide-field FDCD image, the chiral SIM image demonstrates a better resolution.
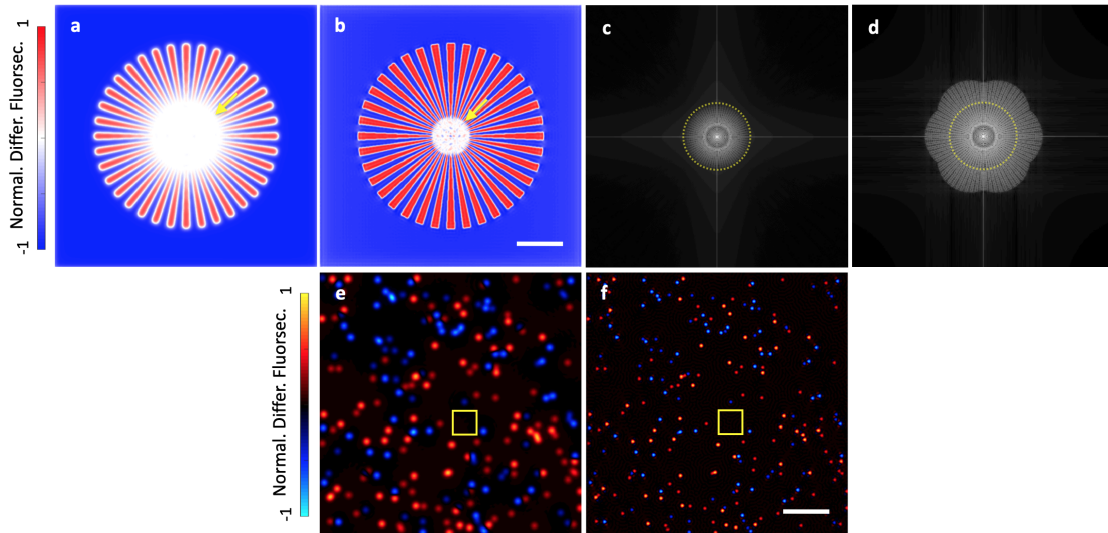


**Figure 4.8:** Numerical demonstration of chiral SIM where *s*- and *p*-polarized light are applied to acquire the subimages. (a) Deconvolved wide-field FDCD and (b) chiral SIM images of the chiral Siemens star. The yellow arrows indicate the edge of the unresolved area. Fourier transform of (c) the wide-field FDCD and (d) the chiral SIM images. The yellow dashed circles indicate the boundary of the OTF. (e) Deconvolved wide-field FDCD and (f) chiral SIM images of the nanobeads. The colorbars indicate the value of the normalized differential fluorescence. Scale bar: 2 μm.

Some groups of chiral beads merged in the wide-field FDCD image are well-separated in the reconstructed chiral SIM image, verifying the super-resolution provided by the chiral SIM method [104]. Note that because the wide-field FDCD microscopy and chiral SIM are chiral imaging methods, the achiral beads cannot be observed in the corresponding images (see the yellow rectangles in Figs. 4.8(e) and (f)).

**Part II – Using Two CPL**

The wide-field FDCD, chiral SIM, normal wide-field and SIM images of the nanobeads are presented in Figs. 4.9(a-d), respectively. Similar to the results in the previous demonstration, the chiral SIM image (Fig. 4.9(a)) shown in this demonstration also exhibits a higher resolution compared to the wide-field FDCD image (Fig. 4.9(b)). Several clusters of the unresolved chiral beads in the wide-field FDCD image are well-separated in the chiral SIM image thanks to the resolution improvement. However, since the wide-field FDCD microscopy and chiral SIM are both chiral imaging methods, the achiral beads cannot be discerned in the corresponding images (marked by the yellow rectangles in Figs. 4.9(a) and (b)). On the other hand, as shown in Eq. 4.47, we can use the same group of the subimages, which were used to produce the chiral SIM image shown in Fig. 4.9(b), to generate the subimages for reconstructing the conventional SIM image. In this way, the achiral beads, which cannot be observed in the wide-field FDCD and chiral SIM images, can be detected and imaged at super-resolution (Fig. 4.9(d)). Through this theoretical demonstration, the ability of chiral SIM that applies the illumination scheme of two CPL to simultaneously obtain the chiral and achiral domain distribution is numerically verified [105].
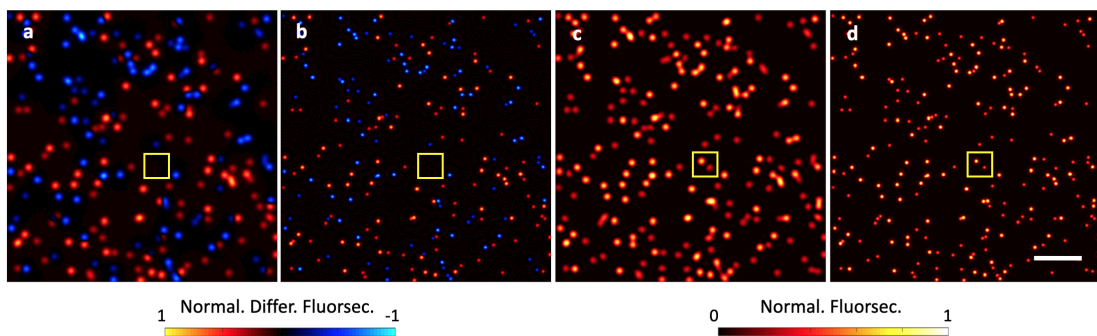


**Figure 4.9:** Numerical demonstration of chiral SIM and conventional SIM where two CPL are applied to acquire the subimages. (a) Deconvolved wide-field FDCD and (b) chiral SIM images of the nanobeads. The colorbar indicates the value of the normalized differential fluorescence. (c) Deconvolved wide-field and (d) SIM images of the nanobeads. The colorbar indicates the value of the normalized fluorescence. The yellow rectangles mark the location of the achiral beads. Scale bar: 2 μm.

# Chapter 5

# Challenges to Chiral SIM and the Potential Solutions

Natural chiral molecules hardly sense the field oscillation of electromagnetic plane waves because their size and the helical pitch of chiral light are not comparable. Interaction between light and chiral molecules is thus intrinsically weak, leading to a small dissymmetry factor of roughly $10^{-3}$ at visible wavelengths [15, 16]. Owing to this small factor, imaging natural chiral molecules is usually challenging since the noise becomes pronounced in acquired images. It is even more demanding for high-speed imaging as the acquisition time has to be very short and fewer photons can be collected by the detectors, resulting in the low signal-to-noise ratio (SNR). In this chapter, we focus on the effect of noise on the performance of chiral SIM and the possible means to enhance the image quality. The SNR of the reconstructed chiral SIM image is mathematically derived. With a series of numerical calculations and demonstrations, we inspect the effect of noise on the image quality under different experimental conditions. We also investigate the possibility of exploiting the superchiral near fields formed in the proximity of nanostructures to address the weak CD responses that lower the performance of chiral SIM. At last, the advantages and the main difficulty of applying such nanostructures in the chiral SIM are discussed.

## 5.1 Signal and Noise Analysis for Chiral SIM

In a real experiment, the recorded images are inevitably degraded by a variety of noise types, such as the readout noise and dark noise due to the readout process (e.g. charge transfer and analog-to-digital conversion) and thermally-induced free electrons. Besides, the arrival of photons at the camera sensor is a random process, leading to the so-called photon shot noise. In general, the readout noise of a modern imaging device, such as an sCMOS camera, has been much reduced ($\sim 1$ e$^{-}$ at the high readout rate [111]) owing to the advances of in-sensor architecture and fabrication. The dark noise can also be

managed appropriately by cooling the camera ($\sim 0.1$ e$^-$/pixel/s). Nevertheless, the shot noise cannot be removed by any practical means and is usually dominant among all sources of noise during image acquisition. In this regard, we here focus on the influence of the shot noise on the reconstructed chiral SIM images and omit the effects from the other types of noise as they are in principle addressable in an experiment. In the following, we formulate the SNR of the reconstructed chiral SIM image as a function of spatial frequency in Fourier space. As a measure frequently applied in noise analysis, SNR compares the expected signals with noise and is useful as a metric of image fidelity. Since the spatial features of complex samples can be Fourier decomposed into respective spatial frequencies, analysis of SNR in Fourier space provides a better insight into the influence of the noise than that in real space.

### 5.1.1 Signal-To-Noise Ratio of Reconstructed Chiral SIM Image

We here apply the illumination scheme of two *s*-and *p*-polarized light, as illustrated in Fig. 4.2, and calculate the SNR of the reconstructed image in Fourier space [112]. Considering the photon shot noise $N_{shot}(\mathbf{r})$ that occurs during the image acquisition, the subimages in real space can be expressed as

$$M'_j(\mathbf{r}) = M_j(\mathbf{r}) + N_{shot,j}(\mathbf{r}). \tag{5.1}$$

Then, the corresponding Fourier transform can be calculated as

$$
\begin{aligned}
\bar{M}'_j(\mathbf{k}) &= \bar{M}_j(\mathbf{k}) + \bar{N}_{shot,j}(\mathbf{k}) \\
&= \sum_{l=-1}^{1} \bar{\Omega}_l(\mathbf{k} - l\mathbf{k}')e^{il(j-1)\varphi_0} + \sum_{l=-1}^{1} \bar{\chi}_l(\mathbf{k} - l\mathbf{k}')e^{il(j-1)\varphi_0} \\
&= \sum_{l=-1}^{1} \bar{\Omega}'_l(\mathbf{k} - l\mathbf{k}')e^{il(j-1)\varphi_0}.
\end{aligned}
\tag{5.2}
$$

Here, $\bar{\Omega}'_l(\mathbf{k} - l\mathbf{k}') = \bar{\Omega}_l(\mathbf{k} - l\mathbf{k}') + \bar{\chi}_l(\mathbf{k} - l\mathbf{k}')$ denotes the individual components with the noise term $\bar{\chi}_l(\mathbf{k} - l\mathbf{k}')$, which is expressed by Fourier transform of $\bar{N}_{shot,j}(\mathbf{k})$ with respect to the pattern phase $\varphi_j$

$$\bar{\chi}_l(\mathbf{k}) = \frac{1}{3}\sum_{j=1}^{3} \bar{N}_{shot,j}(\mathbf{k})e^{-il(j-1)\varphi_0}. \tag{5.3}$$

Based on the derivation in Sec. 4.2.1, the Fourier transform of the reconstructed image in the presence of noise is given by

$$\bar{M}'_{rec}(\mathbf{k}) = -\frac{\sum_{l'=\pm1,\theta} \bar{h}^*\left(\mathbf{k}+l'\mathbf{k}'_\theta\right)\bar{\Omega}'_{l'}(\mathbf{k})}{\sum_{l'=\pm1,\theta}\left|\bar{h}\left(\mathbf{k}+l'\mathbf{k}'_\theta\right)\right|^2 + w}$$

$$= \bar{M}_{rec}(\mathbf{k}) - \frac{\sum_{l'=\pm1,\theta} \bar{h}^*\left(\mathbf{k}+l'\mathbf{k}'_\theta\right)\bar{\chi}'_{l'}(\mathbf{k})}{\sum_{l'=\pm1,\theta}\left|\bar{h}\left(\mathbf{k}+l'\mathbf{k}'_\theta\right)\right|^2 + w}. \tag{5.4}$$

To derive the SNR of the reconstructed chiral SIM image in Fourier space, we need to calculate the variance of $\bar{M}'_{rec}(\mathbf{k})$:

$$\mathrm{Var}\left[\bar{M}'_{rec}(\mathbf{k})\right] = \mathrm{Var}\left[-\frac{\sum_{l'=\pm1,\theta} \bar{h}^*\left(\mathbf{k}+l'\mathbf{k}'_\theta\right)\bar{\chi}'_{l'}(\mathbf{k})}{\sum_{l'=\pm1,\theta}\left|\bar{h}\left(\mathbf{k}+l'\mathbf{k}'_\theta\right)\right|^2 + w}\right]$$

$$= \frac{\sum_{l'=\pm1,\theta}\left|\bar{h}^*\left(\mathbf{k}+l'\mathbf{k}'_\theta\right)\right|^2}{\left(\sum_{l'=\pm1,\theta}\left|\bar{h}\left(\mathbf{k}+l'\mathbf{k}'_\theta\right)\right|^2 + w\right)^2}\mathrm{Var}\left[\bar{\chi}'_{l'}(\mathbf{k})\right]. \tag{5.5}$$

Considering the derivation of $\mathrm{Var}\left[\bar{\chi}'_{l'}(\mathbf{k})\right]$ in Appendix C, Eq. 5.5 can be simplified as

$$\mathrm{Var}\left[\bar{M}'_{rec}(\mathbf{k})\right] = \frac{\sum_{l'=\pm1,\theta}\left|\bar{h}^*\left(\mathbf{k}+l'\mathbf{k}'_\theta\right)\right|^2}{\left(\sum_{l'=\pm1,\theta}\left|\bar{h}\left(\mathbf{k}+l'\mathbf{k}'_\theta\right)\right|^2 + w\right)^2}\left(\frac{\varepsilon\omega U_{e,0}\bar{\alpha}''(0)\bar{h}(0)}{6\gamma}\right). \tag{5.6}$$

Finally, the SNR of the reconstructed chiral SIM image in Fourier space is given by

$$\mathrm{SNR}(\mathbf{k}) = \frac{\bar{M}_{rec}(\mathbf{k})}{\sqrt{\mathrm{Var}\left[\bar{M}'_{rec}(\mathbf{k})\right]}}$$

$$= \frac{C_1\bar{G}''(\mathbf{k})}{\sqrt{\omega U_{e,0}\bar{\alpha}''(0)}}\sqrt{\frac{6\gamma}{\varepsilon}}\sqrt{\frac{\sum_{l'=\pm1,\theta}\left|\bar{h}(\mathbf{k}-l'\mathbf{k}'_\theta)\right|^2}{\bar{h}(0)}}. \tag{5.7}$$

By substituting Eqs. 4.12 and 4.37 into Eq. 5.7 can be further simplified as

$$\mathrm{SNR}(\mathbf{k}) = \frac{\bar{G}''(\mathbf{k})}{\sqrt{\bar{\alpha}''(0)}}\frac{\cos^2\psi}{c}E_0\sqrt{6\gamma}\sqrt{\frac{\sum_{l'=\pm1,\theta}\left|\bar{h}(\mathbf{k}-l'\mathbf{k}'_\theta)\right|^2}{\bar{h}(0)}}$$

$$= \frac{\bar{G}''(\mathbf{k})}{\sqrt{\bar{\alpha}''(0)}}\frac{\cos^2\psi}{c^{3/2}}\sqrt{\frac{12\omega I_0\gamma}{n\varepsilon_0}}\sqrt{\frac{\sum_{l'=\pm1,\theta}\left|\bar{h}(\mathbf{k}-l'\mathbf{k}'_\theta)\right|^2}{\bar{h}(0)}}, \tag{5.8}$$

where $I_0$ is the laser intensity, $c$ the speed of light and $\varepsilon_0$ the permittivity in vacuum.

Eq. 5.8 is instructive because it tells that the SNR of the reconstructed chiral SIM image in Fourier space is governed by multiple quantities. First of all, the strength of the CD response of the sample has a significant influence on the reconstructed image, which is reflected by the direct proportionality of SNR($\mathbf{k}$) to the Fourier spectrum of the molecular chiral polarizability $\bar{G}''(\mathbf{k})$. Secondly, chiral domains with smaller $\bar{\alpha}''(0)$, namely the sum of all pixel values in real space ($\bar{\alpha}''(0) = \sum_{\mathbf{r}} \alpha''(\mathbf{r})$), are expected to show a better SNR when other parameters remain the same because this helps the chirality-dependent signals of the sample to stand out from the electric dipole absorption ones. Thirdly, it is intuitive that enhancing the laser intensity on the sample $I_0$ improves the SNR of the reconstructed image. However, excessive laser intensity may give rise to unpleasant photobleaching of the fluorescent sample. Fourthly, the incident angle of the $s$- and $p$-polarized waves $\psi$ affects the SNR of the reconstructed image because the amplitude of the OC excitation patterns $C_1$ is proportional to $\cos^2 \psi$: the SNR improves when $\cos^2 \psi$ increases. However, it should be noted that this improvement is at the price of lowering the spatial frequency of the OC patterns as $|\mathbf{k}'|$ is proportional to $\sin \psi$ (Eq. 4.13). Finally, we assume the proportionality constant $\gamma$ relates to the quantum yield $\Phi_q$, the detection efficiency of the imaging system $\beta_d$, the number of fluorophores $\eta$, and the exposure time $\Delta t$, i.e. $\gamma = \Phi_q \beta_d \eta \Delta t$. Since the SNR is proportional to the square root of $\gamma$, prolonging $\Delta t$, selecting the fluorophore or fluorescent sample with high $\Phi_q$, improving the detection efficiency of the imaging system $\beta_d$, and increasing the fluorophore number $\eta$ within a voxel can all enhance the SNR.

## 5.2 Numerical Demonstration of Chiral SIM in the Presence of Noise

To illustrate the effect of noise on the quality of the reconstructed chiral SIM image, in this section, we present a series of numerical demonstrations under different experimental conditions and calculate the corresponding SNR as a measure of the image quality. Synthetic chiral filaments are simulated for mimicking a real biological sample and are applied in the demonstrations. All images are degraded by only the shot noise since other types of noise are not dominant during the image acquisition.

## 5.2.1 Synthetic Chiral Samples

### Chiral Filaments

We design a new chiral sample, termed the chiral filaments, with irregular shapes and orientations to mimic a biological sample in a real experiment (Fig. 5.1). One important feature of this filament sample is that the chiral domains are inhomogeneously distributed within each filament, rendering this synthetic sample more realistic. We assume these chiral filaments are labeled by the fluorophores that have similar molecular and optical properties to Rhodamine 6G (R6G), which is one of the widely used dyes in fluorescence microscopy with the absorption maximum at approximately 532 nm. Apart from the spectral properties, the quantum yield $\Phi_q$ and the imaginary part of the polarizability $\alpha''$ of the fluorophore should be similar to those of R6G, which are 0.95 [113] and $6 \times 10^{-38}$ A$^2$s$^4$kg$^{-1}$ [114], respectively. To fulfill the criteria of FDCD, the fluorophores are supposed to form the corresponding fluorescent chiral assembly and freely rotate after attaching to the chiral structure of the filaments. In this sense, the fluorescence emitted from the fluorophores should be CD-dependent, i.e. the emission strength solely depends on the CD that originates from the filament chirality. We specify the spatial distribution of the dissymmetry factor $g_{\text{CPL}}(\mathbf{r})$ to describe the CD response of the local domains within the filaments (Fig. 5.1(a)) and calculate the corresponding Fourier transform of the filament sample (Fig. 5.1(b)). The value of $g_{\text{CPL}}(\mathbf{r})$ ranges from $-4 \times 10^{-4}$ to $4 \times 10^{-4}$ because the filament sample is designed to imitate ordinary chiral species whose $g_{\text{CPL}}$ is at the scale of $10^{-3} \sim 10^{-4}$. Finally, we assume around five fluorophores occupy each pixel where the chiral filaments reside, i.e. $\eta = 5$. This corresponds to a relatively high molecular density such that all chiral filaments are supposed to be fully labeled and the distribution of $g_{\text{CPL}}(\mathbf{r})$ can be well-characterized by the emitted CD-dependent fluorescence.
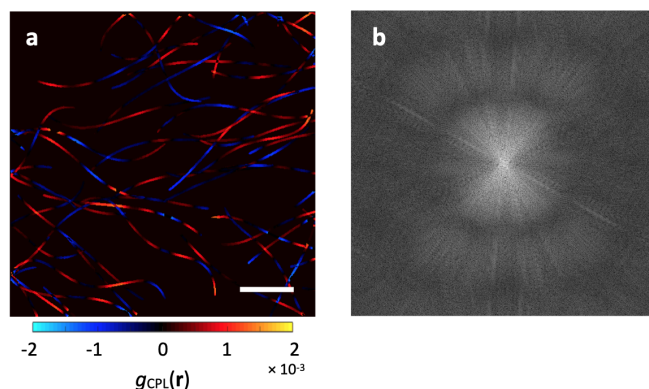


**Figure 5.1:** Synthetic chiral filaments. (a) Spatial distribution of the dissymmetry factor $g_{\text{CPL}}(\mathbf{r})$. Scale bar: 2 µm (b) The corresponding Fourier transform.

### 5.2.2 Theoretical Demonstrations

In the numerical simulations, the shot noise is introduced during the image formation using the noise function in the DIPimage toolbox [110]. We consider different experimental conditions and change the parameters accordingly. All the deconvolved wide-field FDCD and reconstructed chiral SIM images shown in the demonstrations are normalized to their maximum pixel value within the region of interest. We select the illumination scheme of *s*- and *p*-polarized light with the same configuration described in Fig. 4.2 and thus the FDTD-simulated excitation patterns shown in Sec. 4.3.1 are applied again. SNR($\mathbf{k}$) (Eq. 5.8) is averaged along the azimuth angle in Fourier space, as shown in the following

$$\text{SNR}_{\text{avg}}(k) = \frac{\sum_{|\mathbf{k}|=k} \text{SNR}(\mathbf{k})}{Q}, \tag{5.9}$$

in order to present the SNR of the final image with respect to different spatial frequencies of the chiral filaments, regardless of the orientations in Fourier space. Here, $Q$ denotes the number of the discrete data points in the Fourier transform of the reconstructed chiral SIM image as $|\mathbf{k}| = k$ [112].

#### Effect of the Strength of CD Response on Chiral SIM Image Quality

In order to view the effect of the strength of the CD response on the image quality, we enhance the dissymmetry factor by multiplying $g_{\text{CPL}}(\mathbf{r})$ by a factor of $m$, where $m = 1, 10, 100$. The exposure time $\Delta t$ and laser intensity $I_0$ are set to be 1 s and 50 W/cm$^2$, respectively, for a modest experimental condition.

We present the simulated deconvolved wide-field FDCD and reconstructed chiral SIM images of the filament sample with $m = 1, 10, 100$ in Fig. 5.2. When $m = 1$, we can observe many artifacts in both wide-field FDCD (Fig. 5.2(a)) and chiral SIM images (Fig. 5.2(d)), which severely degrade the image quality. This means the FDCD signal from the chiral filaments with ordinary CD response is very weak such that it cannot compete with the shot noise. Neither the deconvolution method nor the chiral SIM image reconstruction can restore the information on the chiral domains properly. On the contrary, the image quality is much improved when $m = 10$ (Figs. 5.2(b) and (e)) and 100 (Figs. 5.2(c) and (f)). Also, the chiral SIM images (Figs. 5.2(e) and (f)) exhibit superior resolution compared to the wide-field FDCD images (Figs. 5.2(b) and (c)). Some filaments which were merged in the wide-field FDCD images are well-resolved in the chiral SIM images. In general, the quality of the chiral SIM images (Figs. 5.2(d-f))

highly relates to the strength of the CD response. A sufficiently large dissymmetry factor is required for the image reconstruction. If the dissymmetry factor of the sample is too small, the noise could become much pronounced than the FDCD signal and thus hampers the chiral SIM image reconstruction and degrades the image quality.

In addition to the reconstructed chiral SIM images, $\mathrm{SNR_{avg}}(k)$ also provides useful information on the effect of noise (Fig. 5.3). As expected, the magnitude of $\mathrm{SNR_{avg}}(k)$ at low spatial frequency is higher than that at high spatial frequency because the OTF of the optical imaging system behaves like a low-pass filter in Fourier space during the image acquisition. In the cases of $m = 10$ and $100$, $\mathrm{SNR_{avg}}(k)$ remains sufficiently large even when $k > k_{cutoff}$. This agrees with the observation of the resolution improvement in the chiral SIM images displayed in Figs. 5.2(e) and (f). Eventually, $\mathrm{SNR_{avg}}(k)$ drops
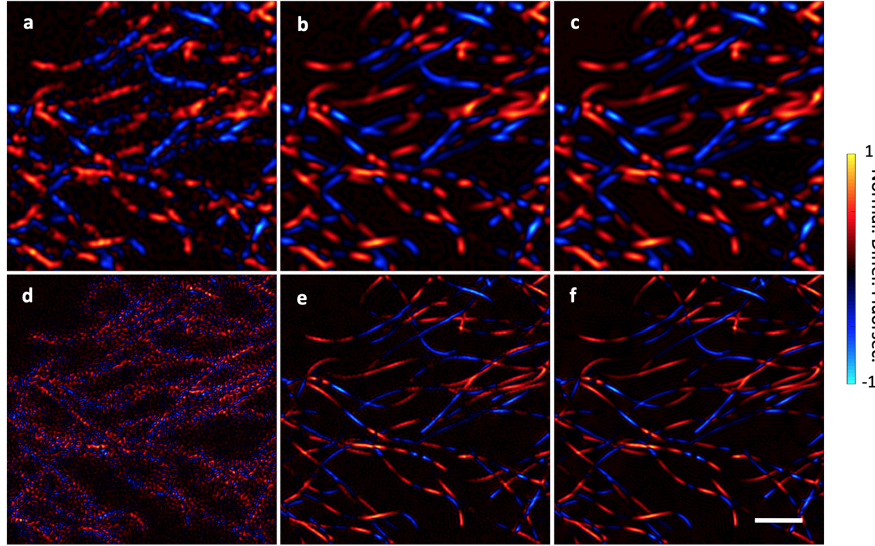


**Figure 5.2:** Theoretical demonstration of chiral SIM in the presence of shot noise. The strength of the dissymmetry factor is controlled by the multiplication factor $m$. $\Delta t = 1$ s and $I_0 = 50$ W/cm$^2$. (a-c) Deconvolved wide-field FDCD images with $m = 1, 10, 100$, respectively. (d-f) Reconstructed chiral SIM images with $m = 1, 10, 100$, respectively. The colorbar indicates the value of the normalized differential fluorescence. Scale bar: 2 μm.
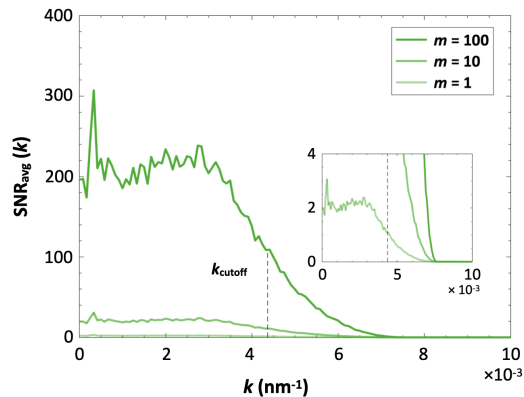


**Figure 5.3:** $\mathrm{SNR_{avg}}(k)$ when $m = 1, 10, 100$. The black dashed line indicates $k_{cutoff}$ of the optical system. The inset shows the zoom-in of the green curves. Note that $k_{cutoff} \approx 4.4 \times 10^{-3}$ nm$^{-1}$ when the emission wavelength of the fluorophore and NA of the objective are 550 nm and 1.2, respectively.

drastically as $k$ approaches the theoretical bandwidth of the effective OTF, which is roughly 1.85-fold of $k_{cutoff}$ in this demonstration. On the contrary, in the case of $m$ = 1, $\text{SNR}_{\text{avg}}(k)$ is below unity when $k > k_{cutoff}$ and thus it is should be insufficient to generate a chiral SIM image with good quality. This is confirmed by the fact that the reconstructed chiral SIM image shown in Fig. 5.2(d) is significantly degraded and fails to reveal the true features of the chiral domains.

**Effect of the Exposure Time on Chiral SIM Image Quality**

Figure 5.2(d) in the last theoretical simulations suggests that the FDCD signal emitted from the chiral filaments with ordinary CD response (i.e. $m = 1$) is inadequate to overcome the photon shot noise. Therefore, as Eq. 5.8 indicates, we consider prolonging the exposure time $\Delta t$ to enhance the SNR of the reconstructed chiral SIM image.

We first analyze the SNR of the reconstructed chiral SIM images in Fourier space with different $\Delta t$. Figure 5.4 displays the curves of $\text{SNR}_{\text{avg}}(k)$ at $k = 1.85 k_{cutoff}$ (i.e. $\text{SNR}_{\text{avg}}(1.85 k_{cutoff})$) with respect to $m$, where $I_0 = 50$ W/cm$^2$ for moderate illumination intensity and $\Delta t = 1, 10, 50, 100$ s. As mentioned previously, the ratio of $|\mathbf{k}'|$ to $k_{cutoff}$ is set to be 0.85 in order to gain a moderate resolution improvement. In this sense, the theoretical bandwidth of the effective OTF in Fourier space is at $1.85 k_{cutoff}$ and $\text{SNR}_{\text{avg}}(1.85 k_{cutoff})$ has to reach a threshold in order to obtain reasonable image quality for observing the resolution improvement. Since the image obtained when $m = 10$ and $\Delta t = 1$ s (Fig. 5.2(e)) demonstrates decent image quality, we use the corresponding $\text{SNR}_{\text{avg}}(1.85 k_{cutoff})$ as the threshold for the comparison in Fig. 5.4 (indicated by a black arrow). This means any experimental conditions that let $\text{SNR}_{\text{avg}}(1.85 k_{cutoff})$ sit in the gray zone in Fig. 5.4 are considered not generating reasonably good images. As can be seen in Fig. 5.4, when $\Delta t = 100$ s, the value of $\text{SNR}_{\text{avg}}(1.85 k_{cutoff})$ is always larger than the threshold (referred to the darkest red curve in Fig. 5.4). Therefore, we expect the quality of the reconstructed chiral SIM image to be good in the experimental condition of $\Delta t \geq 100$ s. On the contrary, when $\Delta t < 100$ s, the corresponding curves are all in the gray zone if $m = 1$. Accordingly, the quality of the reconstructed chiral SIM images should be unsatisfactory in the experimental condition of $\Delta t = 50$ and 10 s as the chiral filaments with ordinary CD response are applied. Those conclusions will be verified by the numerical simulations in the following.

We present the simulated deconvolved wide-field FDCD and reconstructed chiral SIM images of the ordinary filament sample (i.e. $m = 1$) with $\Delta t = 10, 50, 100$ s in Fig.

5.5. $I_0$ is again set to be 50 W/cm$^2$ for moderate illumination intensity. Clearly, the quality of the wide-field FDCD (Figs. 5.5(a-c)) and reconstructed chiral SIM images (Figs. 5.5(d-f)) is improved as $\Delta t$ is increased. When $\Delta t = 100$ s, the chiral SIM image (Fig. 5.5(f)) has good image quality, which is similar to that of the chiral SIM image shown in Fig. 5.2(e) ($m = 10$ and $\Delta t = 1$ s). In addition, as compared to the wide-field FDCD images with $\Delta t = 10$ s (Fig. 5.5(a)) and 50 s (Fig. 5.5(b)), the resolution of the chiral SIM images with $\Delta t = 10$ s (Fig. 5.5(d)) and 50 s (Fig. 5.5(e)) is improved. However, the sparse artifacts in the chiral SIM images with $\Delta t = 10$ s and 50 s may still cause misinterpretation of the sample details. Overall, the quality of the simulated chiral SIM images in Fig. 5.5 is in good agreement with the expectation inferred from the theoretical curves shown in Fig. 5.4.
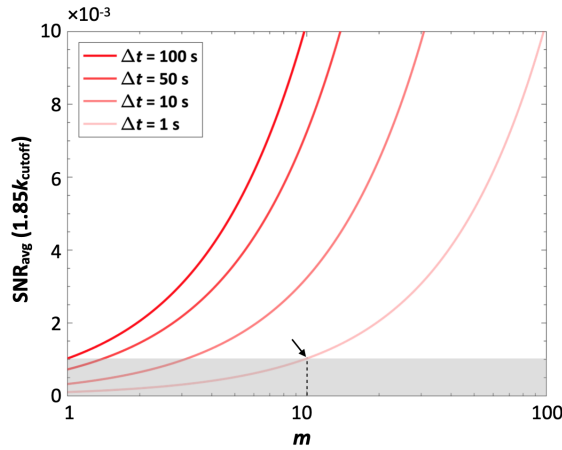


**Figure 5.4:** $\mathrm{SNR}_{\mathrm{avg}}(1.85k_{cutoff})$ as a function of $m$ when $\Delta t = 1, 10, 50, 100$ s. The black arrow indicates the corresponding $\mathrm{SNR}_{\mathrm{avg}}(1.85k_{cutoff})$ when $m = 10$ and $\Delta t = 1$. The experimental conditions that let $\mathrm{SNR}_{\mathrm{avg}}(1.85k_{cutoff})$ be in the gray zone are considered not generating chiral SIM images with good quality.
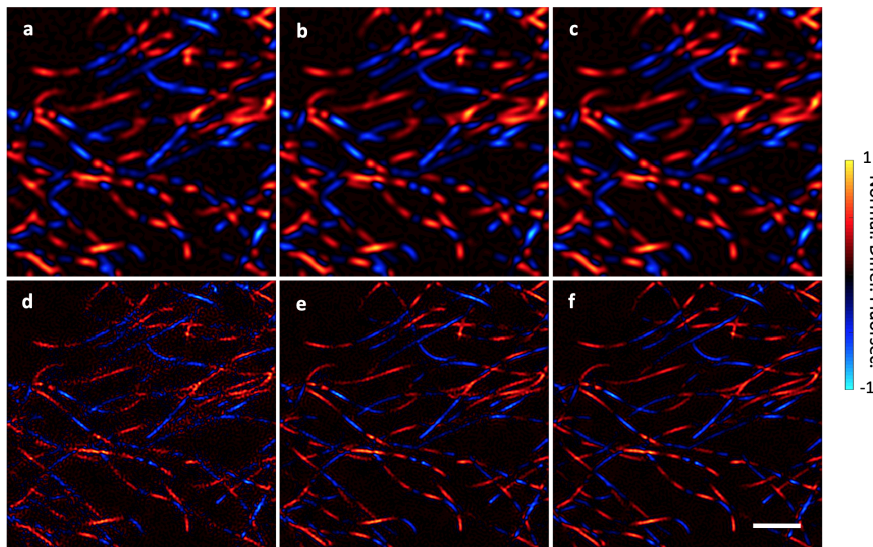


**Figure 5.5:** Theoretical demonstration of chiral SIM in the presence of shot noise. $I_0 = 50$ W/cm$^2$ and $m = 1$. (a-c) Deconvolved wide-field FDCD images with $\Delta t = 10, 50, 100$ s, respectively. (d-f) Reconstructed chiral SIM images with $\Delta t = 10, 50, 100$ s, respectively. The colorbar indicates the value of the normalized differential fluorescence. Scale bar: $2\,\mu$m.

**Effect of Laser Intensity on Chiral SIM Image Quality**

While prolonging $\Delta t$ fairly improves the quality of chiral SIM images, it is at the expense of imaging speed, which is not preferred in rapid imaging. Alternatively, we can consider improving the SNR by increasing the laser intensity $I_0$. However, increasing $I_0$ is sometimes unfavored in fluorescence microscopy as it may lead to photobleaching of the fluorophores. Moreover, as we will show in the following, increasing $I_0$ is not as effective in increasing the SNR as the means discussed in the previous sections.

Figure 5.6 shows the curves of $\mathrm{SNR_{avg}}(1.85k_{cutoff})$ as a function of $m$ when $I_0 = 50, 100, 1000, 5000$ W/cm$^2$, which are comparable to the laser intensity applied in normal wide-field and confocal fluorescence microscopy [115]. Here, we set $\Delta t$ to be 20 ms, which provides a frame rate of approximately 5.55 fps (20 ms for each subimage and in total nine subimages are required for one chiral SIM image). When $1 < m < 10$, all the curves sit in the gray zone. This means even at a relatively low frame rate of 5.5 fps and with high intensity of 5000 W/cm$^2$, the FDCD signal should still be insufficient to overcome the shot noise, leading to poor image quality. This conclusion is confirmed by the images shown in Fig. 5.7, where we present the wide-field FDCD and chiral SIM images of the ordinary filament sample ($m = 1$) with $I_0 = 100, 1000, 5000$ W/cm$^2$. $\Delta t$ is set to be 20 ms for the frame rate of 5.5 fps. Apparently, all images in Fig. 5.7 are severely degraded by the noise. The artifacts in the wide-field FDCD (Figs. 5.7(a-c)) and chiral SIM images (Figs. 5.7(d-f)) are so prevailing that even the global shape of the filaments can hardly be recognized. In general, the quality of the chiral SIM images becomes poor when $\Delta t$ decreases. Fast imaging for ordinary chiral samples whose dissymmetry factor smaller than $10^{-3}$ still remains very challenging for the proposed chiral SIM method.
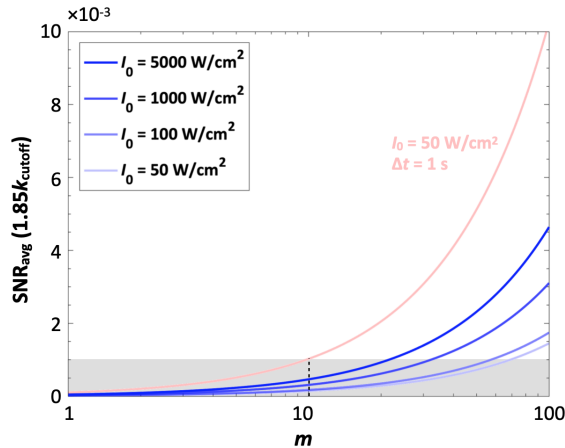


**Figure 5.6:** $\mathrm{SNR_{avg}}(1.85k_{cutoff})$ as a function of $m$ when $I_0 = 50, 100, 1000, 5000$ W/cm$^2$. $\Delta t$ is set to be 20 ms. The light red curve indicates the SNRavg $(1.85\ k_{cutoff})$ when $I_0 = 50$ W/cm$^2$ and $\Delta t = 1$ s. The experimental conditions that let $\mathrm{SNR_{avg}}(1.85k_{cutoff})$ sit in the gray zone are considered not generating chiral SIM images with good quality.
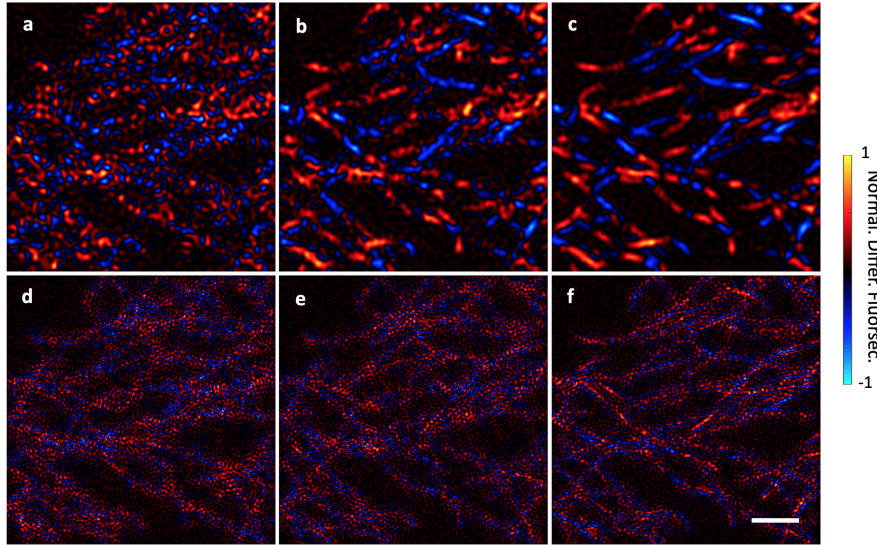
**Figure 5.7:** Theoretical demonstration of chiral SIM in the presence of shot noise. $\Delta t = 20$ ms and $m = 1$. (a-c) Deconvolved wide-field FDCD images with $I_0 = 100, 1000, 5000$ W/cm$^2$, respectively. (d-f) Reconstructed chiral SIM images with $I_0 = 100, 1000, 5000$ W/cm$^2$, respectively. The colorbar indicates the value of the normalized differential fluorescence. Scale bar: 2 µm.

## 5.3 Application of Nanostructures in Chiral SIM

According to Eq. 2.17, the CD-related signal is proportional to the OC of the excitation fields. Thus, enhancing the OC of the excitation light will strengthen the CD response. However, the difficulty of enhancing the OC in conventional optics lies in the fact that the OC of light in the far field reaches its uppermost strength if CPL is employed at the same wavelength [96]. This also means the strength of the OC generated by the interference of multiple far-field waves cannot exceed that of CPL when their intensity is normalized based on the number of the applied far-field waves. As a result, the far-field illumination schemes we have proposed in Sec. 4.1 are unable to boost the CD response of a given chiral sample. In contrast, electromagnetic fields with stronger OC compared to CPL, i.e. the superchiral fields, can be formed in the vicinity of plasmonic or dielectric nanostructures. As the CD response is enhanced by well-designed nanostructures, the exposure time could be shortened for high frame-rate imaging of ordinary chiral samples. In this sense, applying the nanostructures that offer such superchiral near fields is an attractive solution. The following sections discuss the advantages and the current issues of implementing such nanostructures in the proposed chiral SIM method.

### 5.3.1 Advantages of Using Nanostructures in Chiral SIM

**Strengthen the Chiral Light-Matter Interaction**

Various plasmonic [96, 116–131] and dielectric [124, 131–147] nanostructures have been proposed or experimentally implemented as a platform to generate the superchiral fields in the near field, leading to the reinforcement of the chiral response. Based on Eq. 2.8, the generation of superchiral fields relies on an optimum nanostructure that offers the local electric and magnetic fields that are (i) parallel and highly enhanced, (ii) spatially overlapped and (iii) neither in-phase nor 180° out-of-phase (in the best case, 90° out-of-phase). If designed properly, both plasmonic and dielectric nanostructures can provide the field enhancement and thus form the desired superchiral near fields. The mechanism responsible for this field enhancement is different. Plasmonic nanostructures can be engineered to induce localized surface plasmon resonance, which explicitly strengthens the electric response and gives rise to the characteristic electric field enhancement. On the other hand, using dielectric nanostructures can boost the magnetic response and generate the enhanced magnetic field via, for example, the Mie resonance [145]. Moreover, the dielectric nanostructures can be, like the plasmonic counterparts, engineered to induce the electric dipole and magnetic dipole resonances simultaneously. Such phenomenon, called the Kerker effect [148, 149], is widely used to facilitate the OC enhancement around or within the dielectric nanostructures [136, 141, 142, 146, 147].

**Further Enhance the Resolving Power of Chiral SIM**

To produce the enhanced OC and electric energy density patterns that cover a large region of interest, the designed nanostructure should consist of many elementary units arranged into a micrometer-scale periodic array, such as an array in the square or hexagonal lattice. Meanwhile, the generated superchiral near fields need to be mostly distributed on the top surface of the whole nanostructure such that they are accessible to the chiral samples. The excitation patterns are generally specklelike because they are vaguely shaped by the geometry and the two-dimensional arrangement of the elementary units. The geometry of these elementary units is usually simple, such as disks, for certain symmetric patterns and the ease of fabrication. The working wavelength of the whole nanostructure could be tuned by adjusting the aspect ratio or the periodicity of the elementary units.

Importantly, the subimages acquired upon the excitation of these speckle patterns should no longer apply to chiral SIM image reconstruction because the reconstruction

algorithm can only operate with the subimages acquired upon the excitation of one-dimensional periodic patterns. In theory, this type of subimages can be processed by the blind SIM algorithm to obtain the super-resolved images [150]. Furthermore, because the lattice constant of the periodic array structures, which basically determines the spatial frequency of the excitation patterns, can be two or even one hundred nanometers depending on the design and the fabrication capabilities, the generated speckle patterns may possess very high spatial frequencies. As the sample is illuminated by such speckle patterns, more high spatial frequency information on the chiral sample is down-modulated and can be restored afterwards. Therefore, if an optimum nanostructure is applied, the resolving power of chiral SIM could be further improved, which is similar to the idea demonstrated in the localized plasmonic SIM (LPSIM) [85, 86, 151, 152].

### 5.3.2 Issue of Using Nanostructures in Chiral SIM

Although plasmonic and dielectric nanostructures seem useful to reinforce the CD response and the resolving power of chiral SIM, they still cannot be properly applied in the chiral SIM method. When a nanostructure works as an illumination platform in chiral SIM, the generated superchiral near fields should be switched multiple times to provide a sufficient number of subimages for blind SIM image reconstruction. In each switch, these near fields also have to enable the essential signal decoupling, ensuring these subimages can be used to generate chiral domain images. However, in spite of many investigations, the nanostructures that can form such superchiral fields have not yet been discovered. Applying nanostructures in chiral SIM thus remains a problem to be solved. In the following, we present one of our investigations as an example to illustrate this issue.

Inspired by LPSIM [85, 86, 151, 152] and the work from Solomon et al. [142], we select a hexagonally-packed periodic silicon disk array, whose lattice constant $a = 300$ nm, disk radius $r = 92$ nm and the disk height $h = 80$ nm (Fig. 5.8(a)), as an illumination platform and use the FDTD method (FDTD Solutions, Lumerical) to simulate the generated OC distribution $C(\mathbf{r})$ and electric energy density distribution $U_e(\mathbf{r})$ in the near field. Because these dielectric disks can maintain the phase property of the incident light [142], they are illuminated by CPL to concurrently generate strong electric and magnetic fields that possess a phase condition similar to CPL, giving rise to great OC enhancement. In the case where the CPL is normally incident on the array ($\theta = 0°$), the simulated transmission spectrum has a dip at around 540 nm (Fig. 5.8(b)), which correlates to the concurrent electric and magnetic resonances. Such resonances can also
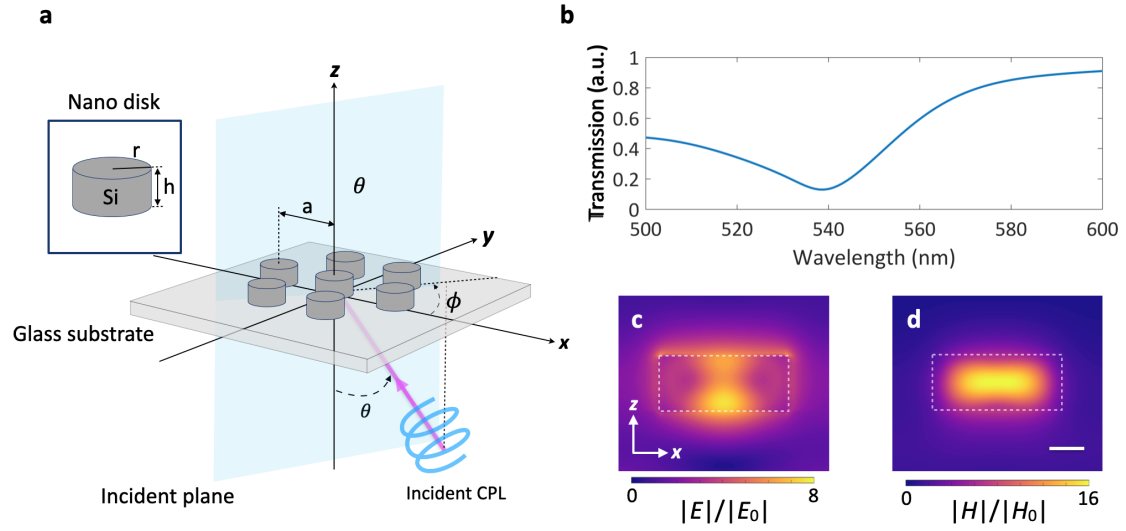
**Figure 5.8:** (a) Schematics of the hexagonally-packed periodic Si disk array in the FDTD simulation. The inset shows the geometric parameters of a single disk. $a = 300$ nm, $r = 92$ nm and $h = 80$ nm. (b) Simulated transmission spectrum of the disk array as $\theta = 0°$. (c) Simulated electric and (d) magnetic field enhancement of the disk array when $\lambda = 540$ nm and $\theta = 0°$. Scale bar: 50 nm.

be confirmed by the strong field enhancement in the disk (Figs. 5.8(c) and (d)). Besides, we can switch in different excitation patterns, as required by the blind SIM algorithm [85, 86, 150–152], by changing the incident angle $\theta$ and azimuth angle $\phi$ of the CPL.

Figure 5.9 shows the simulated OC enhancement distribution $C(\mathbf{r})/C_{\mathrm{CPL}}$ and $U_e(\mathbf{r})$, which are located 5 nm above the surface of the disks in the array. Here, $\lambda = 540$ nm and $C_{\mathrm{CPL}}$ denotes the OC of CPL. $\theta$ and $\phi$ are set to be $\{\theta = 0°, \phi = 0°\}$, $\{\theta = 30°, \phi = 0°\}$ and $\{\theta = 30°, \phi = 60°\}$, respectively, to generate different excitation patterns. Since this disk array supports the $C_3$ symmetry, the near-field distribution in the condition of $\{\theta = 30°, \phi = n \cdot 60°\}$, where $n$ is an integer, can be reasoned. Following the discussion in Sec. 3.1.2, these speckle patterns should fulfill the requirements illustrated in either scenario 1 or 2 to decouple the CD-related signal from the one related to electric dipole absorption. Because $C(\mathbf{r})/C_{\mathrm{CPL}}$ and $U_e(\mathbf{r})$ are complicated two-dimensional patterns (Figs. 5.9(a-l)), it is less likely to identify the harmonic components that only contain CD-related signal and then decouple them via Fourier analysis. On the other hand, when $C(\mathbf{r})$ alters because the handedness of the normally incident CPL changes (Figs. 5.9(a) and (b)), $U_e(\mathbf{r})$ stays identical (Figs. 5.9(c) and (d)). This means the CD-related signal can be decoupled via image subtraction of the two images obtained under this excitation condition, generating one applicable subimage. Still, as we set $\theta = 30°$ and keep $\phi = 0°$ to switch to other excitation patterns and generate another subimages, $U_e(\mathbf{r})$ changes (Figs. 5.9(g) and (h)) when the handedness of the CPL changes (Figs. 5.9(e)
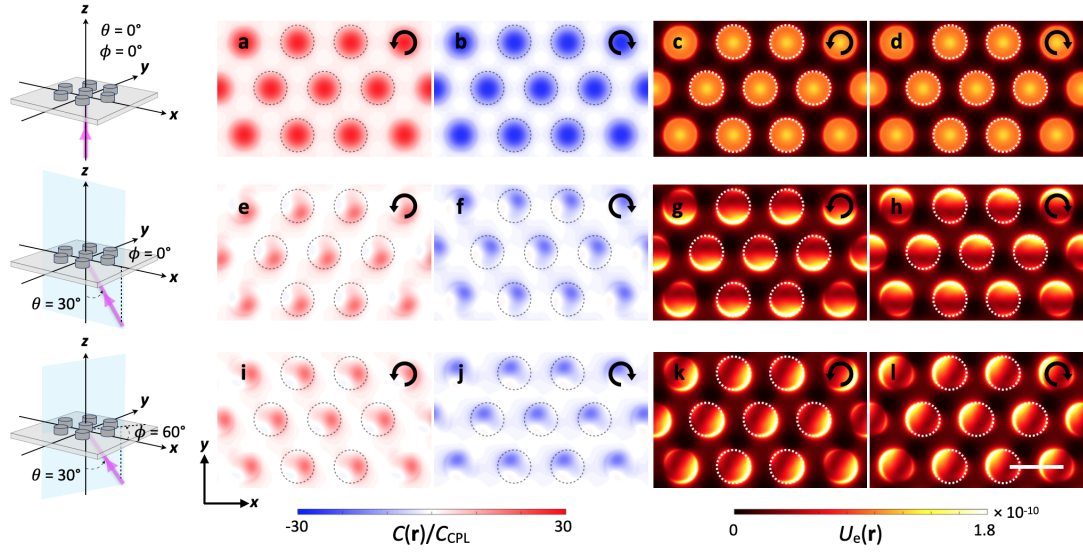
**Figure 5.9:** Simulated $C(\mathbf{r})/C_{\mathrm{CPL}}$ and $U_e(\mathbf{r})$ when the disk array shown in Fig. 5.8(a) is illuminated by the CPL with (a-d) $\phi = 0°$, $\theta = 0°$, (e-h) $\phi = 0°$, $\theta = 30°$, and (i-l) $\phi = 60°$, $\theta = 30°$. The circular arrows depict the incident polarization: the counterclockwise (clockwise) arrow indicates the left (right)-circular polarization. The white and black circular dotted lines indicate the position of part of the nanodisks. $C(\mathbf{r})/C_{\mathrm{CPL}}$ and $U_e(\mathbf{r})$ are calculated 5 nm above the surface of the disk array. $\lambda = 540$ nm. Scale bar: 300 nm.

and (f)). Similarly, as we keep $\theta = 30°$ and set $\phi = 60°$, the excitation pattern rotates accordingly and $U_e(\mathbf{r})$ still cannot remain the same when $C(\mathbf{r})$ alters (Figs. 5.9(i-l)). In this sense, the number of subimages applicable to the blind SIM algorithm is insufficient and we cannot reconstruct a super-resolved image of the chiral domains. We also obtain similar simulation results, i.e. $U_e(\mathbf{r})$ changes as the handedness of the obliquely incident CPL alters, when other nanostructures, such as hexagonally-packed periodic silver disk array or square-packed periodic silicon disk array, are illuminated by LCPL and RCPL successively. These results may originate from the spin-orbit coupling [153–155] of CPL. Therefore, it is difficult to maintain the spatial distribution of the local electric energy density while the handedness of CPL is switched. Also, according to our investigation, the superchiral near fields generated when these nanostructures are illuminated by LPL cannot be sculpted to enable the essential signal decoupling.

In conclusion, a design of nanostructures that is feasible to decouple the CD-related signal and generate adequate subimages has, to the best of our knowledge, not yet been discovered. Further efforts are needed to address this issue to improve the performance of the chiral SIM technique.

# Chapter 6

# Experimental Attempts at Chiral SIM

In previous chapters, we have formulated the working principle of chiral SIM and presented numerical demonstrations. Ultimately, we would like to provide a proof-of-concept experiment and image the molecular chirality distribution at super-resolution in a real experiment. This chapter illustrates our experimental attempts at the chiral SIM method. We first shortly introduce the chiral sample, namely the annealed chiral polyfluorene films, we select for the chiral SIM experiment. Next, we illustrate our optical setups for wide-field FDCD imaging and chiral SIM. Finally, we present the experimental results, discuss the issues that occur in the experimental demonstrations and propose a new experimental setup for the future chiral SIM experiment.

## 6.1 Chiral Sample – Annealed Chiral Polyfluorene Film

### Material – $\pi$-Conjugated Polymers

Conjugated polymers have been vastly investigated due to their unique properties that enable applications in optoelectronics [156–159]. Apart from the ordinary optical properties, those polymers also show chiroptical responses. We select the thin films that are made of the $\pi$-conjugated polyfluorene, poly[9,9-bis((3S)-3,7-dimethyloctyl)-2,7-fluorene] (**1**, Fig. 6.1(a)), as the chiral sample for the experiments because such a chiral polyfluorene film has been widely investigated by not only spectroscopic means [160–164] but also several imaging methods like direct confocal CD microscopy [33], two-photon CD confocal microscopy [39], and CD-SNOM [65]. Therefore, we can have both the knowledge of the basic optical properties and rough ideas on the spatial distribution of the chiral polyfluorene film from these studies. Besides, this chiral polyfluorene film exhibits strong CD

response after thermal annealing [160, 163]. Such strong chiral light-matter interaction is beneficial to the following chiral imaging experiments.

**Preparation**

The polymer **1** is first dissolved in the chloroform to obtain a solution whose concentration is 10 mg/mL. We then drop the solution onto a glass coverslip and fabricate the thin film of the polymer **1** using the spin-coating method. The total spin time is set to be two minutes and the acceleration is 1500 rpm/s. The thickness of the films varies according to the concentration of the solution and the terminal spin speed. We choose three terminal spin speeds, which are 2000 rpm, 3000 rpm and 4000 rpm, such that we can fabricate three film samples with different thicknesses. Afterwards, the thin film is thermally annealed at 120°C for eight minutes in the ambient environment.

**Properties**

After the spin-coating and annealed process, the chiral polyfluorene films are deposited on the coverslips and look glassy. The absorption spectra of these three film samples are measured by a commercial spectrometer (Lambda 950 UV/VIS Spectrometer, PerkinElmer, USA). The absorption peaks are located around 380 nm and the absorption at 400 nm is around 80% (Fig. 6.1(b)). Therefore, a 405 nm continuous wave laser source is suitable for exciting the annealed chiral polyfluorene film.
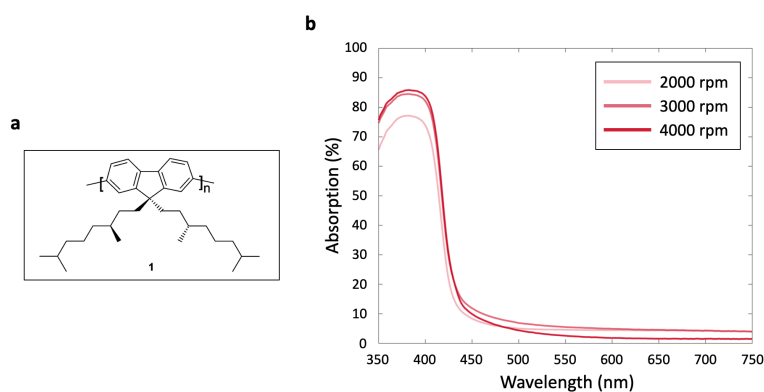


**Figure 6.1:** (a) Molecular structure of the $\pi$-conjugated polymers, poly[9,9-bis((3S)-3,7-dimethyloctyl)-2,7-fluorene] (**1**). (b) Absorption spectrum of the annealed chiral polyfluorene films.

## 6.2 Direct FDCD Imaging

We first use a rather simple optical setup, i.e. a wide-field microscope incorporated with circular polarization illumination, to inspect the FDCD of the annealed chiral polyfluorene films. This wide-field imaging setup is designed in a way that after being converted into CPL, the excitation light does not pass through any optical components and directly reaches the film sample prepared on a coverslip. Such a design avoids disturbing the circular polarization before the excitation light arrives at the sample and thus reduces spurious signals during the image acquisition. The images acquired upon the illumination of LCPL and RCPL are later subtracted one from the other to obtain the FDCD image. Further details and the experimental results are discussed in the following sections.

### 6.2.1 Optical Setup and Experiment

We depict the optical setup used for the wide-field FDCD imaging in Fig. 6.2. A 405 nm diode laser (LuxX+ 405-120, Omicron, Germany) is selected because the wavelength of the laser source fits the absorption bandwidth of the film samples. The laser beam coming out from the optical fiber is collimated by an achromatic doublet lens $L_1$ (AC254-060-A-ML, focal length = 60 mm, Thorlabs, USA). This collimated beam is then relayed by a 4f system, which is composed of a pair of achromatic doublet lenses $L_2$ (AC254-400-A-ML, focal length = 400 mm) and $L_3$ (AC254-050-A-ML, focal length = 50 mm, Thorlabs, USA) and the beam size is demagnified by the 4f system to increase the laser intensity on the sample. To generate CPL, the polarization state of the laser beam is first cleaned up by a linear polarizer $P$ (High contrast glass linear polarizer, Edmund Optics, UK) and then converted into circular polarization by a liquid crystal variable retarder (LCVR; LCC1423-A, Thorlabs, USA). The LCVR consists of liquid crystal molecules that rotate according to the applied voltage sent from the liquid crystal controller (LCC25, Thorlabs, USA). By varying this applied voltage, the LCVR functions as a variable wave plate such that we can actively control the phase retardation of the laser beam and generate both LCPL and RCPL. After the LCVR, we avoid using an objective as a condenser lens in order to let the beam directly illuminate the sample. This should effectively prevent the circular polarization of the incident beam from being distorted before the beam arrives at the sample. The fluorescence that emanates from the chiral sample is collected by an objective (MPlanApo, 60x/NA = 0.9 Air, Olympus, Japan) and then is imaged on an sCMOS camera (Zyla 4.2, Andor, UK) by a tube lens TL (AC508-250-A1-ML, focal
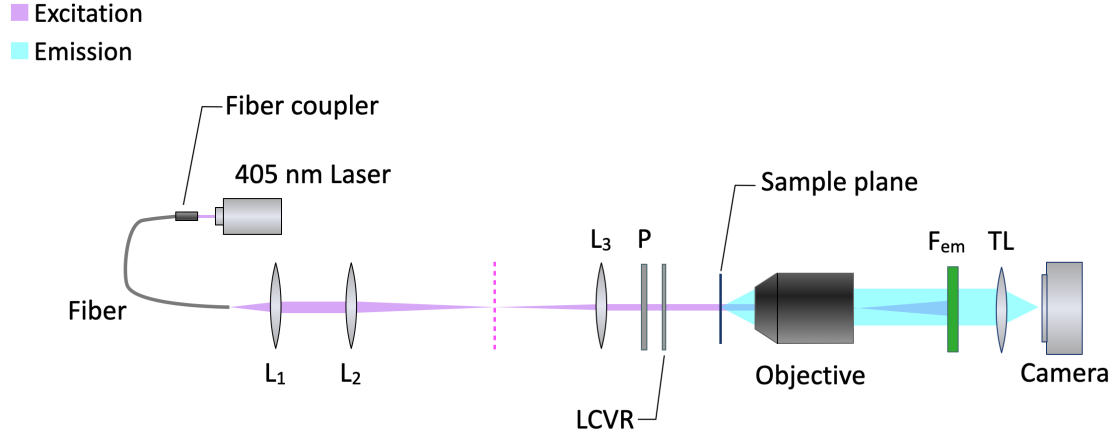
**Figure 6.2:** Schematics of the optical setup for direct wide-field FDCD imaging. The laser beam coming from the optical fiber is first collimated by $L_1$ (focal length = 60 mm) and is demagnified by a 4f system comprised of $L_2$ (focal length = 400 mm) and $L_3$ (focal length = 50 mm). Then, the collimated beam is cleaned up by a linear polarizer $P$ and converted into CPL by the liquid crystal variable retarder (LCVR) and reaches the sample plane. The fluorescence emitted from the sample is collected by an objective, cleaned up by an emission filter $F_{em}$, and imaged on an sCMOS camera by a tube lens TL (focal length = 250 mm). The magenta dashed line indicates an intermediate image plane.

length = 250 mm, Thorlabs, USA). The unwanted excitation light is cleaned up by an emission filter $F_{em}$ (NF405-13, Thorlabs, USA). Eventually, two fluorescence images are recorded upon the excitation of LCPL and RCPL for generating one single FDCD image.

To examine the circular polarization state of the laser beam, we use a portable polarimeter (PAX1000VIS/M, Thorlabs, USA) to measure the Stokes parameters of the beam. Before performing the wide-field FDCD imaging, this polarimeter is placed after the LCVR to receive the laser beam (Fig. 6.3). The ellipticity of the beam is then dynamically monitored such that we can tune the applied voltage on the LCVR accordingly to optimize the quality of the circular polarization state. After the calibration, the absolute value of the ellipticity is maintained within the range of 44.5° to 45° (i.e. the ratio of the minor axis to the major axis of the polarization ellipse is about 0.98 to 1) for both LCPL and RCPL, which suggests the incident beam is well circularly polarized.



**Figure 6.3:** Sketch of the usage of the polarimeter. This portable polarimeter is used to measure the Stokes parameters of the incident beam in order to optimize the circular polarization and determine the applied voltage sent from the LCVR controller.

Importantly, those film samples also show fluorescence-detected linear dichroism (FDLD) [39]. This difference in fluorescence upon the excitation of two orthogonal LPL 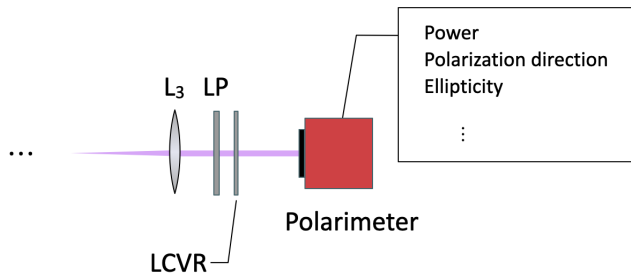may be misinterpreted as the desired FDCD signal. To ensure that the recorded FDCD signal does not originate from the FDLD, we not only calibrate the incident CPL but also present a comparison between the FDCD and FDLD images of the chiral polyfluorene films. We generate the FDLD image by simply placing another linear polarizer after the LCVR to convert the CPL into LPL. When rotating the linear polarizer, we can produce two orthogonal LPL with equal intensity and record the fluorescence images upon the excitation of these two LPL. By subtracting one of the images from the other, we can therefore obtain the FDLD image. If the FDCD and FDLD images are highly correlated, which in principle should not be, the acquired FDCD could be false and be resulted from the FDLD [39].

The images acquired from the measurements are processed in MATLAB and the whole operation is formulated in the following. After the film samples are sequentially illuminated by LCPL and RCPL, we obtain two fluorescence images $M_L(\mathbf{r})$ and $M_R(\mathbf{r})$, respectively. Thus, the FDCD image is generated by subtracting $M_R(\mathbf{r})$ from $M_L(\mathbf{r})$

$$\Delta F_{\text{FDCD}}(\mathbf{r}) = M_L(\mathbf{r}) - M_R(\mathbf{r}). \tag{6.1}$$

On the other hand, after the sample is excited by two orthogonal LPL, which are horizontally and vertically polarized light, successively, we can obtain two images $M_H(\mathbf{r})$ and $M_V(\mathbf{r})$, respectively. The FDLD image can then be calculated by subtracting one of the images from the other:

$$\Delta F_{\text{FDLD}}(\mathbf{r}) = M_V(\mathbf{r}) - M_H(\mathbf{r}). \tag{6.2}$$

### 6.2.2 Results and Discussion

We present the acquired fluorescence images, $M_L(\mathbf{r})$, $M_R(\mathbf{r})$, $M_V(\mathbf{r})$ and $M_H(\mathbf{r})$, and the final FDCD and FDLD images, $\Delta F_{\text{FDCD}}(\mathbf{r})$ and $\Delta F_{\text{FDLD}}(\mathbf{r})$, of the film samples that are fabricated with the spin-speed of 2000, 3000 and 4000 rpm in Fig. 6.4. For each film sample, the fluorescence images are taken at the same location and the FDCD and FDLD images are obtained according to Eqs. 6.1 and 6.2, respectively. The camera exposure time is set to be 500 ms for relatively fast image acquisition.

Particularly, we observe grain distribution in $M_R(\mathbf{r})$ (marked by the yellow arrows in Figs. 6.4(d-f)). Such distribution is distinct from the spatial features observed in $M_L(\mathbf{r})$ (Figs. 6.4(a-c)), which indicates the intensity of the fluorescence emitted from the local area of the film samples is different upon the excitation of RCPL and LCPL. In contrast, the spatial features look similar when the film samples are illuminated by vertically (Figs. 6.4(g-i)) and horizontally polarized light (Figs. 6.4(j-l)), respectively. Still, the film samples are expected to show differential fluorescence upon the excitation of these two types of LPL because, for each film sample, the bright and dark areas shown in $M_V(\mathbf{r})$ and $M_H(\mathbf{r})$ do not coincide (see the areas marked by the yellow rectangles in Figs. 6.4(g-l)). All areas that exhibit differential fluorescence are further identified in $\Delta F_{\mathrm{FDCD}}(\mathbf{r})$ (Figs. 6.4(m-o)) and $\Delta F_{\mathrm{FDLD}}(\mathbf{r})$ (Figs. 6.4(p-r)). In the images of $\Delta F_{\mathrm{FDCD}}(\mathbf{r})$, the blue and white areas indicate different levels of differential fluorescence. In the blue areas, the fluorescence is stronger when the film samples are illuminated by RCPL and the differential fluorescence is insignificant in the white areas. The shape of the domains is similar to what we have seen in $M_R(\mathbf{r})$ (Figs. 6.4(d-f)) and the domain size is around 100 to 200 nm. Because most of the domains exhibit stronger fluorescence upon the excitation of RCPL, the whole images are mainly seen in blue. Such a spatial feature suggests that chiral domains with only one handedness are formed in these three film samples [39]. As for the images of $\Delta F_{\mathrm{FDLD}}(\mathbf{r})$, areas that exhibit differential fluorescence are observed as well. In red (blue) areas, the fluorescence is stronger when the film samples are illuminated by vertically (horizontally) polarized light. Importantly, the spatial features observed in the images of $\Delta F_{\mathrm{FDCD}}(\mathbf{r})$ and $\Delta F_{\mathrm{FDLD}}(\mathbf{r})$ are uncorrelated. The domain size shown in $\Delta F_{\mathrm{FDLD}}(\mathbf{r})$ is approximately 10 µm, which is much larger than that in $\Delta F_{\mathrm{FDCD}}(\mathbf{r})$. Also, the global shape of the domains in the images of $\Delta F_{\mathrm{FDCD}}(\mathbf{r})$ and $\Delta F_{\mathrm{FDLD}}(\mathbf{r})$ do not look alike. Since the spatial domains that show the differential fluorescence in $\Delta F_{\mathrm{FDCD}}(\mathbf{r})$ are distinct from those in $\Delta F_{\mathrm{FDLD}}(\mathbf{r})$, the detected differential fluorescence should not originate from LD and those domains can be recognized as the chiral domains of the films.

In summary, the direct wide-field microscope incorporated with circular and linear polarization illumination is used for FDCD and FDLD imaging. All annealed chiral polyfluorene films show similar spatial features and there is no significant difference among the images of each film sample taken under the same type of excitation. All the film samples exhibit not only the FDCD but also the FDLD signals.
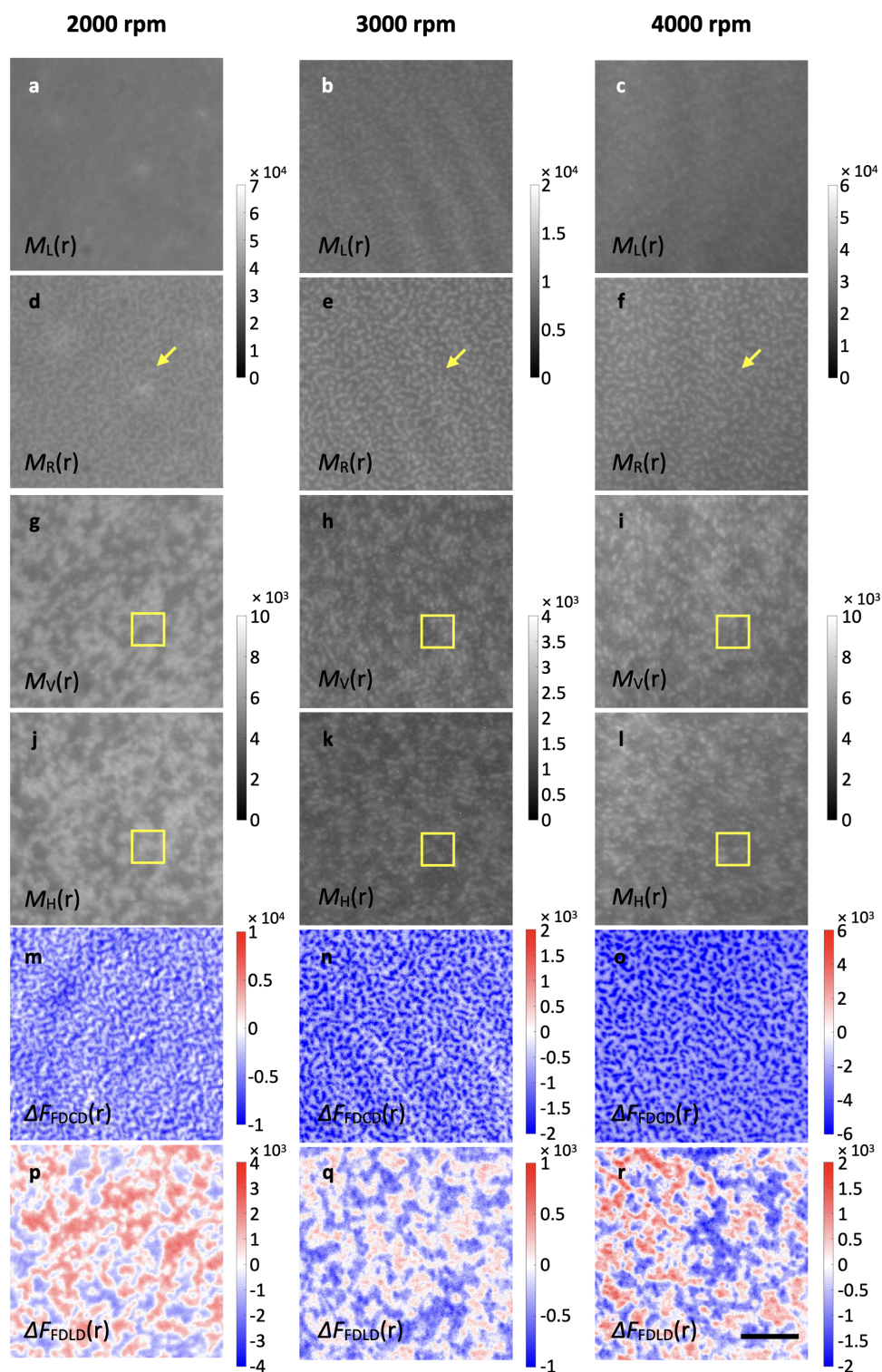
**Figure 6.4:** Acquired fluorescence images, $M_L(\mathbf{r})$, $M_R(\mathbf{r})$, $M_V(\mathbf{r})$ and $M_H(\mathbf{r})$, and the FDCD and FDLD images, $\Delta F_{\mathrm{FDCD}}(\mathbf{r})$ and $\Delta F_{\mathrm{FDLD}}(\mathbf{r})$, of the annealed chiral polyfluorene films fabricated with the spin-speeds 2000 rpm, 3000 rpm and 4000 rpm, respectively. The yellow arrows indicate the characteristic grain distribution when the films are illuminated by RCPL. The areas marked by the yellow rectangles show different fluorescence intensity when the films are illuminated by LCPL and RCPL. The camera exposure time is set to be 500 ms for relatively fast image acquisition. For each film sample, the FDCD image is not the same as the FDLD image, suggesting that the detected differential fluorescence in the FDCD images should not originate from LD. The coloarbars show the photon count (gray) and the differential fluorescence (blue-red), respectively. Scale bar: 10 µm

## 6.3 Chiral SIM Experiment

As discussed in Sec. 4.2, we have suggested two theoretically feasible illumination schemes, namely using *s*- and *p*-polarized light and two CPL of the same handedness, to form the desired structured OC and electric energy density distribution. Here, we select the two-CPL-illumination scheme for the chiral SIM experiment because it is relatively easier to be implemented in practice compared to the other. In typical SIM experiment, the laser beam is commonly split by a diffractive optical element into two main beams. These diffraction beams interfere with each other on the sample plane to form structured excitation patterns [106, 165]. Usually, those diffraction beams are separated by several millimeters. Therefore, it is complicated to manipulate the diffraction beams individually because there is not much space to place optical components for controlling each diffraction beam. On the other hand, it is simpler to implement the experiment if the diffraction beams are managed to be in the same condition. In this sense, applying two CPL illumination is more preferred than *s* and *p*-polarized light illumination in a practical experiment. We slightly modify the fast SIM setup [106, 165] for implementing the chiral SIM experiment. The experimental details will be discussed in the following sections.

### 6.3.1 Optical Setup and Experiment

We depict the optical setup for the chiral SIM experiment in Fig. 6.5. Again, the 405 nm laser (LuxX+ 405-120, Omicron, Germany) is selected as the light source because it fits the absorption of the film samples. An achromatic doublet lens $L_1$ (AC254-060-A-ML, focal length = 60 mm, Thorlabs, USA) is used to collimate the laser beam coming out from the optical fiber. The collimated beam is cleaned up by a linear polarizer $P_0$ (High contrast glass linear polarizer, Edmund Optics, UK) and the direction of the linear polarization is controlled by a half-wave plate (HWP; AHWP10M-600, Thorlabs, USA). A spatial light modulator (SLM; SXGA-3DM, Forth Dimension Displays, UK) is positioned on the intermediate image plane to fast switch the excitation patterns on the sample plane. This SLM displays binary grating images with different pattern phases and orientations on its screen to diffract the incoming light and thus forms the desired $\pm 1^{\text{st}}$ diffraction beams. Totally three pairs of $\pm 1^{\text{st}}$ diffraction beams, which are marked by beam 1 to beam 6 in three orientations (see the inset in Fig. 6.5), are generated when the SLM shows the grating images with three different orientations. To avoid the distortion
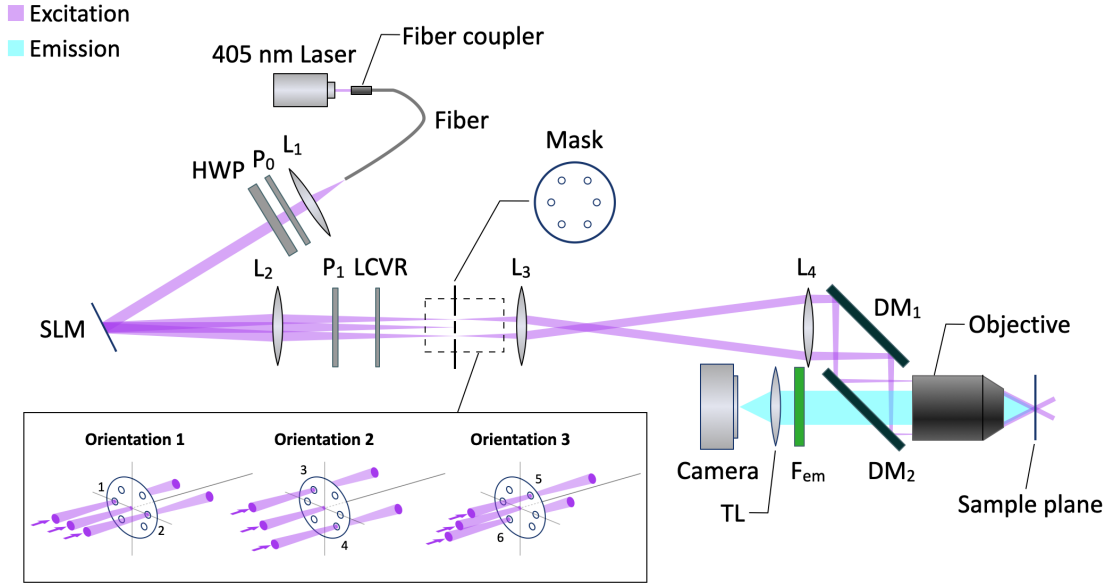
**Figure 6.5:** Schematics of the optical setup for the chiral SIM experiment. The laser beam coming from the optical fiber is first collimated by $L_1$ (focal length = 60 mm) and its polarization state is cleaned up by a linear polarizer $P_0$. The polarization direction of the linearly polarized beam is controlled by a half-wave plate (HWP). Next, the laser beam is diffracted by a spatial light modulator (SLM) into three diffraction beams. To relay the grating images shown on the SLM display, a 4f system comprised of $L_2$ (focal length = 400 mm) and $L_3$ (focal length = 50 mm) is applied. The diffraction beams are cleaned up by a linear polarizer $P_1$ and converted into CPL by the liquid crystal variable retarder (LCVR). Then, the $\pm 1^{\text{st}}$-order diffraction beams are selected by a spatial mask and focused by a lens $L_4$ (focal length = 200 mm) on the back focal plane of an objective to generate the desired structured OC and electric energy density patterns. The fluorescence emitted from the sample is collected by the same objective and cleaned up by an emission filter $F_{\text{em}}$. Finally, the sample fluorescence is imaged on an sCMOS camera by a tube lens TL (focal length = 250 mm). The inset shows the six diffraction beams (marked by beam 1 to 6) generated when the SLM displays the grating images with three different orientations.

of the excitation patterns on the sample plane, the laser beam is incident onto the SLM at a small angle [165]. In our setup, the incident angle is approximately 3°. In addition, because the polarization state of the laser beam incident on the SLM screen affects the reflection efficiency and the polarization states of output diffraction beams, we use the HWP to adjust the direction of the linear polarization such that the intensity and the polarization of the output diffraction beams are optimized. Still, the diffraction efficiency is generally low [165]. In our case, only 3% to 5% of the incident beam is diffracted into the $\pm 1^{\text{st}}$ diffraction beams.

Two achromatic doublet lenses are used to establish a 4f system, which consists of two lenses $L_2$ (AC254-300-A-ML, focal length = 300 mm) and $L_3$ (AC254-250-A-ML, focal length = 250 mm, Thorlabs, USA), in order to relay the grating images onto the sample plane. A spatial mask with six pinholes is placed on the Fourier plane of $L_2$ and acts as a filter to remove the unwanted $0^{\text{th}}$-order diffraction beam as well as other redundant diffraction orders caused by the pixelated SLM screen and the vias (i.e. the

electrical connection between the pixels) of the display pixels [165]. This spatial filtering should thus ensure the sinusoidal excitation patterns of OC and electric energy density patterns with good contrast on the sample plane. Next, the $\pm 1^{\text{st}}$ diffraction beams are reflected by two identical dichroic mirrors $DM_1$ and $DM_2$ (DMLP425, Thorlabs, USA) and focused by a lens $L_4$ (AC254-200-A1-ML, focal length = 200 mm, Thorlabs, USA) on the back focal plane of an objective (MPlanApo, 60x/NA = 0.9 Air, Olympus, Japan). $DM_1$ and $DM_2$ are placed orthogonally in a three-dimensional arrangement such that the phase retardation imposed on the *s*- and *p*-polarization components of the incident beam by $DM_1$ can be in general compensated by $DM_2$ [165].

To generate the desired circular polarized beams, the $\pm 1^{\text{st}}$ diffraction beams are first cleaned up by another linear polarizer $P_1$ (High contrast glass linear polarizer, Edmund Optics, UK) and then pass through the LCVR (LCC1423-A, Thorlabs, USA). Similar to the implementation in the wide-field FDCD imaging setup (Sec. 6.2.1), the linear polarization is transformed into circular polarization by tuning the applied voltage on the LCVR. The polarization states of the $0^{\text{th}}$ and $\pm 1^{\text{st}}$-order diffraction beams are different after the laser beam is diffracted by the SLM. Therefore, we perform the calibration of the circular polarization based on the polarization state of the $\pm 1^{\text{st}}$-order diffraction beams rather than that of the $0^{\text{th}}$-order one. To determine the applied voltage on the LCVR, we place the portable polarimeter after $DM_2$ and dynamically monitor the ellipticity of the $+1^{\text{st}}$-order diffraction beam in orientation 1, i.e. beam 1 shown in the inset in Fig. 6.5 (Fig. 6.6). Although these two orthogonally-arranged dichroic mirrors still introduce anonymous phase retardation, by rotating the LCVR and changing the applied voltage simultaneously, we can optimize the ellipticity of the diffraction beam and then determine the applied voltages that generate good LCPL and RCPL. After the calibration, the ellipticity of the $\pm 1^{\text{st}}$-order diffraction beams can achieve around 44.8° and two collimated circularly polarized plane waves should then, in principle, come out from the objective. Next, the fluorescence emitted from the sample is collected by the same objective and then passes through $DM_2$. The unwanted excitation light is cleaned up by an emission filter ($F_{\text{em}}$, NF405-13, Thorlabs, USA). Eventually, the fluorescence is focused on the sCMOS camera (Zyla 4.2, Andor, UK) by a tube lens TL (AC508-250-A1-ML, focal length = 250 mm, Thorlabs, USA) and we can obtain the subimages of the sample under the illumination of two LCPL and two RCPL, respectively. Based on Eq. 4.42, we should be able to generate the processed images that are suitable for the chiral SIM image reconstruction.
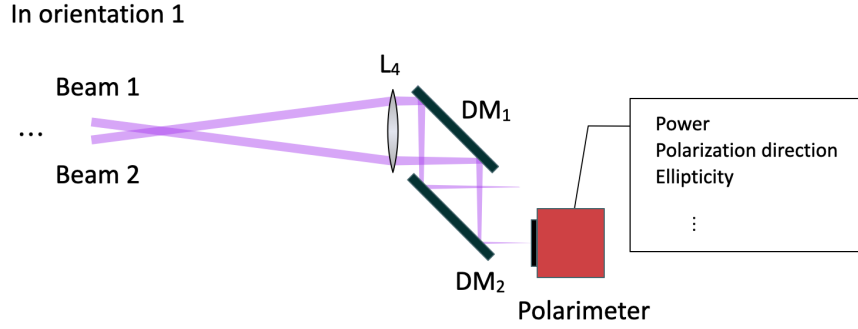
**Figure 6.6:** Sketch of the usage of polarimeter in the chiral SIM experiment. This portable polarimeter is used to measure the Stokes parameters of the +1-order diffraction beam to optimize the circular polarization and determine the applied voltage sent from the LCVR controller.

### 6.3.2 Results and Discussion

We present the fluorescence images acquired when the film sample is illuminated by two $\pm 1^{\text{st}}$ diffraction beams in three different orientations, the corresponding differential images and the Fourier transform of the differential images in Fig. 6.7. The fluorescence images $M_+(\mathbf{r})$ (Figs. 6.7(a-c)) and $M_-(\mathbf{r})$ (Figs. 6.7(d-f)) are taken when the two $\pm 1^{\text{st}}$ diffraction beams are converted into LCPL and RCPL, respectively. The differential images $M(\mathbf{r})$ (Figs. 6.7(g-i)), namely the subimages for the chiral SIM image reconstruction, are generated according to Eq. 4.42 and are processed to obtain the corresponding Fourier transform $\bar{M}(\mathbf{k})$ (Figs. 6.7(j-l)). Because the three film samples have shown similar chiral domain distribution in the wide-field FDCD images (Figs. 6.4(m-o)), here we only record the images of the one fabricated with the spin-speed of 2000 rpm for simplicity. All fluorescence images are acquired at the same position of the film sample and the camera exposure time is set to be 500 ms for relatively fast image acquisition.

The spatial features in $M_+(\mathbf{r})$ look different from that in $M_-(\mathbf{r})$, which suggests the film sample demonstrates differential fluorescence when it is under the illumination of two left- and right-circularly polarized diffraction beams. The characteristic grain distribution, which has been found in Fig. 6.4(d), can be vaguely observed as the film sample is illuminated by two right-circularly polarized diffraction beams. However, the spatial features shown in $M_+(\mathbf{r})$ and $M_-(\mathbf{r})$ vary when the orientation of the $\pm 1^{\text{st}}$ diffraction beams alters from 1 to 3 (see the area marked by the yellow rectangles in Figs. 6.7(a-f)). Such a phenomenon indicates the recorded optical responses from the same local area of the film change when the two $\pm 1^{\text{st}}$ diffraction beams illuminate the sample in different orientations. Accordingly, the spatial features and the chirality of the local domains observed in the $M(\mathbf{r})$ change (see the area marked by the magenta rectangles

in Figs. 6.7(g-i)) such that we cannot determine the chiroptical properties of the local domains. Meanwhile, we do not observe any stripes or structured patterns in $M(\mathbf{r})$. This unfortunately means that the high spatial frequency information on the chiral domains is not down-modulated and captured by the optical imaging system. Such a conclusion can also be confirmed by the corresponding Fourier transform $\bar{M}(\mathbf{k})$ because there are no two additional peaks, which implies the desired high-frequency down-modulation, near the central peak in the images of the corresponding Fourier transform. As a result,
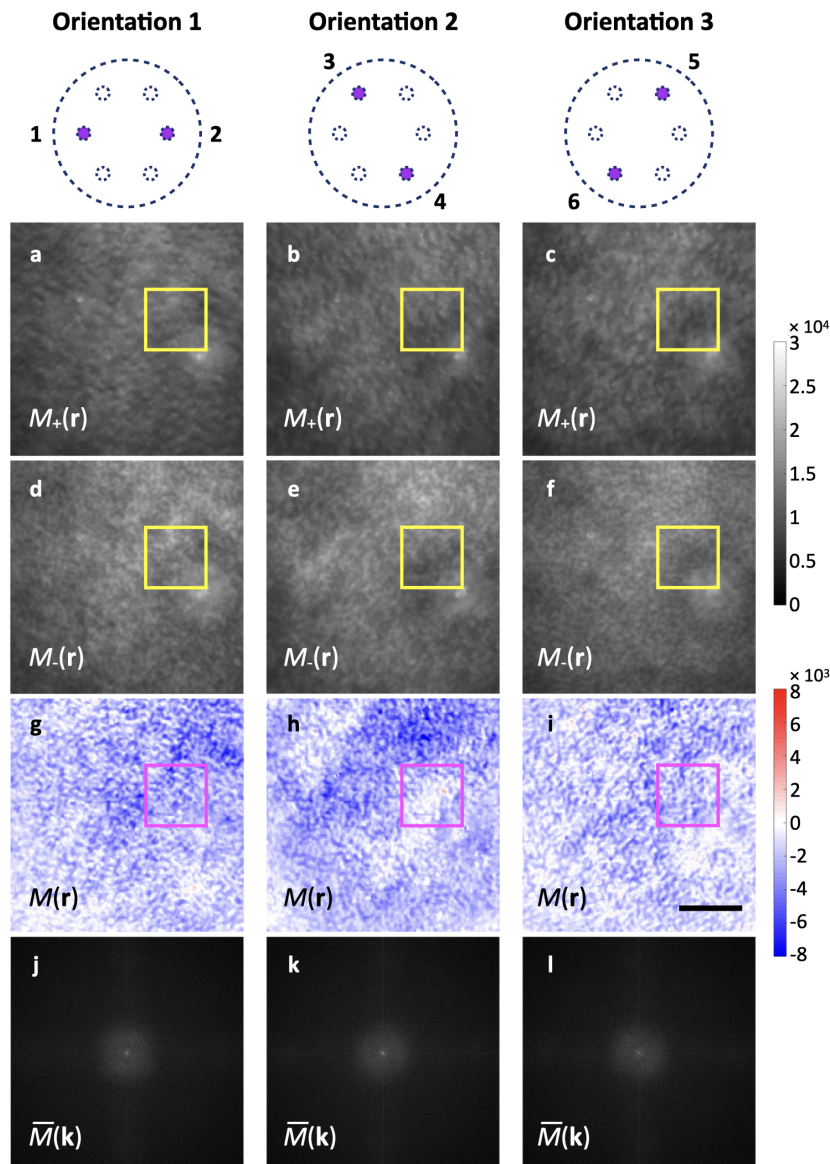


**Figure 6.7:** The fluorescence images of the film fabricated with the spin-speed of 2000 rpm $M_{\pm}(\mathbf{r})$, processed image $M(\mathbf{r})$ and the corresponding Fourier transform $\bar{M}(\mathbf{k})$ acquired under the excitation patterns with orientation 1 to 3. The rectangles are used to mark the spatial features within. Those images are taken at the same position of the film sample. The camera exposure time is set to be 500 ms for relatively fast image acquisition. The coloarbars show the photon count (gray) and the differential fluorescence (blue-red), respectively. Scale bar: 10 µm.
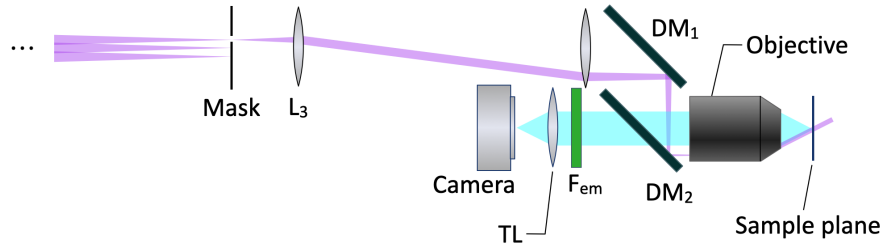
**Figure 6.8:** Schematics of the single-beam illumination scheme in the chiral SIM setup. In this scheme, only one single diffraction beam selected by the spatial mask that has only one pinhole eventually reaches the sample.

those differential images $M(\mathbf{r})$ cannot be further processed by the chiral SIM image reconstruction and generate the super-resolved chiral domain image.

We also record the fluorescence images when the film sample is illuminated by the diffraction beams individually to inspect the condition of the six diffraction beams. To achieve this single-beam illumination scheme, another spatial mask that has only one pinhole is used to select the desired diffraction beams sequentially (Fig. 6.8). Similarly, this single diffraction beam is converted into LCPL or RCPL, depending on the applied voltage on the LCVR and how we rotate the LCVR, and obliquely incident on the film sample. We present the fluorescence images acquired with this single-beam illumination scheme and the corresponding FDCD images in Fig. 6.9. The fluorescence images $M'_L(\mathbf{r})$ (Figs. 6.9(a-f)) and $M'_R(\mathbf{r})$ (Figs. 6.9(g-l)) are taken when the single diffraction beam is converted into LCPL and RCPL, respectively. The FDCD images $\Delta F'_{\mathrm{FDCD}}(\mathbf{r})$ (Figs. 6.9(m-r)) are generated based on Eq. 6.1. Here, the prime $'$ in the superscript differentiates the images acquired with this single-beam illumination scheme from those obtained previously in the wide-field FDCD imaging method. As usual, all fluorescence images are acquired at the same position of the film sample and the camera exposure time is set to be 500 ms for relatively fast image acquisition.

The spatial features found in $M'_L(\mathbf{r})$ look different from that in $M'_R(\mathbf{r})$, which indicates that the film sample demonstrates the differential fluorescence under the illumination of single left- and right-circularly polarized diffraction beam. In the images of $M'_R(\mathbf{r})$, we also vaguely observe the characteristic grain distribution (marked by the yellow arrows in Figs. 6.9(g-l)). Nevertheless, the spatial features shown in the images of $\Delta F'_{\mathrm{FDCD}}(\mathbf{r})$ are dissimilar to what we have observed in $\Delta F_{\mathrm{FDCD}}(\mathbf{r})$ (Fig. 6.4(m)). The spatial features and the chirality of the domains observed in $\Delta F'_{\mathrm{FDCD}}(\mathbf{r})$ also alter
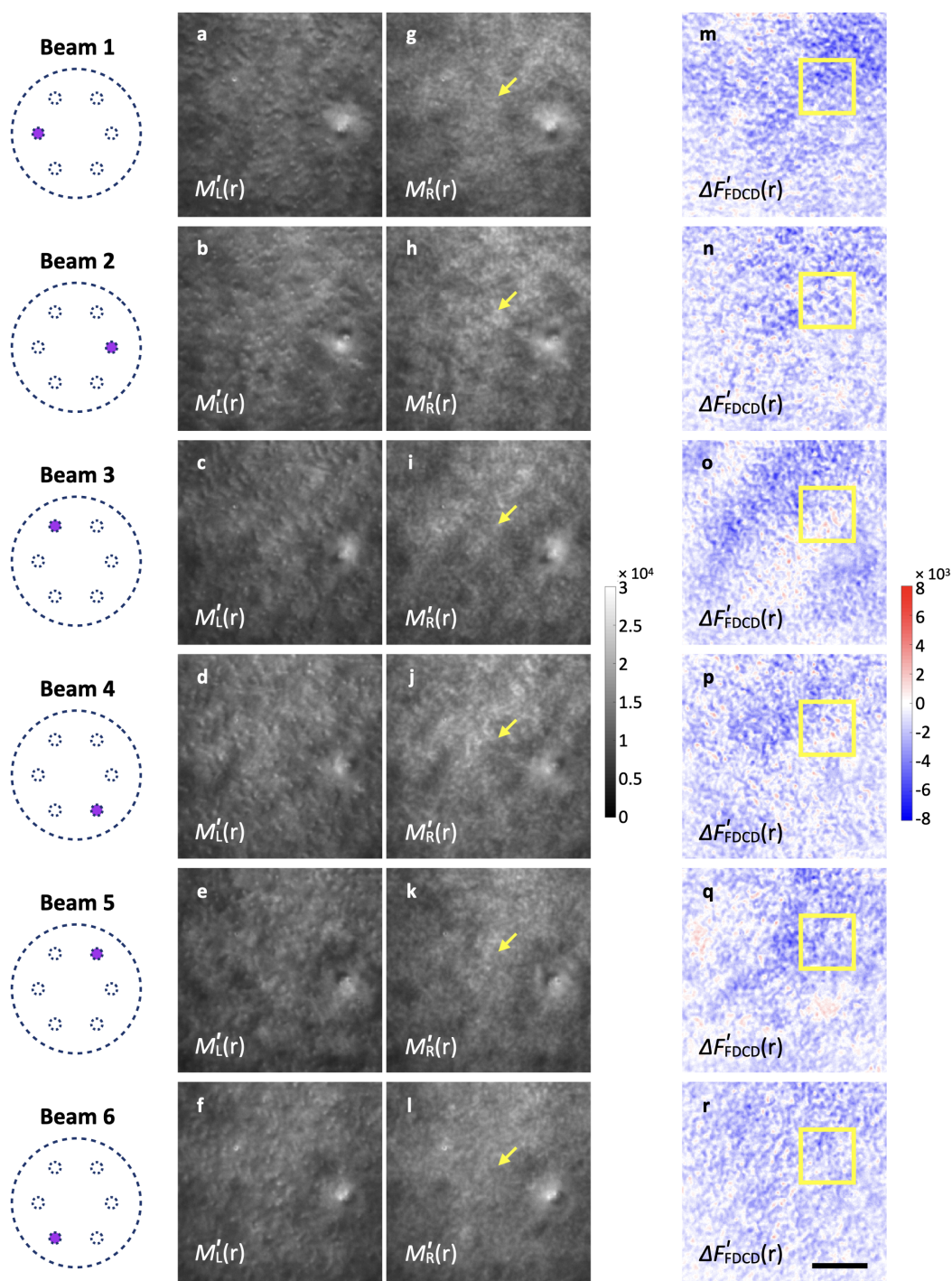
**Figure 6.9:** The fluorescence images $M'_L(\mathbf{r})$ and $M'_R(\mathbf{r})$ and corresponding FDCD images $\Delta F'_{\mathrm{FDCD}}(\mathbf{r})$ of the film sample fabricated with the spin-speed of 2000 rpm. Those fluorescence images are taken under the excitation of beam 1 to 6 and at the same position of the film sample, respectively. The yellow arrows mark the characteristic grain distribution when the film is illuminated by a single right-circularly polarized diffraction beam. The yellow rectangles emphasize that the spatial features and the chirality of the domains within alter as different diffraction beams illuminate the film individually. The camera exposure time is set to be 500 ms for relatively fast image acquisition. The coloarbars show the photon count (grayscale) and the differential fluorescence (blue-red), respectively. Scale bar: 10 μm.

when different single diffraction beams illuminate the sample one at a time (see the area marked by the yellow rectangles in Figs. 6.9(m-r)).

One possible reason that leads to the results shown in Figs. 6.7 and 6.9 could be that the circular polarization of the six diffraction beams has been distorted before these beams arrive at the sample. Such distortion could most likely arise from the objective because it is a sophisticated optical element that consists of multiple lenses. When the diffraction beams traverse the lenses inside the objective, the circular polarization of the beams could be disturbed significantly [166]. Since the polarization state of each diffraction beam could be affected to different extent, the chiroptical properties of the local domains shown in the differential images change consequently when the film sample is illuminated by the different diffraction beams one at a time, leading to what we have observed in Fig. 6.9. Also, the interference of two diffraction beams in a poor condition of the circular polarization is unable to generate the desired structured illumination with high contrast [103], which may be the reason that we cannot observe any stripe patterns in Fig. 6.7. In addition, this polarization distortion could also be caused by the SLM display, on which the liquid crystals are frequently switched between the on and off state to prevent damage to themselves while the SLM shows different grating images [167]. Such an operation could disturb the polarization state of the diffraction beams. Thus, using SLM may also be a potential problem in the chiral SIM experiment.

To solve those issues and improve the experimental results in the future, we here propose another optical setup for implementing the chiral SIM experiment (Fig. 6.10). Particularly, we do not use the SLM and objective in the illumination part of the imaging system in order to avoid disturbing the circular polarization of the incident beams. In this setup, the laser beam is first collimated by a lens $L$ and its polarization state is cleaned up by a linear polarizer $P_0$. Importantly, we suggest using a 50/50 beam splitter to divide the collimated beam into two because this should avoid fluctuations, which the liquid crystals on the SLM display could arise, in the polarization state of the resulting two beams. After the collimated beams are split, they are guided towards the sample plane individually using two mirrors $M_1$ and $M_2$. To convert the incident beams into two CPL, two sets of the linear polarizer, $P_1$ and $P_2$, and the quarter-wave plate, $QWP_1$ and $QWP_2$, are applied. These polarizers are specifically placed right before the sample plane in order to ensure that the circular polarization is not disturbed by any optical elements after the beams are converted. Next, the fluorescence emanated from the sample is collected by an objective in the detection part of the imaging system. After being cleaned
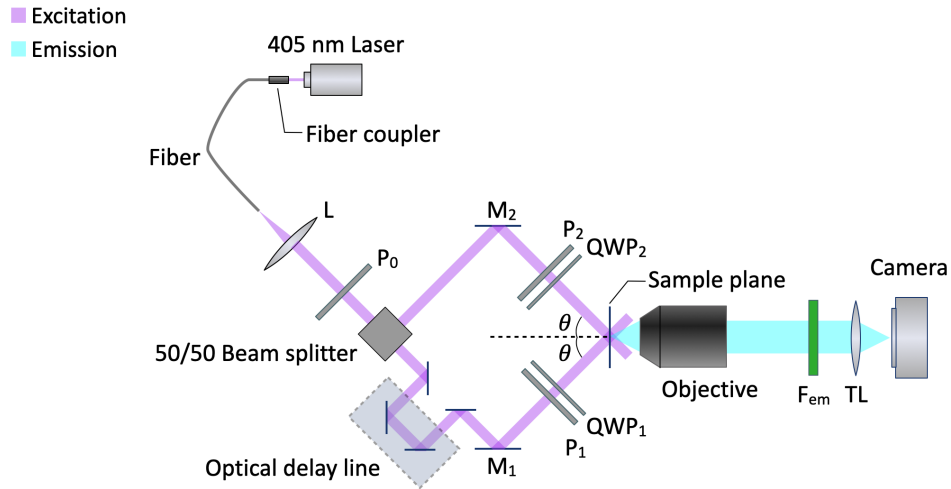
**Figure 6.10:** Schematics of the proposed optical setup for future chiral SIM experiment. Particularly, the SLM and objective are removed in the illumination part of the imaging system to avoid disturbing the polarization state of the beams. The laser beam coming out from the fiber is collimated by a lens $L$. After being cleaned up by a linear polarizer $P_0$, the collimated beam is split by a 50/50 beam splitter and guided towards the sample plane individually using two mirrors $M_1$ and $M_2$ at an angle $\theta$. To convert the incident beams into two CPL, two sets of the linear polarizer, $P_1$ and $P_2$, and the quarter-wave plate, $QWP_1$ and $QWP_2$, are applied. Specifically, those polarizers are placed right before the sample plane to ensure that the circular polarization is not disturbed by any optical elements after the beams are converted. The fluorescence emitted from the sample is collected by an objective. After being cleaned up by an emission filter $F_{em}$, the fluorescence is focused by a tube lens TL and then captured by a camera. The optical delay line is used to change the initial phase of one of the incident beams such that the structured OC patterns can be shifted during the image acquisition.

up by an emission filter $F_{em}$, the fluorescence is focused by a tube lens TL and then captured by a camera. During the image acquisition, we can use, for example, an optical delay line to change the phase of one of the two CPL to shift the structured excitation patterns and thus obtain the subimages for the chiral SIM image reconstruction.

Nevertheless, one should notice that there are still several limitations when working with this proposed setup. The imaging speed of this imaging system could be greatly restricted because the optical delay line in the illumination part of the proposed setup usually has to be operated manually or mechanically to shift different excitation patterns. Besides, the adjustment of these two mirrors $M_1$ and $M_2$, which is crucial because the incident angle of the beams affects the contrast of the excitation patterns, could be complicated in a real experiment. Finally, the resolution improvement may only be achieved in one lateral direction because it is tricky to change the orientation of the excitation patterns, namely rotating the two circularly polarized beams in three-dimensional space, when a beam splitter and mirrors are employed to split the excitation beam into two and guide them towards the sample plane. All of these issues should be carefully considered and managed in future chiral SIM research and experiment.

# Chapter 7

# Summary and Outlook

## 7.1 Summary of the Thesis

This thesis focuses on the development of the chiral SIM method in both theoretical and experimental aspects. We establish the theoretical framework of chiral SIM and analytically investigate possible far-field illumination schemes, based on two-wave interference, for its experimental realization. Essentially, our numerical demonstrations theoretically prove that the chiral SIM method is able to image and discriminate chiral domains at super-resolution. This capability makes chiral SIM a favorable technique to inspect the structural information on various biological samples or sophisticated nanomaterials with much more details. Despite the superior resolving power of chiral SIM, our analysis of noise degradation suggests that using chiral SIM with the proposed far-field illumination scheme to rapidly image natural chiral samples is challenging due to the intrinsically weak chiral light-matter interaction. The small dissymmetry factor of natural chiral samples, which originates from the size mismatch between the molecular structures and the pitch of far-field chiral light (e.g. CPL), leads to low SNR. Thus, the quality of the reconstructed chiral SIM images is usually deficient when this method operates at high imaging speed. Exploiting the superchiral fields formed near plasmonic or dielectric nanostructures could be a promising solution to this issue. Applying such nanostructures in chiral SIM could not only strengthen the chiroptical response of the sample but also enhance the resolving power even further. Still, the nanostructure that can provide the superchiral near fields feasible for the chiral SIM method has, to the best of our knowledge, not yet been discovered. According to our investigations, the main difficulty lies in the fact that the generated superchiral fields cannot enable the essential CD signal decoupling in each switch to generate enough amount of applicable subimages.

In addition, our attempts at the experimental demonstration, where the far-field illumination scheme that employs two CPL is applied, are informative although the generated subimages cannot be applied to the chiral SIM image reconstruction. The

unsatisfactory experimental results could arise from the sophisticated components such as the microscope objective and the SLM in the illumination part of the optical setup because they are very likely to muddle the circular polarization of the incident light and decrease the contrast of the excitation patterns. As a result, the moirè effect is not evident such that the high spatial frequency information cannot be brought into the observable bandwidth of the optical imaging system and restored by the chiral SIM image reconstruction. By excluding these sophisticated components in the illumination part of the optical setup, we propose a new configuration for the future chiral SIM experiment. The incident laser beam is divided into two by a beam splitter and the objective is only used in the detection part for collecting the fluorescence from the sample. In the end, we discuss the limitations of this proposed configuration which should be considered in the future chiral SIM experiment.

## 7.2 Future Work and Perspective

In the final section, we provide suggestions for future work and look forward to new research directions that may advance the development of chiral SIM and help to pave the road towards practical applications in diverse fields.

### Designing Nanostructures and Tailoring Superchiral Near Fields with Artificial Intelligence

As we discussed in Sec. 5.3.1, using plasmonic or dielectric nanostructures could be beneficial to the performance of chiral SIM because the generated superchiral near fields can strengthen the chiral light-matter interaction. Unfortunately, such an idea is still not applicable because we have not yet found the nanostructure that can sufficiently tailor the superchiral near fields to enable the CD signal decoupling. To search for a practical scheme for applying the superchiral near fields in chiral SIM, a further investigation on the design of nanostructures becomes necessary.

However, using conventional simulation techniques, such as FDTD and finite element methods, to design nanostructures and tailor the corresponding near-field distribution relies on designers' intuition, insight and experience. The design task can be very tricky if the existing design library cannot provide a good hint. Besides, adjusting a handful of geometric parameters in the simulation to match expected optical properties and field distribution usually needs numerous cycles of simulations and re-evaluation, which is

thus time-inefficient and computationally expensive. In this sense, simulation techniques based on artificial intelligence are powerful tools for the design task. In particular, the deep learning technique is a data-driven method that needs little human intervention and can approach the target without intuitive reasoning [168, 169]. Thus, it can work much more efficiently compared to these conventional simulation methods after a series of training processes. Apart from many applications in, for example, image analysis [170] and genomics [171], researchers also put their focus on the inverse design of photonic nanostructures using the deep learning neuron networks [172–178]. Very recently, the feasibility of using the deep learning method to inversely design the nanostructure based on a predetermined near-field distribution has been demonstrated [179, 180]. These studies are exciting because they may reveal the possibility of engineering the distribution of superchiral fields by the deep learning method. Useful nanostructures that are very likely outside of our knowledge base may be discovered by the deep learning neuron networks more efficiently. We therefore expect that designing the nanostructures and tailoring the corresponding superchiral near fields with the deep learning model becomes a new sub research domain and, eventually, helps to find out an optimum design of nanostructure applicable to the chiral SIM method.

**Illumination Scheme of Using Superchiral Surface Waves**

Bloch surface waves are electromagnetic waves induced at the interface between the one-dimensional photonic crystal (1DPC) and the surrounding medium [181, 182]. When a well-designed 1DPC structure is illuminated by CPL, the TE and TM modes can be excited coherently, leading to uniform superchiral fields on the top surface [183–185]. We expect the interference of such superchiral surface waves will form one-dimensional periodic OC patterns with giant OC. By changing the initial phase and the handedness of the incident CPL, the pattern phase and the handedness of the generated periodic OC distribution should alter accordingly and the subimages applicable to chiral SIM image reconstruction can be obtained straightforwardly. Overall, using the 1DPC structure as an illumination platform in chiral SIM may not only generate the desired structured illumination patterns but also strengthen the chiroptical responses of the investigated chiral sample owing to the enhanced OC. It could be a means to enhance the performance of chiral SIM and thus deserves further investigation.

**Plasmonic-Enhanced Assembly of Achiral Dyes and Chiral Macromolecules**

When achiral dyes or fluorescent molecules are attached to the macroscopic chiral structure of macromolecules, such as DNA strains and proteins, the whole assembly gives rise to the CD [186–188] and FDCD responses [142, 189] approximately at the wavelengths where the absorption of the individual dye molecules occurs. Furthermore, such CD response can be much enhanced by positioning plasmonic nanoparticles in the proximity of the chiral assemblies [188]. As the CD response of the hybrid systems (i.e. plasmonic nanoparticles combined with the assemblies of achiral dyes and chiral macromolecules) is enhanced, the corresponding FDCD response is expected to be enhanced as well, which makes such systems a suitable sample for the proof-of-concept chiral SIM experiment. In addition, the forenamed studies may disclose the possibility of inspecting many macromolecules of interest via FDCD measurement after fluorescence labeling, and, if necessary, the FDCD signal could be enhanced by binding nanoparticles to the dye-macromolecule assemblies. If such a scheme is feasible, chiral SIM may become a powerful method since it can be applied to investigate the chiral domains of a variety of biological samples that can be fluorescently labeled and exhibit structure-induced FDCD. Thus, a comprehensive investigation on such hybrid systems may be an important research field that benefits the long-term development of chiral SIM.

**Perspectives**

Chiral SIM is a novel approach developed to rapidly image chiral domains of a given sample at super-resolution, and, at the same time, to overcome the challenges that limit the capability of conventional chiral imaging techniques. In general, the strengths of chiral SIM include the high image acquisition rate, the flexibility of applying various illumination schemes or platforms to enhance chiroptical responses, and superior resolving power over diffraction-limited imaging methods. Thus, it has the potential to be advanced further towards a real-time monitoring method to investigate the conformational changes in organic systems of interest or towards three-dimensional imaging that helps the study the structural information on vital macromolecules. Ultimately, applications of chiral SIM may involve diagnosis or pathological analysis. For instance, we may be able to detect and analyze the unusual structural deformation of proteins, which participate in the appearance of neurodegenerative and neuropsychiatric disorders such as Alzheimer's and Parkinson's diseases, in a real-time manner with images or videos at super-resolution.

# Bibliography

1. Kelvin, W. T. B. *The molecular tactics of a crystal* (Clarendon Press, 1894).

2. Franks, M. E., Macpherson, G. R. & Figg, W. D. Thalidomide. *The Lancet* **363,** 1802–1811 (2004).

3. Greenfield, N. J. Using circular dichroism spectra to estimate protein secondary structure. *Nat. Protoc.* **1,** 2876 (2006).

4. Miles, A. J. & Wallace, B. A. Circular dichroism spectroscopy of membrane proteins. *Chem. Soc. Rev.* **45,** 4859–4872 (2016).

5. Barron, L. D. *Molecular light scattering and optical activity* (Cambridge University Press, 2009).

6. Collins, J. T., Kuppe, C., Hooper, D. C., Sibilia, C., Centini, M. & Valev, V. K. Chirality and chiroptical effects in metal nanostructures: fundamentals and current trends. *Advanced Optical Materials* **5,** 1700182 (2017).

7. Arago, D. Sur une modification remarquable qu'éprouvent les rayons lumineux dans leur passage à travers certains corps diaphanes, et sur quelques autres nouveaux phénomènes d'optique. *Mem. Inst.* **1,** 93–134 (1811).

8. Biot, J.-B. Mémoire sur un nouveau genre d'oscillations que les molécules de la lumiére éprouvent, en traversant certains cristaux. *Mem. Inst.* **1,** 1–372 (1812).

9. Haidinger, W. Üeber den Pleochroismus des Amethysts. *Ann. Phys.* **146,** 531–544 (1847).

10. Cotton, A. Absorption inégale des rayons circulaires droit et gauche dans certains corps actifs. *Compt. Rend.* **120,** 989–991 (1895).

11. Barriel, O. A. *Mueller matrix polarimetry of anisotropic chiral media* PhD thesis (Universitat de Barcelona, 2010).

12. Tang, Y. *Chirality of light and its interaction with chiral matter* PhD thesis (Harvard University, 2013).

13. Fresnel, A. Extrait d'un Meémoire sur la double réfraction pariculiére que présente le cristal de roche dans la direction de son axe. *Ann. Chim. Phys.* **28,** 147–161 (1825).

14. Kuhn, W. Optical rotatory power. *Ann. Rev. Phys. Chem.* **9,** 417–438 (1958).

15. Barron, L. D. & Buckingham, A. D. Vibrational optical activity. *Chem. Phys. Lett.* **492,** 199–213 (2010).

16. Tang, Y. & Cohen, A. E. Optical chirality and its interaction with matter. *Phys. Rev. Lett.* **104,** 163901 (2010).

17. Turner, D. H., Tinoco Jr, I. & Maestre, M. Fluorescence detected circular dichroism. *J. Am. Chem. Soc.* **96,** 4340–4342 (1974).

18. Tinoco Jr, I. & Turner, D. H. Fluorescence detected circular dichroism. Theory. *J. Am. Chem. Soc.* **98,** 6453–6456 (1976).

19. Tanaka, K., Pescitelli, G., Nakanishi, K. & Berova, N. Fluorescence detected exciton coupled circular dichroism: development of new fluorescent reporter groups for structural studies. *Monatsh. Chem.* **136,** 367–395 (2005).

20. Ehrenberg, B. & Steinberg, I. Effect of photoselection on fluorescence-detected circular dichroism. *J. Am. Chem. Soc.* **98,** 1293–1295 (1976).

21. Karunakaran, S. C., Cafferty, B. J., Weigert-MuÇoz, A., Schuster, G. B. & Hud, N. V. Spontaneous symmetry breaking in the formation of supramolecular polymers: implications for the origin of biological homochirality. *Angew. Chem.* **58,** 1453–1457 (2019).

22. Zinna, F., Resta, C., Górecki, M., Pescitelli, G., Di Bari, L., Jávorfi, T., Hussain, R. & Siligardi, G. Circular dichroism imaging: mapping the local supramolecular order in thin films of chiral functional polymers. *Macromolecules* **50,** 2054–2060 (2017).

23. Albano, G., Górecki, M., Pescitelli, G., Di Bari, L., Jávorfi, T., Hussain, R. & Siligardi, G. Electronic circular dichroism imaging (CD i) maps local aggregation modes in thin films of chiral oligothiophenes. *New J. Chem.* **43,** 14584–14593 (2019).

24. Claborn, K., Puklin-Faucher, E., Kurimoto, M., Kaminsky, W. & Kahr, B. Circular dichroism imaging microscopy: application to enantiomorphous twinning in biaxial crystals of 1, 8-dihydroxyanthraquinone. *J. Am. Chem. Soc.* **125,** 14825–14831 (2003).

25. Arteaga, O., El-Hachemi, Z., Canillas, A. & Ribó, J. M. Transmission Mueller matrix ellipsometry of chirality switching phenomena. *Thin Solid Films* **519,** 2617–2623 (2011).

26. Arteaga, O. & Kuntman, E. *Beyond polarization microscopy: Mueller matrix microscopy with frequency demodulation* in *Polarization: Measurement, Analysis, and Remote Sensing XI* **9099** (2014), 90990R.

27. Marongiu, R., Le Gratiet, A., Pesce, L., Bianchini, P. & Diaspro, A. ExCIDS: a combined approach coupling Expansion Microscopy (ExM) and Circular Intensity Differential Scattering (CIDS) for chromatin-DNA imaging. *OSA Continuum* **3,** 1770–1780 (2020).

28. Kaminsky, W., Claborn, K. & Kahr, B. Polarimetric imaging of crystals. *Chem. Soc. Rev.* **33,** 514–525 (2004).

29. Arteaga, O., Freudenthal, J., Wang, B. & Kahr, B. Mueller matrix polarimetry with four photoelastic modulators: theory and calibration. *Appl. Opt.* **51,** 6805–6817 (2012).

30. Arteaga, O., Baldrís, M., Antó, J., Canillas, A., Pascual, E. & Bertran, E. Mueller matrix microscope with a dual continuous rotating compensator setup and digital demodulation. *Appl. Opt.* **53,** 2236–2245 (2014).

31. Arteaga, O., Kuntman, E., Antó, J., Pascual, E., Canillas, A. & Bertran, E. Mueller matrix microscopy on a Morpho butterfly. *Bioinspir. Biomim.* **11,** 016006 (2015).

32. Le Gratiet, A., Pesce, L., Oneto, M., Marongiu, R., Zanini, G., Bianchini, P. & Diaspro, A. Circular intensity differential scattering (CIDS) scanning microscopy to image chromatin-DNA nuclear organization. *OSA Continuum* **1,** 1068–1078 (2018).

33. Savoini, M., Biagioni, P., Meskers, S. C., Duo, L., Hecht, B. & Finazzi, M. Spontaneous formation of left-and right-handed cholesterically ordered domains in an enantiopure chiral polyfluorene film. *J. Phys. Chem. Lett.* **2,** 1359–1362 (2011).

34. Yamada, T., Eguchi, T., Wakiyama, T., Narushima, T., Okamoto, H. & Kimizuka, N. Synthesis of Chiral Labtb and Visualization of Its Enantiomeric Excess by Induced Circular Dichroism Imaging. *Chem. Eur. J.* **25,** 6698–6702 (2019).

35. Narushima, T. & Okamoto, H. Circular dichroism microscopy free from commingling linear dichroism via discretely modulated circular polarization. *Sci. Rep.* **6,** 35731 (2016).

36. Vinegrad, E., Vestler, D., Ben-Moshe, A., Barnea, A. R., Markovich, G. & Cheshnovsky, O. Circular dichroism of single particles. *ACS Photonics* **5,** 2151–2159 (2018).

37. Helmchen, F. & Denk, W. Deep tissue two-photon microscopy. *Nat. Methods* **2,** 932–940 (2005).

38. Lefort, C. A review of biomedical multiphoton microscopy and its laser sources. *J. Phys. D: Appl. Phys.* **50,** 423001 (2017).

39. Savoini, M., Wu, X., Celebrano, M., Ziegler, J., Biagioni, P., Meskers, S. C., Duò, L., Hecht, B. & Finazzi, M. Circular dichroism probed by two-photon fluorescence microscopy in enantiopure chiral polyfluorene thin films. *J. Am. Chem. Soc.* **134,** 5832–5835 (2012).

40. Chen, X., Nadiarynkh, O., Plotnikov, S. & Campagnola, P. J. Second harmonic generation microscopy for quantitative analysis of collagen fibrillar structure. *Nat. Protoc.* **7,** 654–669 (2012).

41. Mazumder, N., Qiu, J., Foreman, M. R., Romero, C. M., Hu, C.-W., Tsai, H.-R., Török, P. & Kao, F.-J. Polarization-resolved second harmonic generation microscopy with a four-channel Stokes-polarimeter. *Opt. Express* **20,** 14090–14099 (2012).

42. Lee, H., Huttunen, M. J., Hsu, K.-J., Partanen, M., Zhuo, G.-Y., Kauranen, M. & Chu, S.-W. Chiral imaging of collagen by second-harmonic generation circular dichroism. *Biomed. Opt. Express* **4,** 909–916 (2013).

43. Zhuo, G.-Y., Lee, H., HSU, K.-J., Huttunen, M., Kauranen, M., Lin, Y.-Y. & Chu, S.-W. Three-dimensional structural imaging of starch granules by second-harmonic generation circular dichroism. *J. Microsc.* **253,** 183–190 (2014).

44. Rodrigues, S. P., Lan, S., Kang, L., Cui, Y. & Cai, W. Nonlinear imaging and spectroscopy of chiral metamaterials. *Adv. Mater.* **26,** 6157–6162 (2014).

45. Campbell, K. R. & Campagnola, P. J. Wavelength-dependent second harmonic generation circular dichroism for differentiation of Col I and Col III isoforms in stromal models of ovarian cancer based on intrinsic chirality differences. *J. Phys. Chem. B* **121,** 1749–1757 (2017).

46. Chen, M.-Y., Huttunen, M., Kan, C.-W., Deka, G., Lin, Y.-Y., Ye, C.-W., Wu, M.-J., Liu, H.-L. & Chu, S.-W. Resonant nonlinear microscopy reveals changes in molecular level chirality in native biological tissues. *Opt. Commun.* **422,** 56–63 (2018).

47. Schmeltz, M., Teulon, C., Latour, G., Ghoubay, D., Borderie, V., Aimé, C. & Schanne-Klein, M.-C. Implementation of artifact-free circular dichroism SHG imaging of collagen. *Opt. Express* **27,** 22685–22699 (2019).

48. Byers, J., Yee, H., Petralli-Mallow, T. & Hicks, J. Second-harmonic generation circular-dichroism spectroscopy from chiral monolayers. *Phys. Rev. B* **49,** 14643 (1994).

49. Terazima, M., Hirota, N., Braslavsky, S. E., Mandelis, A., Bialkowski, S. E., Diebold, G. J., Miller, R., Fournier, D., Palmer, R. A. & Tam, A. Quantities, terminology, and symbols in photothermal and related spectroscopies (IUPAC Recommendations 2004). *Pure Appl. Chem.* **76,** 1083–1118 (2004).

50. Bialkowski, S. E., Astrath, N. G. & Proskurnin, M. A. *Photothermal Spectroscopy Methods* (John Wiley & Sons, 2019).

51. Kitamori, T. Thermal lens microscope and microchip chemistry. *Bull. Chem. Soc. Jpn.* **92,** 469–473 (2019).

52. Uchiyama, K., Hibara, A., Kimura, H., Sawada, T. & Kitamori, T. Thermal lens microscope. *Jpn. J. Appl. Phys.* **39,** 5316 (2000).

53. Dada, O. O., Feist, P. E. & Dovichi, N. J. Thermal diffusivity imaging with the thermal lens microscope. *Appl. Opt.* **50,** 6336–6342 (2011).

54. Proskurnin, M., Volkov, D., Gor'kova, T., Bendrysheva, S., Smirnova, A. & Nedosekin, D. Advances in thermal lens spectrometry. *J. Anal. Chem.* **70,** 249–276 (2015).

55. Berciaud, S., Lasne, D., Blab, G. A., Cognet, L. & Lounis, B. Photothermal heterodyne imaging of individual metallic nanoparticles: Theory versus experiment. *Phys. Rev. B* **73,** 045424 (2006).

56. Berciaud, S., Cognet, L., Blab, G. A. & Lounis, B. Photothermal heterodyne imaging of individual nonfluorescent nanoclusters and nanocrystals. *Phys. Rev. Lett.* **93,** 257402 (2004).

57. Gaiduk, A., Yorulmaz, M., Ruijgrok, P. & Orrit, M. Room-temperature detection of a single molecule's absorption by photothermal contrast. *Science* **330,** 353–356 (2010).

58. Yamauchi, M., Mawatari, K., Hibara, A., Tokeshi, M. & Kitamori, T. Circular dichroism thermal lens microscope for sensitive chiral analysis on microchip. *Anal. Chem.* **78,** 2646–2650 (2006).

59. Mawatari, K., Kubota, S. & Kitamori, T. Circular dichroism thermal lens microscope in the UV wavelength region (UV-CD-TLM) for chiral analysis on a microchip. *Anal. Bioanal. Chem.* **391,** 2521–2526 (2008).

60. Spaeth, P., Adhikari, S., Le, L., Jollans, T., Pud, S., Albrecht, W., Bauer, T., Caldarola, M., Kuipers, L. & Orrit, M. Circular dichroism measurement of single metal nanoparticles using photothermal imaging. *Nano Lett.* **19,** 8934–8940 (2019).

61. Narushima, T. & Okamoto, H. Circular dichroism nano-imaging of two-dimensional chiral metal nanostructures. *Phys. Chem. Chem. Phys.* **15,** 13805–13809 (2013).

62. Narushima, T. & Okamoto, H. Strong nanoscale optical activity localized in two-dimensional chiral metal nanostructures. *J. Phys. Chem. C* **117,** 23964–23969 (2013).

63. Hashiyada, S., Narushima, T. & Okamoto, H. Local optical activity in achiral two-dimensional gold nanostructures. *J. Phys. Chem. C* **118,** 22229–22233 (2014).

64. Nishiyama, Y. & Okamoto, H. Near-field nonlinear CD imaging of single gold nanostructures. *J. Phys. Chem. C* **120,** 28157–28162 (2016).

65. Savoini, M., Biagioni, P., Lakhwani, G., Meskers, S., Duo, L. & Finazzi, M. Near-field circular polarization probed by chiral polyfluorene. *Opt. Lett.* **34,** 3571–3573 (2009).

66. Tantussi, F., Fuso, F., Allegrini, M., Micali, N., Occhiuto, I. G., Scolaro, L. M. & Patanè, S. Linear and circular dichroism in porphyrin J-aggregates probed by polarization modulated scanning near-field optical microscopy. *Nanoscale* **6,** 10874–10878 (2014).

67. Heinzelmann, H. & Pohl, D. Scanning near-field optical microscopy. *Appl. Phys. A* **59,** 89–101 (1994).

68. Hecht, B., Sick, B., Wild, U. P., Deckert, V., Zenobi, R., Martin, O. J. & Pohl, D. W. Scanning near-field optical microscopy with aperture probes: Fundamentals and applications. *J. Chem. Phys.* **112,** 7761–7774 (2000).

69. Hartschuh, A. in *Encyclopedia of Nanotechnology* 1878–1878 (Springer Netherlands, Dordrecht, 2012).

70. Hwang, J., Gheber, L. A., Margolis, L. & Edidin, M. Domains in cell plasma membranes investigated by near-field scanning optical microscopy. *Biophys. J.* **74,** 2184–2190 (1998).

71. De Lange, F., Cambi, A., Huijbens, R., de Bakker, B., Rensen, W., Garcia-Parajo, M., van Hulst, N. & Figdor, C. G. Cell biology beyond the diffraction limit: near-field scanning optical microscopy. *J. Cell Sci.* **114,** 4153–4160 (2001).

72. Bulat, K., Rygula, A., Szafraniec, E., Ozaki, Y. & Baranska, M. Live endothelial cells imaged by Scanning Near-field Optical Microscopy (SNOM): capabilities and challenges. *J. Biophotonics* **10,** 928–938 (2017).

73. Zhang, W., Fang, Z. & Zhu, X. Near-field Raman spectroscopy with aperture tips. *Chem. Rev.* **117,** 5095–5109 (2017).

74. Henriques, R., Griffiths, C., Hesper Rego, E. & Mhlanga, M. M. PALM and STORM: unlocking live-cell super-resolution. *Biopolymers* **95,** 322–331 (2011).

75. Leung, B. O. & Chou, K. C. Review of super-resolution fluorescence microscopy for biology. *Appl. Spectrosc.* **65,** 967–980 (2011).

76. Khater, I. M., Nabi, I. R. & Hamarneh, G. A review of super-resolution single-molecule localization microscopy cluster Analysis and quantification methods. *Patterns* **1,** 100038 (2020).

77. Lelek, M., Gyparaki, M. T., Beliu, G., Schueder, F., Griffié, J., Manley, S., Jungmann, R., Sauer, M., Lakadamyali, M. & Zimmer, C. Single-molecule localization microscopy. *Nat. Rev. Dis. Primers* **1,** 1–27 (2021).

78. Müller, T., Schumann, C. & Kraegeloh, A. STED microscopy and its applications: new insights into cellular processes on the nanoscale. *ChemPhysChem* **13,** 1986–2000 (2012).

79. Sednev, M. V., Belov, V. N. & Hell, S. W. Fluorescent dyes with large Stokes shifts for super-resolution optical microscopy of biological objects: a review. *Methods Appl. Fluoresc.* **3,** 042004 (2015).

80. Vicidomini, G., Bianchini, P. & Diaspro, A. STED super-resolved microscopy. *Nat. Methods* **15,** 173–182 (2018).

81. Wildanger, D., Patton, B. R., Schill, H., Marseglia, L., Hadden, J., Knauer, S., Schönle, A., Rarity, J. G., O'Brien, J. L., Hell, S. W., *et al.* Solid Immersion Facilitates Fluorescence Microscopy with Nanometer Resolution and Sub-Ångström Emitter Localization. *Adv. Mater.* **24,** OP309–OP313 (2012).

82. Heintzmann, R. & Huser, T. Super-resolution structured illumination microscopy. *Chem. Rev.* **117,** 13890–13908 (2017).

83. Rego, E. H., Shao, L., Macklin, J. J., Winoto, L., Johansson, G. A., Kamps-Hughes, N., Davidson, M. W. & Gustafsson, M. G. Nonlinear structured-illumination microscopy with a photoswitchable protein reveals cellular structures at 50-nm resolution. *Proc. Natl. Acad. Sci. U.S.A.* **109,** E135–E143 (2012).

84. Wei, F., Lu, D., Shen, H., Wan, W., Ponsetto, J. L., Huang, E. & Liu, Z. Wide field super-resolution surface imaging through plasmonic structured illumination microscopy. *Nano Lett.* **14,** 4634–4639 (2014).

85. Wei, F., Ponsetto, J. L. & Liu, Z. in *Plasmonics and Super-Resolution Imaging* 2531–2536 (Pan Stanford, 2017).

86. Bezryadina, A., Zhao, J., Xia, Y., Zhang, X. & Liu, Z. High spatiotemporal resolution imaging with localized plasmonic structured illumination microscopy. *ACS Nano* **12,** 8248–8254 (2018).

87. Huang, X., Fan, J., Li, L., Liu, H., Wu, R., Wu, Y., Wei, L., Mao, H., Lal, A., Xi, P., *et al.* Fast, long-term, super-resolution imaging with Hessian structured illumination microscopy. *Nat. Biotechnol.* **36,** 451 (2018).

88. Markwirth, A., Lachetta, M., Mönkemöller, V., Heintzmann, R., Hübner, W., Huser, T. & Müller, M. Video-rate multi-color structured illumination microscopy with simultaneous real-time reconstruction. *Nat. Commun.* **10,** 1–11 (2019).

89. Wicker, K. & Heintzmann, R. Single-shot optical sectioning using polarization-coded structured illumination. *J. Opt.* **12,** 084010 (2010).

90. Zhanghao, K., Chen, X., Liu, W., Li, M., Liu, Y., Wang, Y., Luo, S., Wang, X., Shan, C., Xie, H., *et al.* Super-resolution imaging of fluorescent dipoles via polarized structured illumination microscopy. *Nat. Commun.* **10,** 1–10 (2019).

91. Wicker, K. & Heintzmann, R. Resolving a misconception about structured illumination. *Nat. Photonics* **8,** 342–344 (2014).

92. Collett, E. *Field Guide to Polarization* (SPIE Press, 2005).

93. Lipkin, D. M. Existence of a new conservation law in electromagnetic theory. *J. Math. Phys.* **5,** 696–700 (1964).

94.   Schäferling, M. Chiral nanophotonics. *Springer Ser. Opt. Sci.* **205** (2017).

95.   Bliokh, K. Y. & Nori, F. Characterizing optical chirality. *Phys. Rev. A* **83,** 021803 (2011).

96.   Schäferling, M., Yin, X. & Giessen, H. Formation of chiral fields in a symmetric environment. *Opt. Express* **20,** 26326–26336 (2012).

97.   Nienhaus, G. U. & Nienhaus, K. in *Fluorescence Microscopy* 133–164 (John Wiley & Sons, Ltd, 2017).

98.   Abbe, E. Beiträge zur Theorie des Mikroskops und der mikroskopischen Wahrnehmung. *Arkiv. Mikroskop. Anat.* **9,** 413–468 (1873).

99.   Heintzmann, R. & Ficz, G. Breaking the resolution limit in light microscopy. *Brief. Funct. Genom.* **5,** 289–301 (2006).

100.   Rayleigh, L. Investigations in optics, with special reference to the spectroscope. *Philos. Mag.* **8,** 261–274 (1879).

101.   Birk, U., Best, G., Amberger, R. & Cremer, C. in *Fluorescence Microscopy* 291–319 (John Wiley & Sons, Ltd, 2017).

102.   Gustafsson, M. G., Shao, L., Carlton, P. M., Wang, C. R., Golubovskaya, I. N., Cande, W. Z., Agard, D. A. & Sedat, J. W. Three-dimensional resolution doubling in wide-field fluorescence microscopy by structured illumination. *Biophys. J.* **94,** 4957–4970 (2008).

103.   Zhang, J., Huang, S.-Y., Lin, Z.-H. & Huang, J.-S. Generation of optical chirality patterns with plane waves, evanescent waves and surface plasmon waves. *Opt. Express* **28,** 760–772 (2020).

104.   Huang, S.-Y., Zhang, J., Karras, C., Förster, R., Heintzmann, R. & Huang, J.-S. Chiral Structured Illumination Microscopy. *ACS Photonics* **8,** 130–134 (2021).

105.   Zhang, J., Huang, S.-Y., Singh, A. K. & Huang, J.-S. Structured illumination microscopy for simultaneous imaging of achiral and chiral domains. *Opt. Lett.* **46,** 4546–4549 (2021).

106.   Förster, R., Lu-Walther, H.-W., Jost, A., Kielhorn, M., Wicker, K. & Heintzmann, R. Simple structured illumination microscope setup with high

acquisition speed by using a spatial light modulator. *Opt. Express* **22,** 20663–20677 (2014).

107. Park, J. H., Lee, S.-W., Lee, E. S. & Lee, J. Y. A method for super-resolved CARS microscopy with structured illumination in two dimensions. *Opt. Express* **22,** 9854–9870 (2014).

108. Wicker, K., Mandula, O., Best, G., Fiolka, R. & Heintzmann, R. Phase optimisation for structured illumination microscopy. *Opt. Express* **21,** 2032–2049 (2013).

109. Wicker, K. *Increasing resolution and light efficiency in fluorescence microscopy* PhD thesis (King's College London, 2010).

110. Luengo, C. DIPimage. *GitHub repository* (2021).

111. Mandracchia, B., Hua, X., Guo, C., Son, J., Urner, T. & Jia, S. Fast and accurate sCMOS noise correction for fluorescence microscopy. *Nat. Commun.* **11,** 1–12 (2020).

112. Huang, S.-Y., Singh, A. K. & Huang, J.-S. Signal and noise analysis for chiral structured illumination microscopy. *Opt. Express* **29,** 23056–23072 (2021).

113. Kubin, R. F. & Fletcher, A. N. Fluorescence quantum yields of some rhodamine dyes. *J. Lumin.* **27,** 455–462 (1982).

114. Djorović, A., Meyer, M., Darby, B. L. & Le Ru, E. C. Accurate modeling of the polarizability of dyes for electromagnetic calculations. *ACS Omega* **2,** 1804–1811 (2017).

115. Schermelleh, L., Ferrand, A., Huser, T., Eggeling, C., Sauer, M., Biehlmaier, O. & Drummen, G. P. Super-resolution microscopy demystified. *Nat. Cell Biol.* **21,** 72–84 (2019).

116. Hendry, E., Carpy, T., Johnston, J., Popland, M., Mikhaylovskiy, R., Lapthorn, A., Kelly, S., Barron, L., Gadegaard, N. & Kadodwala, M. Ultrasensitive detection and characterization of biomolecules using superchiral fields. *Nat. Nanotechnol.* **5,** 783–787 (2010).

117.  Schäferling, M., Dregely, D., Hentschel, M. & Giessen, H. Tailoring enhanced optical chirality: design principles for chiral plasmonic nanostructures. *Phys. Rev. X* **2,** 031010 (2012).

118.  Schäferling, M., Yin, X., Engheta, N. & Giessen, H. Helical plasmonic nanostructures as prototypical chiral near-field sources. *ACS Photonics* **1,** 530–537 (2014).

119.  Lin, D. & Huang, J.-S. Slant-gap plasmonic nanoantennas for optical chirality engineering and circular dichroism enhancement. *Opt. Express* **22,** 7434–7445 (2014).

120.  Tian, X., Fang, Y. & Sun, M. Formation of enhanced uniform chiral fields in symmetric dimer nanostructures. *Sci. Rep.* **5,** 1–12 (2015).

121.  Schäferling, M., Engheta, N., Giessen, H. & Weiss, T. Reducing the complexity: Enantioselective chiral near-fields by diagonal slit and mirror configuration. *ACS Photonics* **3,** 1076–1084 (2016).

122.  Kang, L., Ren, Q. & Werner, D. H. Leveraging superchiral light for manipulation of optical chirality in the near-field of plasmonic metamaterials. *ACS Photonics* **4,** 1298–1305 (2017).

123.  García-Guirado, J., Svedendahl, M., Puigdollers, J. & Quidant, R. Enantiomer-selective molecular sensing using racemic nanoplasmonic arrays. *Nano Lett.* **18,** 6279–6285 (2018).

124.  Mun, J. & Rho, J. Surface-enhanced circular dichroism by multipolar radiative coupling. *Opt. Lett.* **43,** 2856–2859 (2018).

125.  Lu, F., Zhang, W., Zhang, J., Zhang, L., Xue, T., Liu, M., Meng, C., Mao, D. & Mei, T. Dynamic manipulation of optical chirality for gammadion nanostructures. *Appl. Phys. Express* **12,** 072015 (2019).

126.  Gilroy, C., Hashiyada, S., Endo, K., Karimullah, A. S., Barron, L. D., Okamoto, H., Togawa, Y. & Kadodwala, M. Roles of superchirality and interference in chiral plasmonic biodetection. *J. Phys. Chem. C* **123,** 15195–15203 (2019).

127. Petronijevic, E., Sandoval, E. M., Ramezani, M., Ordóñez-Romero, C. L., Noguez, C., Bovino, F. A., Sibilia, C. & Pirruccio, G. Extended chiro-optical near-field response of achiral plasmonic lattices. *J. Phys. Chem. C* **123,** 23620–23627 (2019).

128. Horrer, A., Zhang, Y., Gérard, D., Béal, J., Kociak, M., Plain, J. & Bachelot, R. Local optical chirality induced by near-field mode interference in achiral plasmonic metamolecules. *Nano Lett.* **20,** 509–516 (2019).

129. Qin, J., Deng, L., Kang, T., Nie, L., Feng, H., Wang, H., Yang, R., Liang, X., Tang, T., Shen, J., *et al.* Switching the Optical Chirality in Magnetoplasmonic Metasurfaces Using Applied Magnetic Fields. *ACS Nano* **14,** 2808–2816 (2020).

130. Mattioli, F., Mazzeo, G., Longhi, G., Abbate, S., Pellegrini, G., Mogni, E., Celebrano, M., Finazzi, M., Duò, L., Zanchi, C. G., *et al.* Plasmonic superchiral lattice resonances in the mid-infrared. *ACS Photonics* **7,** 2676–2681 (2020).

131. Fazel-Najafabadi, A., Schuster, S. & Auguié, B. Orientation averaging of optical chirality near nanoparticles and aggregates. *Phys. Rev. B* **103,** 115405 (2021).

132. Yoo, S., Cho, M. & Park, Q.-H. Globally enhanced chiral field generation by negative-index metamaterials. *Phys. Rev. B* **89,** 161405 (2014).

133. Ho, C.-S., Garcia-Etxarri, A., Zhao, Y. & Dionne, J. Enhancing enantioselective absorption using dielectric nanospheres. *ACS Photonics* **4,** 197–203 (2017).

134. Mohammadi, E., Tsakmakidis, K., Askarpour, A., Dehkhoda, P., Tavakoli, A. & Altug, H. Nanophotonic platforms for enhanced chiral sensing. *ACS Photonics* **5,** 2669–2675 (2018).

135. Yao, K. & Liu, Y. Enhancing circular dichroism by chiral hotspots in silicon nanocube dimers. *Nanoscale* **10,** 8779–8786 (2018).

136. Solomon, M. L., Hu, J., Lawrence, M., García-Etxarri, A. & Dionne, J. A. Enantiospecific optical enhancement of chiral sensing and separation with dielectric metasurfaces. *ACS Photonics* **6,** 43–49 (2018).

137. Graf, F., Feis, J., Garcia-Santiago, X., Wegener, M., Rockstuhl, C. & Fernandez-Corbaton, I. Achiral, helicity preserving, and resonant structures for enhanced sensing of chiral molecules. *ACS Photonics* **6,** 482–491 (2019).

138. Hu, J., Lawrence, M. & Dionne, J. A. High quality factor dielectric metasurfaces for ultraviolet circular dichroism spectroscopy. *ACS Photonics* **7,** 36–42 (2020).

139. Zhao, X. & Reinhard, B. M. Switchable chiroptical hot-spots in silicon nanodisk dimers. *ACS Photonics* **6,** 1981–1989 (2019).

140. Yao, K. & Zheng, Y. Near-ultraviolet dielectric metasurfaces: from surface-enhanced circular dichroism spectroscopy to polarization-preserving mirrors. *J. Phys. Chem. C* **123,** 11814–11822 (2019).

141. Mohammadi, E., Tavakoli, A., Dehkhoda, P., Jahani, Y., Tsakmakidis, K. L., Tittl, A. & Altug, H. Accessible superchiral near-fields driven by tailored electric and magnetic resonances in all-dielectric nanostructures. *ACS Photonics* **6,** 1939–1946 (2019).

142. Solomon, M. L., Abendroth, J. M., Poulikakos, L. V., Hu, J. & Dionne, J. A. Fluorescence-detected circular dichroism of a chiral molecular monolayer with dielectric metasurfaces. *J. Am. Chem. Soc.* **142,** 18304–18309 (2020).

143. Garcia-Guirado, J., Svedendahl, M., Puigdollers, J. & Quidant, R. Enhanced chiral sensing with dielectric nanoresonators. *Nano Lett.* **20,** 585–591 (2020).

144. Wu, T., Zhang, W., Zhang, H., Hou, S., Chen, G., Liu, R., Lu, C., Li, J., Wang, R., Duan, P., *et al.* Vector exceptional points with strong superchiral fields. *Phys. Rev. Lett.* **124,** 083901 (2020).

145. Du, K., Li, P., Wang, H., Gao, K., Liu, R.-B., Lu, F., Zhang, W. & Mei, T. Optical chirality enhancement in hollow silicon disk by dipolar interference. *Adv. Opt. Mater.* **9,** 2001771 (2021).

146. Tseng, M. L., Jahani, Y., Leitis, A. & Altug, H. Dielectric Metasurfaces Enabling Advanced Optical Biosensors. *ACS Photonics* **8,** 47–60 (2020).

147. Jeon, S. & Kim, S. J. Enhancement of Optical Chirality Using Metasurfaces for Enantiomer-Selective Molecular Sensing. *Appl. Sci.* **11,** 2989 (2021).

148. Kerker, M., Wang, D.-S. & Giles, C. Electromagnetic scattering by magnetic spheres. *J. Opt. Soc. Am.* **73,** 765–767 (1983).

149. Liu, W. & Kivshar, Y. S. Generalized Kerker effects in nanophotonics and meta-optics. *Opt. Express* **26,** 13085–13105 (2018).

150. Mudry, E., Belkebir, K., Girard, J., Savatier, J., Le Moal, E., Nicoletti, C., Allain, M. & Sentenac, A. Structured illumination microscopy using unknown speckle patterns. *Nat. Photonics* **6,** 312–315 (2012).

151. Ponsetto, J. L., Wei, F. & Liu, Z. Localized plasmon assisted structured illumination microscopy for wide-field high-speed dispersion-independent super resolution imaging. *Nanoscale* **6,** 5807–5812 (2014).

152. Ponsetto, J. L., Bezryadina, A., Wei, F., Onishi, K., Shen, H., Huang, E., Ferrari, L., Ma, Q., Zou, Y. & Liu, Z. Experimental demonstration of localized plasmonic structured illumination microscopy. *ACS Nano* **11,** 5344–5350 (2017).

153. O'connor, D., Ginzburg, P., Rodríguez-Fortuño, F. J., Wurtz, G. A. & Zayats, A. V. Spin–orbit coupling in surface plasmon scattering by nanostructures. *Nat. Commun.* **5,** 1–7 (2014).

154. Bliokh, K. Y., Rodríguez-Fortuño, F. J., Nori, F. & Zayats, A. V. Spin–orbit interactions of light. *Nat. Photonics* **9,** 796–808 (2015).

155. Pan, D., Wei, H., Gao, L. & Xu, H. Strong spin-orbit interaction of light in plasmonic nanostructures and nanocircuits. *Phys. Rev. Lett.* **117,** 166803 (2016).

156. Grice, A., Bradley, D., Bernius, M., Inbasekaran, M., Wu, W. & Woo, E. High brightness and efficiency blue light-emitting polymer diodes. *Appl. Phys. Lett.* **73,** 629–631 (1998).

157. Halls, J. J., Arias, A. C., MacKenzie, J. D., Wu, W., Inbasekaran, M., Woo, E. P. & Friend, R. H. Photodiodes based on polyfluorene composites: influence of morphology. *Adv. Mater.* **12,** 498–502 (2000).

158. Günes, S., Neugebauer, H. & Sariciftci, N. S. Conjugated polymer-based organic solar cells. *Chem. Rev.* **107,** 1324–1338 (2007).

159. Inganäs, O., Zhang, F. & Andersson, M. R. Alternating polyfluorenes collect solar light in polymer photovoltaics. *Acc. Chem. Res.* **42,** 1731–1739 (2009).

160. Oda, M., Nothofer, H.-G., Lieser, G., Scherf, U., Meskers, S. & Neher, D. Circularly polarized electroluminescence from liquid-crystalline chiral polyfluorenes. *Adv. Mater.* **12,** 362–365 (2000).

161. Lakhwani, G., Meskers, S. C. & Janssen, R. A. Circular differential scattering of light in films of chiral polyfluorene. *J. Phys. Chem. B* **111,** 5124–5131 (2007).

162. Lakhwani, G., Janssen, R. A. & Meskers, S. C. Anisotropic dielectric tensor for chiral polyfluorene at optical frequencies. *J. Phys. Chem. B* **113,** 14165–14171 (2009).

163. Lakhwani, G., Gielen, J., Kemerink, M., Christianen, P. C., Janssen, R. A. & Meskers, S. C. Intensive chiroptical properties of chiral polyfluorenes associated with fibril formation. *J. Phys. Chem. B* **113,** 14047–14051 (2009).

164. Lakhwani, G. & Meskers, S. C. Insights from chiral polyfluorene on the unification of molecular exciton and cholesteric liquid crystal theories for chiroptical phenomena. *TJ. Phys. Chem. A* **116,** 1121–1128 (2012).

165. Lu-Walther, H.-W., Kielhorn, M., Förster, R., Jost, A., Wicker, K. & Heintzmann, R. fastSIM: a practical implementation of fast structured illumination microscopy. *Methods Appl. Fluoresc.* **3,** 014001 (2015).

166. Novotny, L. & Hecht, B. *Principles of nano-optics* (Cambridge university press, 2012).

167. *Introduction to the SXGA-3DM System* Forth Dimension Displays (July 15, 2020). 47 pp.

168. LeCun, Y., Bengio, Y. & Hinton, G. Deep learning. *Nature* **521,** 436–444 (2015).

169. Sarker, I. H. Deep learning: a comprehensive overview on techniques, taxonomy, applications and research directions. *SN comput. sci.* **2,** 1–20 (2021).

170. Moen, E., Bannon, D., Kudo, T., Graf, W., Covert, M. & Van Valen, D. Deep learning for cellular image analysis. *Nat. Methods* **16,** 1233–1246 (2019).

171. Eraslan, G., Avsec, Ž., Gagneur, J. & Theis, F. J. Deep learning: new computational modelling techniques for genomics. *Nat. Rev. Genet.* **20,** 389–403 (2019).

172. Molesky, S., Lin, Z., Piggott, A. Y., Jin, W., Vucković, J. & Rodriguez, A. W. Inverse design in nanophotonics. *Nat. Photonics* **12,** 659–670 (2018).

173. Yao, K., Unni, R. & Zheng, Y. Intelligent nanophotonics: merging photonics and artificial intelligence at the nanoscale. *Nanophotonics* **8,** 339–366 (2019).

174. Hegde, R. S. Deep learning: a new tool for photonic nanostructure design. *Nanoscale Adv.* **2,** 1007–1023 (2020).

175. So, S., Badloe, T., Noh, J., Bravo-Abad, J. & Rho, J. Deep learning enabled inverse design in nanophotonics. *Nanophotonics* **9,** 1041–1057 (2020).

176. Malkiel, I., Mrejen, M., Wolf, L. & Suchowski, H. Machine learning for nanophotonics. *MRS Bull.* **45,** 221–229 (2020).

177. Wiecha, P. R., Arbouet, A., Girard, C. & Muskens, O. L. Deep learning in nano-photonics: inverse design and beyond. *Photonics Res.* **9,** B182–B200 (2021).

178. Ma, W., Liu, Z., Kudyshev, Z. A., Boltasseva, A., Cai, W. & Liu, Y. Deep learning for the design of photonic structures. *Nat. Photonics* **15,** 77–90 (2021).

179. He, J., He, C., Zheng, C., Wang, Q. & Ye, J. Plasmonic nanoparticle simulations and inverse design using machine learning. *Nanoscale* **11,** 17444–17459 (2019).

180. Wu, Q., Li, X., Jiang, L., Xu, X., Fang, D., Zhang, J., Song, C., Yu, Z., Wang, L. & Gao, L. Deep neural network for designing near-and far-field properties in plasmonic antennas. *Opt. Mater. Express* **11,** 1907–1917 (2021).

181. Yu, L., Barakat, E., Sfez, T., Hvozdara, L., Di Francesco, J. & Herzig, H. P. Manipulating Bloch surface waves in 2D: a platform concept-based flat lens. *Light: Sci. Appl.* **3,** e124–e124 (2014).

182. Sinibaldi, A., Fieramosca, A., Rizzo, R., Anopchenko, A., Danz, N., Munzert, P., Magistris, C., Barolo, C. & Michelotti, F. Combining label-free and fluorescence operation of Bloch surface wave optical sensors. *Opt. Lett.* **39,** 2947–2950 (2014).

183. Pellegrini, G., Finazzi, M., Celebrano, M., Duò, L. & Biagioni, P. Chiral surface waves for enhanced circular dichroism. *Phys. Rev. B* **95,** 241402 (2017).

184. Pellegrini, G., Finazzi, M., Celebrano, M., Duò, L. & Biagioni, P. Surface-enhanced chiroptical spectroscopy with superchiral surface waves. *Chirality* **30,** 883–889 (2018).

185. Pellegrini, G., Finazzi, M., Celebrano, M., Duò, L., Iatì, M. A., Maragò, O. M. & Biagioni, P. Superchiral surface waves for all-optical enantiomer separation. *J. Phys. Chem. C* **123,** 28336–28342 (2019).

186. Lee, W., Jose, D., Phelps, C., Marcus, A. H. & von Hippel, P. H. A single-molecule view of the assembly pathway, subunit stoichiometry, and unwinding activity of the bacteriophage T4 primosome (helicase–primase) complex. *Biochemistry* **52,** 3157–3170 (2013).

187. Kringle, L., Sawaya, N. P., Widom, J., Adams, C., Raymer, M. G., Aspuru-Guzik, A. & Marcus, A. H. Temperature-dependent conformations of exciton-coupled Cy3 dimers in double-stranded DNA. *J. Chem. Phys.* **148,** 085101 (2018).

188. Lan, X., Zhou, X., McCarthy, L. A., Govorov, A. O., Liu, Y. & Link, S. DNA-Enabled Chiral Gold Nanoparticle–Chromophore Hybrid Structure with Resonant Plasmon–Exciton Coupling Gives Unusual and Strong Circular Dichroism. *J. Am. Chem. Soc.* **141,** 19336–19341 (2019).

189. Meadows, F., Narayanan, N. & Patonay, G. Determination of protein–dye association by near infrared fluorescence-detected circular dichroism. *Talanta* **50,** 1149–1155 (2000).

# Appendices

## Appendix A

# Derivation of Polarization Ellipse

The $x$ and $y$-component of the electric field can be written by

$$E_x = E_{0x} \cos(\omega t - kz + \varphi_x), \tag{A.1}$$

$$E_y = E_{0y} \cos(\omega t - kz + \varphi_y), \tag{A.2}$$

where $E_{0x}$ ($E_{0y}$) denotes the electric field amplitude of $x$ ($y$)-component. Then, we can obtain the ratio of $E_y$ and $E_{0y}$:

$$\frac{E_y}{E_{0y}} = \cos(\omega t - kz + \varphi_y - \varphi_x + \varphi_x)$$

$$= \cos(\omega t - kz + \varphi_x + \Delta\varphi), \tag{A.3}$$

where $\Delta\varphi \equiv \varphi_y - \varphi_x$. According to the sum and difference identity of trigonometric functions $\cos(\alpha + \beta) = \cos\alpha\cos\beta - \sin\alpha\sin\beta$,, we can rewrite Eq. A.3 by

$$\frac{E_y}{E_{0y}} = \cos(\omega t - kz + \varphi_x)\cos\Delta\varphi - \sin(\omega t - kz + \varphi_x)\sin\Delta\varphi$$

$$= \frac{E_x}{E_{0x}}\cos\Delta\varphi - \sqrt{1 - (\frac{E_x}{E_{0x}})^2}\sin\Delta\varphi. \tag{A.4}$$

After rearranging Eq. A.4, we can obtain the equation of polarization ellipse:

$$(\frac{E_x}{E_{0x}})^2 + (\frac{E_y}{E_{0y}})^2 - 2\frac{E_x E_y}{E_{0x} E_{0y}}\cos\Delta\varphi = \sin^2\Delta\varphi. \tag{A.5}$$

# Appendix B

# Cross-Correlation of $\bar{\Omega}_{-1}(\mathbf{k})$ and $\bar{\Omega}_1(\mathbf{k})$ with Additional Phase Factor

Considering the definition of cross-correlation [109], we can obtain

$$
\begin{aligned}
\mathcal{C}_{-1,1}(\mathbf{k}) &= e^{-i\varphi'}\bar{\Omega}_{-1}(\mathbf{k}) \circledast e^{i\varphi'}\bar{\Omega}_1(\mathbf{k}) \\
&= \int e^{-i\varphi'}\bar{\Omega}_{-1}(\mathbf{k}'')\Big[e^{i\varphi'}\bar{\Omega}_1(\mathbf{k}+\mathbf{k}'')\Big]^* d\mathbf{k}'' \\
&= e^{-2i\varphi'}\int \bar{\Omega}_{-1}(\mathbf{k}'')\bar{\Omega}_1^*(\mathbf{k}+\mathbf{k}'')d\mathbf{k}'' \\
&= e^{-2i\varphi'}\int e^{i\theta_{-1}(\mathbf{k})}|\bar{\Omega}_{-1}(\mathbf{k}'')|e^{-i\theta_1(\mathbf{k})}|\bar{\Omega}_1(\mathbf{k}+\mathbf{k}'')|d\mathbf{k}''.
\end{aligned}
\tag{B.1}
$$

Because the position-corrected components $\bar{\Omega}_{\pm 1}(\mathbf{k})$ should, in principle, have identical phase, $\theta_1(\mathbf{k})$ is equal to $\theta_{-1}(\mathbf{k})$. Therefore, the two phase factors $e^{i\theta_{-1}(\mathbf{k})}$ and $e^{-i\theta_1(\mathbf{k})}$ are canceled out and Eq. B.1 can be simplified as

$$
\mathcal{C}_{-1,1}(\mathbf{k}) = e^{-i2\varphi'}\Big[|\bar{\Omega}_{-1}(\mathbf{k})| \circledast |\bar{\Omega}_1(\mathbf{k})|\Big].
\tag{B.2}
$$

# Appendix C

# Derivation of $\mathrm{Var}[\bar{\chi}'_{l'}(\mathbf{k})]$

$$\mathrm{Var}\Big[\bar{\chi}'_{l'}(\mathbf{k})\Big] = \mathrm{Var}\Big[\frac{\varepsilon}{2\gamma}\frac{1}{3}\sum_{j=1}^{3}\bar{N}_{shot,j}(\mathbf{k})\Big]$$

$$= \Big(\frac{\varepsilon}{6\gamma}\Big)^{2}\mathrm{Var}\Big[\sum_{j=1}^{3}\sum_{\mathbf{r}}N_{shot,j}(\mathbf{r})\Big]$$

$$= \Big(\frac{\varepsilon}{6\gamma}\Big)^{2}\sum_{j=1}^{3}\sum_{\mathbf{r}}M_{j}(\mathbf{r})$$

$$= \Big(\frac{\varepsilon}{6\gamma}\Big)^{2}\times\frac{6\gamma}{\varepsilon}\bar{\Omega}(0)$$

$$= \frac{\varepsilon\omega U_{e,0}\bar{\alpha}''(0)\bar{h}(0)}{6\gamma} \tag{C.1}$$

# Ehrenwörtliche Erklärung

Ich erkläre hiermit ehrenwörtlich, dass ich die vorliegende Arbeit selbständig, ohne unzulässige Hilfe Dritter und ohne Benutzung anderer als der angegebenen Hilfsmittel und Literatur angefertigt habe. Die aus anderen Quellen direkt oder indirekt übernommenen Daten und Konzepte sind unter Angabe der Quelle gekennzeichnet.

Bei der Auswahl und Auswertung folgenden Materials haben mir die nachstehend aufgeführten Personen in der jeweils beschriebenen Weise entgeltlich/unentgeltlich geholfen:

1. Dr. Girish Lakhwani and Dr. Ashish Sharma, providing the chiral polymers.

2. Dr. Uwe Hübner, fabricaiton of the chiral polyfluorene samples.

Weitere Personen waren an der inhaltlich-materiellen Erstellung der vorliegenden Arbeit nicht beteiligt. Insbesondere habe ich hierfür nicht die entgeltliche Hilfe von Vermittlungsbzw. Beratungsdiensten (Promotionsberater oder andere Personen) in Anspruch genommen. Niemand hat von mir unmittelbar oder mittelbar geldwerte Leistungen für Arbeiten erhalten, die im Zusammenhang mit dem Inhalt der vorgelegten Dissertation stehen.

Die Arbeit wurde bisher weder im In- noch im Ausland in gleicher oder ähnlicher Form einer anderen Prüfungsbehörde vorgelegt. Die geltende Promotionsordnung der Physikalisch-Astronomischen Fakultät ist mir bekannt. Ich versichere ehrenwörtlich, dass ich nach bestem Wissen die reine Wahrheit gesagt und nichts verschwiegen habe.

---

Ort, Datum

Unterschrift d. Verfassers

# Curriculum Vitae

Shiang-Yu Huang

Date of birth          06.10.1990 in Taoyuan City, Taiwan

**Education**

2017/01 – 2022/6       Ph.D. Candidate

*Department of Physics,*

*Friedrich-Schiller-Universiät Jena, Jena, Germany*

2013/09 – 2015/08      Master of Science

*Department of Electrophysics*

*National Chiao Tung University, Hsinchu, Taiwan*

2009/09 – 2013/06      Bachelor of Science

*Department of Electrophysics*

*National Chiao Tung University, Hsinchu, Taiwan*

# Publications

## Peer-Reviewed Journals

1. Zhang, J., Huang, S.-Y., Lin, Z.-H. & Huang, J.-S. Generation of optical chirality patterns with plane waves, evanescent waves and surface plasmon waves. *Opt. Express* **28**, 760–772 (2020)

2. Huang, S.-Y., Zhang, J., Karras, C., Förster, R., Heintzmann, R. & Huang, J.-S. Chiral Structured Illumination Microscopy. *ACS Photonics* **8**, 130–134 (2021)

3. Huang, S.-Y., Singh, A. K. & Huang, J.-S. Signal and Noise Analysis for Chiral Structured Illumination Microscopy. *Opt. Express* **29**, 23056–23072 (2021)

4. Zhang, J., Huang, S.-Y., Singh, A. K. & Huang, J.-S. Structured Illumination Microscopy for Simultaneous Imaging of Achiral and Chiral Domains. *Optics Letters* **46**, 4546–4549 (2021)

## Conference Presentations

1. Huang, S.-Y., Zhang, J., & Huang, J.-S. Generation of Optical Chirality Lattice by Light Interference, Poster presentation delivered at 17th International Conference on Chiroptical Spectroscopy – CD2019, June 24, 2019, Pisa, Italy.

2. Huang, S.-Y., Zhang, J., Karras, C., Förster, R., Heintzmann, R.* & Huang, J.-S., Chiral Structured Illumination Microscopy – Wide-Field Chiral Imaging with Super-Resolution. Oral presentation delivered at Dornburg Doctoral Seminar 2020, February 19, Jena, Germany, 2020.

3. Huang, S.-Y., Zhang, J., Karras, C., Förster, R., Heintzmann, R.* & Huang, J.-S., Chiral Structured Illumination Microscopy. Poster presentation delivered at EurAsian Conference on Nanophotonics 2020, April 4, Jena, Germany, 2020.

4. Huang, S.-Y., Zhang, J., Karras, C., Förster, R., Heintzmann, R.* & Huang, J.-S., Chiral structured illumination microscopy: fast imaging chiral domains at super-resolution. Oral presentation delivered at SPIE Photonics Europe 2022, April 5, Strasbourg, France, 2022.